GEORG-AUGUST-UNIVERSITÄT GÖTTINGEN

II. Physikalisches Institut

Feasibility study for the measurement of the inclusive and differential $Z(\rightarrow e^+e^-) + \ jets$ cross section in pp-collisions with the ATLAS experiment at the LHC

von

Katharina Bierwagen

This thesis describes a feasibility study for the measurement of the inclusive and differential $Z(\rightarrow e^+e^-) + \ jets$ cross section for the first 100 pb^{-1} of data with the ATLAS detector at the Large Hadron Collider in Geneva. This study is done on hadron level using predictions from fully simulated Monte Carlo samples and compare them to NLO pertubative QCD calculations including statistical and systematic limitations. In addition, the predictions from different Monte Carlo generators are compared. The inclusive $Z(\rightarrow e^+e^-)+ \geq 1-3 \ jets$ cross section can be determined with a precision of smaller than 25.5%.

Post address:
Friedrich-Hund-Platz 1
37077 Göttingen
Germany

II.Physik-UniGö-Dipl-2009/04

II. Physikalisches Institut
Georg-August-Universität Göttingen

October 2009

GEORG-AUGUST-UNIVERSITÄT

GÖTTINGEN

II. Physikalisches Institut

Feasibility study for the measurement of the inclusive and differential $Z(\rightarrow e^+e^-) + \ jets$ cross section in pp-collisions with the ATLAS experiment at the LHC

von

Katharina Bierwagen

Dieser Forschungsbericht wurde als Diplomarbeit von der Fakultät für Physik der Georg-August-Universität zu Göttingen angenommen.

Angenommen am:	22. Oktober 2009
Referent:	Prof. Dr. Arnulf Quadt
Korreferent:	Prof. Dr. Ariane Frey

Contents

Part I

Overview

1 Introduction

At the end of 2009 the Large Hadron Collider (LHC) at CERN will begin operation, colliding protons at a low centre of mass energy. It will ramp up to 7 TeV and later in 2010 to $8-10$ TeV. The LHC is built to test the Standard Model and to search for new physical phenomena, like Higgs boson production or supersymmetry. The ATLAS detector is one of the four experiments of the LHC. For the first year of data taking, an integrated luminosity of $100-200\,\mathrm{pb}^{-1}$ is expected.

Before making any discoveries of new physical phenomena, the detector has to be understood and calibrated using well understood physics processes. At the next step Standard Model processes can be studied.

The aim of the analysis presented in this diploma thesis, is to prepare a measurement of the inclusive and differential $Z(\rightarrow e^+e^-) + \ jets$ cross sections in the first data taken with the ATLAS detector. In particular, the key quantities used for the selection of the Higgs boson produced by vector boson fusion are studied. In addition, a comparison to theory predictions is prepared and the possibility to distinguish between Monte Carlo generators is studied.
In this thesis, a feasibility study with fully simulated Monte Carlo for $100\,\mathrm{pb}^{-1}$ at a centre of mass energy of 10 TeV is presented. In order to do this, Monte Carlo samples from ALPGEN, PYTHIA and MC@NLO are used. The comparison with theory predictions calculated in LO and NLO with pertubative QCD using MCFM is done on hadron level to be independent from detector setup. Therefore, the theory predictions are corrected for non-pertubative effects, like underlying event and fragmentation, and the data is corrected for detector effects, comparing different correction methods.

Chapter 2 starts with the introduction in the Standard Model and the Higgs Mechanism. In addition, the phenomenology of the proton-proton collisions is explained. In Chapter 3 the LHC experiment and the ATLAS detector layout are presented. Chapter 4 describes the phenomenology of the Z boson and the Higgs boson at the LHC. The ATLAS computing model and the different Monte Carlo Generators currently used in ATLAS are outlined in Chapter 5. Chapter 6 describes the reconstruction and identification algorithms and cuts for the different particles and Chapter 7 gives the motivation for the analysis described in detail in Chapter 8 to 10. The combination of the results of Chapter 9 and 10 are given in Chapter 11, comparing the different methods for the correction of detector effects and summarizing the statistical and systematic uncertainties on the cross section ratio between data and theory. Finally, a conclusion and an outlook are given in Chapter 12.

2 Theory

In this chapter, the Standard Model (SM) and the Higgs mechanism are introduced. In particular, the formalism of Quantum Electrodynamics (QED), Quantum Chromodynamics (QCD) and the electroweak (EW) theory are explained.

2.1 Introduction into the Standard Model of Particle Physics

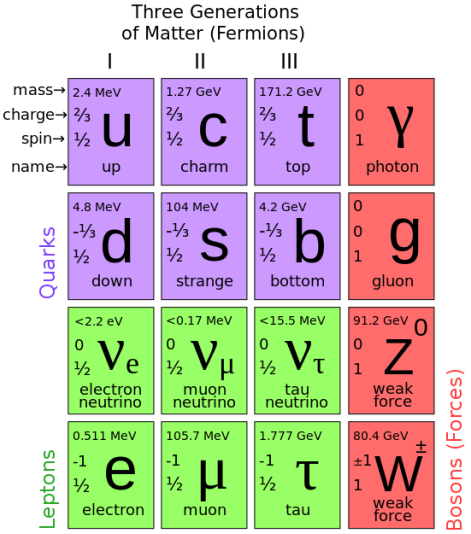

Figure 2.1: Particle content of the Standard Model of particles physics.

Particle physics is interested in revealing the composition of the universe, especially the smallest structure of matter. In order to describe this structure the Standard Model (SM) is used in particle physics, in which known matter is ascribed to a few elementary particles, the fermions. In addition, the SM includes three out of four known fundamental interactions, the electromagnetic, the strong and the weak interaction. The carriers of these interactions are the gauge bosons, gluons for the strong interaction, $W^{\pm}$ and Z^0 bosons for the weak interaction and photons for the EM interaction. Gravity is the only of the fundamental forces that is not described by the SM.

The fermions can be split into two groups of particles, the leptons and the quarks. In contrast to the leptons the quarks can participate in the strong interaction. Leptons and quarks can be split into three generations, see Fig. 2.1. Each generation consists of two leptons and two quarks, the leptons carry the electromagnetic charge 0 or -1, the up type quarks $+2/3$ and the down type quarks $-1/3$. In addition, each quark has one degree of freedom which can take three values from the strong interaction, which are called colour charge. For each of these fermions an antiparticle exists with the opposite charge[1], so in total 12 leptons and 36 quarks.

[1] Neutrino and antineutrino have the same charge (=0), but opposite handedness

Generally from generation to generation the masses of the particles become larger. In addition, the SM has one further particle, the Higgs Boson, which is not discovered yet, but gives a possible solution for the principle of mass creation, the so-called Higgs Mechanism, which is described in Sect. 2.3. Although the SM fits very well to the current measurements, it is not a complete theory and there are still some open questions:

- What about gravity? Only the electromagnetic, the weak and the strong force are explained by the Standard Model.
- How can the matter/ antimatter asymmetry in our universe today be explained?
- How can neutrino masses be explained?
- Why are there three generations of particles?
- The SM only describes 4% of the universe. How can dark matter and dark energy be explained?

The discovery of the Higgs boson and the open questions are the motivation for new experiments such as the Large Hadron Collider.

2.2 Mathematical Description of the Standard Model and the Interactions

Within the Standard Model, the properties of the interactions result from the requirement of local gauge invariance and can be described by group theory. The gauge group of the SM is the direct product

$$\mathrm{SU}(3)_C \otimes \mathrm{SU}(2)_L \otimes \mathrm{U}(1)_Y, \tag{2.1}$$

where C is colour, Y is hypercharge and L is left-handed.
In the following sections the mathematical formulation of SM interactions is described.

2.2.1 Quantum Electrodynamics

Quantum electrodynamics (QED) [1] describes the electromagnetic interaction for charged fermions (spin-1/2 particles). The gauge group of QED is the $\mathrm{U}(1)_{em}$. From the demand for local gauge invariance the Lagrangian of the QED can be written as:

$$L_{QED} = \bar{\Psi}(x)(i\gamma^\mu \partial_\mu - m)\Psi(x) - q\Psi(x)\gamma^\mu A_\mu \Psi(x) - \frac{1}{4}F_{\mu\nu}F^{\mu\nu}, \tag{2.2}$$

in which a mass term for the leptons is allowed, while a mass term for the photons is prohibited. The Lagrangian of the QED is derived starting with the Lagrangian of the free Dirac particle

$$L_0 = i\bar{\Psi}(x)\gamma^\mu \partial_\mu \Psi(x) - \bar{\Psi}(x)m\Psi(x). \tag{2.3}$$

The Lagrangian is invariant under a global $\mathrm{U}(1)_{em}$ transformation[2]

$$\Psi(x) \rightarrow \Psi'(x) = e^{iq\alpha}\Psi(x), \tag{2.4}$$

[2] At each point the phase is changed by the same absolute value.

in which α is an arbitrary constant.

Nonetheless, this Lagrangian is not invariant under a local gauge transformation in which $\alpha(x)$ depends on the position. Therefore one needs a gauge covariant derivative instead of the normal derivative, which fulfils the following constraint:

$$D_\mu \Psi(x) \rightarrow e^{iq\alpha(x)} D_\mu \Psi(x). \tag{2.5}$$

One defines

$$D_\mu \equiv \partial_\mu + iqA_\mu(x), \tag{2.6}$$

where A_μ is the gauge field, which describes in this case the photon field, and is transformed in the following way:

$$A_\mu(x) \rightarrow A'_\mu(x) = A_\mu(x) - \frac{1}{q}\partial_\mu \alpha(x). \tag{2.7}$$

Substituting Eq. 2.6 in Eq. 2.3, one gets the necessary invariance for a local $U(1)_{em}$ transformation and therefore the following Lagrangian:

$$L = \bar{\Psi}(x)(i\gamma^\mu \partial_\mu - m)\Psi(x) - q\Psi(x)\gamma^\mu A_\mu \Psi(x). \tag{2.8}$$

In Eq. 2.8, the first term describes again the Lagrangian of the free Dirac particle and the second term describes the coupling to the gauge field.

Then, a term for the kinetic energy of the photons has to be added,

$$L_{EM} = -\frac{1}{4} F_{\mu\nu} F^{\mu\nu}, \tag{2.9}$$

with the field strength tensor $F^{\mu\nu} = \partial_\mu A_\nu(x) - \partial_\nu A_\mu(x)$, which is gauge invariant.
Therefore, the total QED Lagrangian is gauge invariant. From the definition of A_μ, a mass term for the photon field $L_m = \frac{1}{2} m^2 A_\mu A^\mu$ is excluded, because A_μ is not gauge invariant.

2.2.2 Quantum Chromodynamics

Quantum Chromodynamics (QCD) [1, 2] is a gauge theory, which is based on the SU(3) symmetry group. QCD describes the strong interaction of coloured quarks and gluons within the Standard Model. The quarks are described by colour triplets that are represented as

$$q_f^T \equiv (q_f^1, q_f^2, q_f^3), \tag{2.10}$$

with $1, 2, 3$ standing for red, green and blue. The gluons correspond to the eight generators of the SU(3) symmetry group.

The Lagrangian of QCD consists of two parts: one for the quarks and one for the gluons

$$L_{strong} = L_{quark} + L_{gluon}. \tag{2.11}$$

Similarly to the calculation for the QED Lagrangian, the Lagrangian of free quarks $L_{quark} = \Sigma_{f=1}^{6} \bar{q}_f (i\gamma^\mu \partial_\mu - m_f) q_f$ is used as a starting point for the calculation of the QCD Lagrangian. Local gauge invariance is achieved by introducing 8 gauge fields. Those gauge fields are related to the eight massless gauge bosons, the gluons, of the strong interaction. In addition, the normal derivative in the Lagrangian of free quarks is substituted with a covariant derivative $D_\mu \equiv \partial_\mu + ig\frac{\lambda_a}{2} \mathrm{G}_\mu^a(x)$

$$L_{quark} = \Sigma_{f=1}^{6} [\bar{q}_f i\gamma^\mu (\partial_\mu + ig\mathrm{G}_\mu) q_f - m_f \bar{q}_f q_f]. \tag{2.12}$$

Eq. 2.13 describes the gluon part in the QCD Lagrangian Eq. 2.11

$$L_{gluon} = -\frac{1}{4}\Sigma_{a=1}^{8} \mathrm{G}_{\mu\nu}^{a} \mathrm{G}^{a\mu\nu}. \tag{2.13}$$

Due to the fact that the SU(3) is a non-abelian group, the last term of Eq. 2.14 does not vanish.

$$\mathrm{G}_{\mu\nu} = \partial_\mu \mathrm{G}_\nu^a - \partial_\nu \mathrm{G}_\mu^a + g f^{abc} \mathrm{G}_\nu^b \mathrm{G}_\mu^c. \tag{2.14}$$

Therefore, in contrast to the quarks, which interact through the mediation of gluons, gluon fields are able to self-interact. Based on the self-interaction of gluon fields, the effective coupling constant of the strong interaction is energy dependent. The larger the distance between two quarks, the larger the effective strong coupling constant. This effect is called confinement and explains why quarks and gluons have never been observed free. Another very important property of the strong coupling constant is observed at short distances, called asymptotic freedom. The strong coupling constant converges asymptotically against zero for small distances, so that quarks and gluons can be treated as free and their interactions can be calculated with perturbation theory.

2.2.3 Electroweak Theory

The electroweak theory [1] describes the unification of the weak interaction with the electromagnetic interaction and was introduced by L. Glashow, A. Salam and S. Weinberg (GSW theory). The symmetry group of the electroweak theory is given by

$$SU(2)_L \otimes U(1)_Y. \tag{2.15}$$

The Lagrangian of the electroweak theory is

$$L_{EW} = \underbrace{\sum_{j=1}^{3} i\bar{\psi}_j(x)\gamma^\mu D_\mu \psi_j(x)}_{\text{part for the fermions}} \underbrace{-\frac{1}{4} B_{\mu\nu}B^{\mu\nu} - 14 W_{\mu\nu}^j W_j^{\mu\nu}}_{\text{part for the gauge field}}, \tag{2.16}$$

if invariance under local gauge transformations is required. In this equation D_μ describes the covariant derivative

$$D_\mu = \partial_\mu - ig\frac{\sigma_j}{2} W_\mu^j(x) - ig' Y B_\mu(x). \tag{2.17}$$

The fermionic part of the Lagrangian describes the kinetic energy of the fermions and their interaction with each other and the covariant derivative describes the interaction with the gauge field. It is worth mentioning that no mass term for the fermions is allowed. If there is a mass term, there will be a mixture of the left-handed multiplets with the right-handed singlets. Therefore, the local gauge invariance would be violated, since the weak interaction only couples to left-handed fermions.

The second part of the Lagrangian describes the gauge fields. Again, there is a term for the kinetic energy and a term that describes the self interaction between the gauge fields. In this part of the Lagrangian a term for the mass is not included, in order to avoid a violation of the invariance of local gauge transformations.

At the end in the GSW theory there is no mass for the gauge fields and fermions. Nonetheless, the weak gauge bosons $W^\pm$ and Z have large masses, as confirmed by the experiments [1, 3]. Therefore, an additional mechanism is needed to describe those masses. The solution used in the SM is the Higgs Mechanism.

2.3 The Higgs Mechanism

The Higgs mechanism was introduced by Peter Higgs in 1964 [4, 5]. With the Higgs mechanism the production of particle masses will be described by spontaneous symmetry breaking without violation of the gauge invariance of the Lagrangian.

A scalar and complex SU(2) doublet ϕ is introduced with the hypercharge $Y = 1$,

$$\phi(x) = \begin{pmatrix} \phi^{(+)}(x) \\ \phi^{(0)}(x) \end{pmatrix} = \sqrt{\frac{1}{2}} \begin{pmatrix} \phi_1(x) + i\phi_2(x) \\ \phi_3(x) + i\phi_4(x) \end{pmatrix} \tag{2.18}$$

and the Lagrangian

$$L_{Higgs} = (D_\mu \phi)^\dagger D^\mu \phi - V(\phi), \tag{2.19}$$

where D_μ is the covariant derivative

$$D_\mu = \partial_\mu + ig \sum_{j=1}^{3} L_j W_\mu^j + i\frac{g'}{2} Y B_\mu, \tag{2.20}$$

which builds up the gauge invariance. In Eq. 2.19, $V(\phi)$ describes the most general and renormalizeable potential, which is invariant under a $SU(2)_L \otimes U(1)_Y$ phase space transformation

$$V(\phi) = \mu^2 \phi^\dagger \phi + \lambda(\phi^\dagger \phi)^2. \tag{2.21}$$

The potential depends on the choice of μ and λ. One has to distinguish between 3 cases:

- $\mu^2 > 0$, $\lambda < 0$: The potential is rotationally symmetric with a trivial ground state ($\phi = 0$) and therefore the potential is gauge invariant. This results in a scalar particle with the mass μ and a quartic self coupling λ. The $W^\pm$ and Z do not acquire any mass.
- $\mu^2 \neq 0$, $\lambda < 0$: The vacuum is unstable because the potential is boundless.
- $\mu^2 < 0$, $\lambda > 0$:

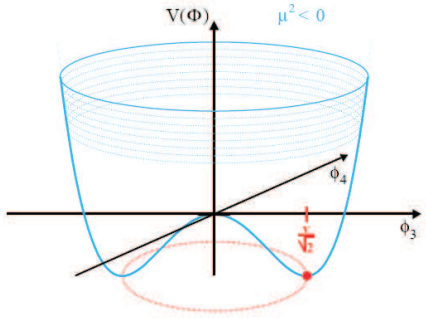

Figure 2.2: Potential for $\mu^2 < 0$ and $\lambda > 0$.

The potential resembles to a mexican hat, see Fig. 2.2. Instead of having a trivial minimum at the origin, it has an degenerate ground state with rotational symmetry. The groundstate is given by

$$-\frac{\mu^2}{2\lambda} = \frac{v^2}{2}, \tag{2.22}$$

with the vacuum expectation value v. Thus, one can have a spontaneous symmetry breaking.

$\phi(x)$ is expanded using Eq. 2.22 by means of perturbation theory. Regarding a rotation in phase space, the choice of the ground state is arbitrary. Therefore, it can be fixed to $\phi_1 = \phi_2 = \phi_4 = 0$ and $\phi_3 = v$ at

$$\phi_0(x) = \frac{1}{\sqrt{2}} \begin{pmatrix} 0 \\ v \end{pmatrix}. \tag{2.23}$$

The ground state is invariant with respect to a $U(1)_{em}$ symmetry, which is a subgroup of $SU(2)_L \otimes U(1)_Y$. Then one expands $\phi(x)$ about the ground state $\phi_0(x)$ and gets

$$\phi(x) = \begin{pmatrix} 0 \\ v + H(x) \end{pmatrix} \tag{2.24}$$

for the complex and scalar Higgs SU(2) doublet.

Once the Higgs field is chosen the underlying $SU(2)_L \otimes U(1)_Y$ symmetry is broken, called spontaneous symmetry breaking. Only $U(1)_{em}$ symmetry remains leaving the photon massless. From the symmetry breaking the W and Z boson acquire mass.

By the choice of the Higgs SU(2) doublet the electroweak theory has four degrees of freedom. Three degrees of freedom are absorbed by the longitudinal polarization of the gauge bosons, and the remaining one implies the existence of another particle, the so-called Higgs boson.

From the considerations above the Lagrangian of the Higgs field is

$$\begin{aligned} L_{Higgs} \;=\; & \underbrace{\frac{1}{2}\partial_\mu H \partial^\mu H}_{\text{kinetic part}} + const \\ & \underbrace{+\frac{1}{4}g^2 v^2 W_\mu^+ W^{-\mu} + \frac{1}{8}(g^2 + g'^2) v^2 Z_\mu Z^\mu - \lambda v^2 H^2}_{\text{mass terms}} \\ & \underbrace{+\frac{1}{2}g^2 v H W_\mu^+ W^{-\mu} + \frac{1}{4}(g^2 + g'^2) v H Z_\mu Z^\mu}_{\text{tri linear } HW^+W^- \text{ and } HZZ \text{ coupling}} \\ & \underbrace{+\frac{1}{4}g^2 H^2 W_\mu^+ W^{-\mu} + \frac{1}{8}(g^2 + g'^2) H^2 Z_\mu Z^\mu}_{\text{quadrilinear } HHW^+W^- \text{ and } HHZZ \text{ coupling}} \\ & \underbrace{-\lambda v H^3 - \frac{1}{4}\lambda H^4}_{\text{Self coupling of the Higgs field}}. \end{aligned}$$

Looking now only at the mass terms of the Lagrangian, the masses of the gauge bosons can be read directly

$$m_W = \frac{1}{2} v g, \tag{2.25}$$

$$m_Z = \frac{1}{2}\sqrt{g^2 + g'^2}, \tag{2.26}$$

$$m_H = v\sqrt{2\lambda}. \tag{2.27}$$

where v is the vacuum expectation value which can be calculated from the Fermi constant G_F

$$v = \sqrt{\frac{1}{\sqrt{2}G_F}} = 246 \text{ GeV}. \tag{2.28}$$

λ remains the only free parameter of the Higgs sector in the Standard Model, which has to be determined experimentally by the measurement of the Higgs boson mass.

Using the Higgs mechanism the mass terms of the gauge bosons can be determined directly from the Lagrangian, which is in contrast to the determination of the mass of the fermions. Those have to be added ad hoc via the Yukawa coupling of the fermions to the Higgs field. In this way the Lagrangian of the Higgs boson gets an additional term, from which the fermion masses can be directly determined. For the fermion mass one gets

$$m_f = \frac{1}{\sqrt{2}} g_f v, \tag{2.29}$$

with the coupling constant g_f being a free parameter of the SM.

2.3.1 Properties of the Higgs Boson

The Higgs boson couples generally to massive particles. The coupling to massless particles such as gluons or photons can be realized via loops of massive particles. In the SM, the possible Higgs couplings are predicted for a given Higgs mass.

Since the Higgs boson couples to mass it will usually decay into the heaviest possible combination of daughter particles. This is independent of whether the decay particles are bosons or fermions. As the Higgs boson is a scalar particle, it has spin 0. Therefore, if it decays into fermions the two daughter particles must have opposite helicities.

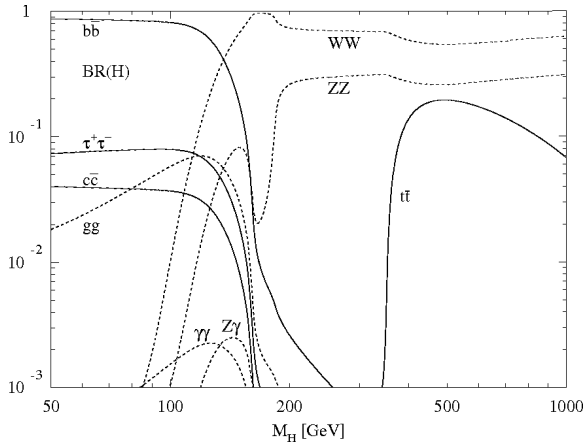

Figure 2.3: Branching ratio of the Higgs boson as a function of its mass [6].

In Fig. 2.3, the different branching ratios, $BR(H)$, are plotted as a function of Higgs mass, which can aid in the decision of what signatures have to be searched for a given Higgs boson mass. For small Higgs boson masses the decay into $b\bar{b}$ dominates with a branching ratio of nearly 90% in comparison to the decay into $\tau^+\tau^-$ with 10%. That comes from the fact that the decay width depends quadratically on the fermion masses, and the mass of the b-quark is nearly a factor of three higher than the mass of the τ. For a Higgs mass above 130 GeV/c^2 the decay

into W^+W^- is dominant and between 130 GeV/c^2 $< m_H <$ 180 GeV/c^2 the decay into ZZ is also important. Contrary to what one might think at first the decay into W^+W^- outweighs the decay into ZZ, even though the Z boson is heavier than the W boson. That is due to the fact that W^+ and W^- are not identical and therefore there are more possibilities for a decay into W^+W^- compared to the decay into ZZ. From a mass of $m_H = 350$ GeV/c^2 the decay into $t\bar{t}$ becomes possible but the dominant decay is still the decay into W^+W^-.

Although, the SM describes very well the current experimental results, the Higgs boson mass is still an unknown parameter. But from theory some limits are set.

- **Upper Limit:** The upper limit for the Higgs boson mass comes from the unitarity of the WW scattering amplitude. In order not to violate this, there must be a Higgs boson below a maximum mass. Otherwise the amplitude would increase to infinity, which would result in a violation.
$$m_H \lesssim 1 \text{ TeV/c}^2.$$

- **Lower Limit:** The lower limit comes from the fact that the vacuum has to remain stable. Looking at the potential, in Fig. 2.2, one recognizes that for small values of λ the potential becomes flatter, which could cause an instability of the vacuum. Therefore, λ must have a minimum value, and since the Higgs boson mass is proportional to $\sqrt{\lambda}$ (Eq. 2.27), the Higgs boson mass must have a minimum value, as well.
$$m_H > 7 \text{ GeV/c}^2.$$

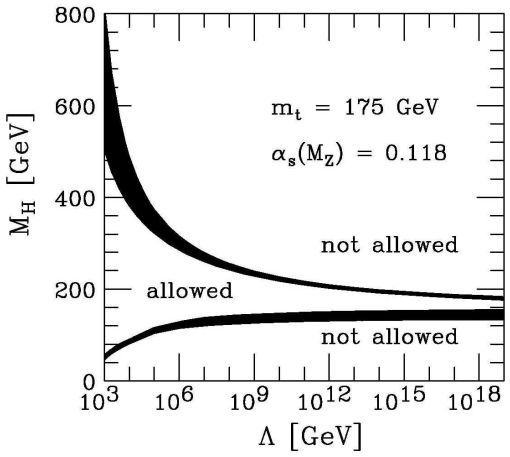

Figure 2.4: "Chimney plot": Higgs mass as a function of Λ [7].

In Fig. 2.4 the Higgs boson mass is shown as a function of Λ, where Λ describes the energy up to which the SM is valid. The upper prohibited range comes from the requirement of the unitarity of the WW scattering amplitude and the lower limit from the requirement of vacuum stability. For example, if the SM were valid up to the so-called GUT scale ($\Lambda = 10^{16}$ GeV), one would get 130 GeV/c^2 $< m_H <$ 180 GeV/c^2 for the limits of the Higgs boson mass.

In order to constrain the Higgs boson mass furthermore a global fit was developed. The global fit considers precision measurements and theoretical assumptions. An essential part for this is the sensitivity of the W mass on electroweak radiation corrections.

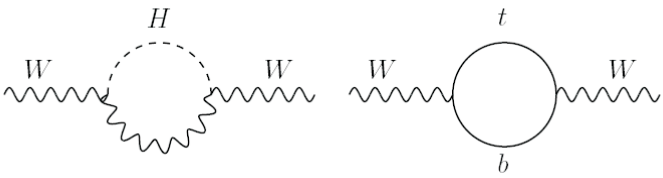

Figure 2.5: Radiation corrections.

In Fig. 2.5 possible radiation corrections are shown, with a Higgs boson or top quark within the loop. By calculating these radiative corrections the following relations can be shown

$$\Delta m_W \propto \ln(m_H) \tag{2.30}$$

and

$$\Delta m_W \propto m_t^2. \tag{2.31}$$

Therefore the sensitivity of the W mass is highly dependent on the top mass, but only weakly on the Higgs boson mass. The Higgs boson mass can not only be determined by radiative corrections, such as the top mass, since the accuracy would be much too low.

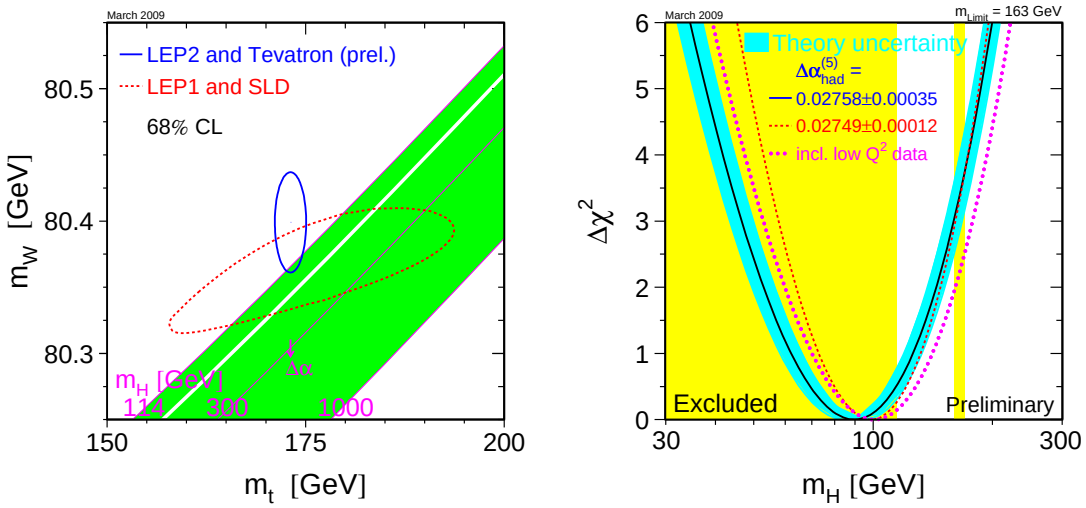

(a) (b)

Figure 2.6: (a) global fit (b) χ^2 as a function of the Higgs boson mass [8].

In Fig. 2.6(a) the global fit with its relations to the masses and indirect and direct measurements from LEP and Tevatron are shown. Using the global fit, the theory of a light Higgs boson can be supported. Fig. 2.6(b) shows the χ^2 of the fit as a function of the Higgs boson mass. From the χ^2 the Higgs boson mass can be determined by an order of magnitude

to $m_H = 88^{+53}_{-35}$ GeV/c^2 and within a confidence level of 95% the Higgs boson mass has to be smaller than 163 GeV/c^2.

2.3.2 Measurements from LEP and Tevatron

LEP and also Tevatron have not found the Higgs boson yet, but both of them were or are able to set exclusion limits on the Higgs boson mass. The following two sections describe briefly the results from these colliders.

Limits from LEP

From the combination of LEP1 data between 1991 and 1994, the existence of a very light Higgs boson could be excluded. A new lower limit was set to

$$m_H > 60.2 \text{ GeV/c}^2 \text{ with } 95\%\text{CL}. \tag{2.32}$$

LEP2 gave the possibility to search for the Higgs boson up to a mass of 115 GeV/c^2, but found no evidence in this range. The combination of all LEP2 data between 1996 and 2000 gave the newest lower limit for the Higgs boson mass [9], which is valid still today

$$m_H > 114.4 \text{ GeV/c}^2 \text{ with } 95\%\text{CL}. \tag{2.33}$$

Limits from Tevatron

With newest measurements from Tevatron the Higgs boson is excluded between
160 GeV/c^2 $< m_H <$ 170 GeV/c^2 [10], see Fig. 2.7.

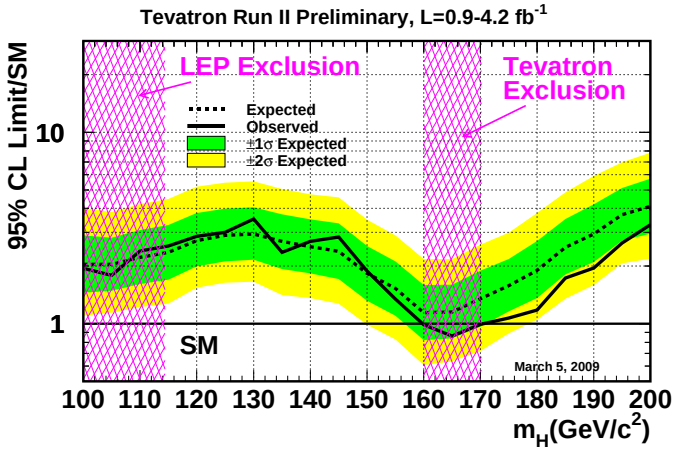

Figure 2.7: 95% C.L. limits on the ratio to the cross section, as a function of the Higgs boson mass. The result comes from the combined CDF and DØ analysis [10].

2.4 Phenomenology of pp Collisions

Understanding the proton-proton interactions requires understanding the proton structure. The proton structure is described by the proton structure functions. In the following sections the main issues for the calculation of hard cross section are described and finally some QCD phenomenological models are explained which are very important for the analysis.

2.4.1 The Parton Model and Parton Distribution Functions

The parton model was introduced by Feynman in 1969 and is used to describe phenomena at high energies. In this model each proton with energy and momentum P^μ is regarded as a system of sub-particles: the three valence quarks, the sea quarks and the gluons. These sub-particles are called partons, which carry energy and momentum in the range between xP^μ and $(x+dx)P^\mu$ with $0 < x < 1$, written as $p_i(x)dx$.

For an exact description of proton-proton collisions, the momentum distributions of the partons have to be well known. The so-called Parton Distribution Functions (PDFs) are determined by different collaborations (ZEUS,H1,BCDMS,E665,NMC,CCFR) in deep inelastic scattering (DIS) of electrons, muons and neutrinos with nucleons. Several approaches are currently available for the description of PDFs, e.g. by the MRST [11, 12, 13] group or by the CTEQ [14] group. Fig. 2.8 shows the PDFs from the CTEQ6.1 PDF set for a Q^2 value of 100 GeV^2.

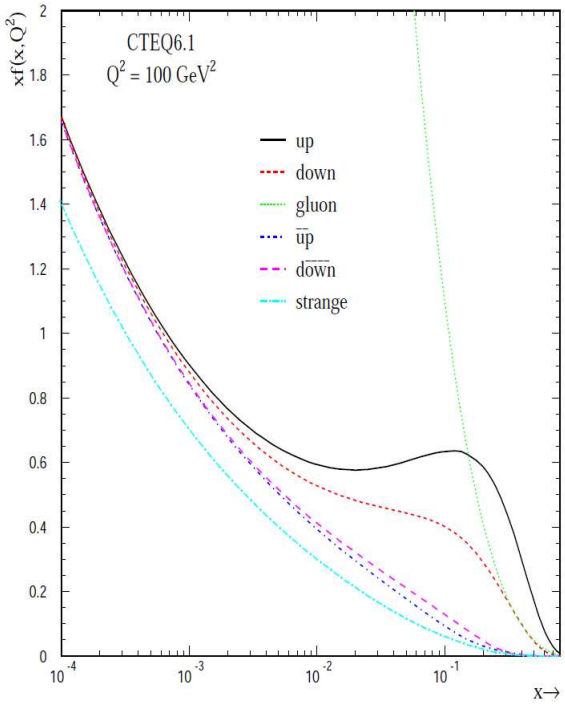

Figure 2.8: Parton Distribution Functions from the CTEQ6.1 set are plotted for $Q^2 = 100$ GeV^2.

PDFs are determined by making a global QCD fit to data, which introduces an uncertainty in the estimate. In addition to the experimental uncertainty, an uncertainty on the theoretical calculations has to be included such as e.g. NNLO and higher order contributions from DGLAP.

For a detailed description of the different sources of uncertainty see [14, 15]. Due to the many different uncertainties, it is not only important to get the best estimate for the PDFs, the uncertainties on the PDFs have also to be understood. In general the largest uncertainty comes from the gluon distribution.

For the calculation of PDF uncertainties two different approaches are available: the Lagrange Multiplier [16] and the Hessian technique [17]. Both the CTEQ group and the MRST group use the Hessian technique. In the Hessian method a large matrix is determined with dimensions taken from the number of free parameters N_p of the fit; e.g. 20×20 for CTEQ and 15×15 for MRST. This matrix has to be diagonalized, which results in a set of eigenvector directions, 20 for CTEQ and 15 for MRST. Each PDF error is then determined by varying along plus or minus of each eigenvector direction, which results in 40 PDF error sets for CTEQ and 30 for MRST.

For this thesis the approach of the CTEQ group is used.

2.4.2 Cross Section

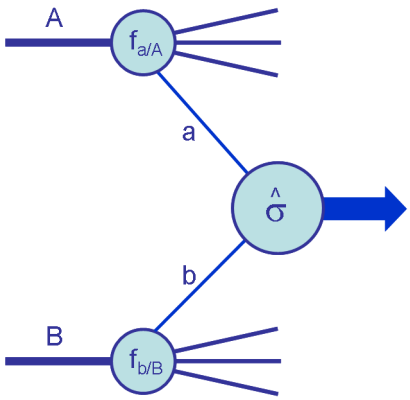

Figure 2.9: Schematical view of a hard scattering process.

The sub-processes in a hadronic collisions can be separated into two types, hard and soft. For both the underlying theory is the QCD, but the handling is different. Hard processes, like high p_T jet production, can be described using perturbative QCD calculation with an adequate precision [18]. In contrast, soft processes, like underlying event, described in section 2.4.5, are dominated by non-pertubative effects. Separation between the two energy regimes is achieved with the introduction of a factorization scale μ_F, which is usually chosen at the order of the scale Q of the hard process. In addition, due to renormalisation of the QCD expansion, the renormalisation scale μ_R is introduced at which the coupling constant of the strong interaction is evaluated. Usually, both scales are chosen to be equal.

The cross section σ_{AB} of a hard process, which is schematically shown in Fig. 2.9, is given by the following formula [18]:

$$\sigma_{AB} = \int \mathrm{d}x_a \mathrm{d}x_b f_{a/A}(x_a, \mu_F^2) f_{b/B}(x_b, \mu_F^2) \times [\hat{\sigma}_0 + \alpha_s(\mu_R^2)\hat{\sigma}_1 + ...]_{ab \to X}. \tag{2.34}$$

The dependence of the cross section calculation on the choice of μ_F and μ_R decreases with increasing order of the correction. A infinite order pertubative cross section calculation is independent of the choice of μ_F and μ_R.

2.4.3 Higher order QCD corrections

The cross section, described in Sect. 2.4.2, is calculated with a pertubative expansion at least at leading order. In order to include next-to-leading order QCD corrections, virtual corrections and initial and final state radiation (see Sect. 2.4.6) have to be taken into account. Approximately, the total cross section can be corrected for higher order effects with the *k-factor*, the ratio between the higher order cross section and the leading order cross section.

2.4.4 Multiple Proton Interactions

The total cross section for inelastic interactions is several orders of magnitude larger than the cross sections for the interesting hard interaction processes. Therefore, a typical bunch crossing is characterized by multiple soft proton-proton interactions. At the LHC, at a centre of mass energy of 14 TeV, 23 inelastic proton-proton collisions per bunch crossing are expected. These events are dominated by events with a small momentum transfer. They are called minimum bias events.

2.4.5 Underlying Event

The underlying event (UE) consists of beam remnants and multiple parton interactions. In order to describe the UE, non-pertubative phenomenological models are needed. In ATLAS two different models are currently used. One is provided by the JIMMY [19] package, which is linked to HERWIG [20] event generator and the second is provided by the PYTHIA [21] event generator. The different Monte Carlo generators are described in Sect. 5.1. From comparison studies between the two packages it has been shown that JIMMY predicts twice as much UE as PYTHIA at the LHC.

2.4.6 Parton Shower

Fig. 2.10 shows a schematical view of the basic structure of a showering and hadronizing event, which is going to be described in this and the following section.

In hadronic collisions, the partons which participate in the hard process may radiate quarks or gluons, which is called initial state radiation (ISR). There is also the possibility to produce radiation after the scattering process, called final state radiation (FSR). Mainly the radiated quarks and/or gluons have very low energy and are nearly collinear with the hard scattered partons. Processes like $q\bar{q} \rightarrow Z^0 \rightarrow e^+e^-$ contain initial state QCD radiation. The radiated quarks or gluons have again the possibility to radiate, which leads to showers of partons. Using the DGLAP[3] equation the relative probability for radiating a gluon or a quark by the parton can be determined. For both ISR and FSR, the structure of the showers is given by a $1 \rightarrow 2$ process, specifically $q \rightarrow qg$, $g \rightarrow gg$ and $g \rightarrow q\bar{q}$. QED radiation is also possible but it is not so important for the following analysis. The probability for one of these processes to happen depends on the virtuality scale Q^2 and the relative transverse momentum. Shower evolution is contained to a cutoff value Q_0, typically around 1 GeV for QCD processes. There is also a defined upper limit Q_{max}. Above Q_{max} showers are matched to the hard interaction itself.

[3] Dokshitzer-Gribov-Lipatov-Altarelli-Parisi equation to describe the evolution of QCD.

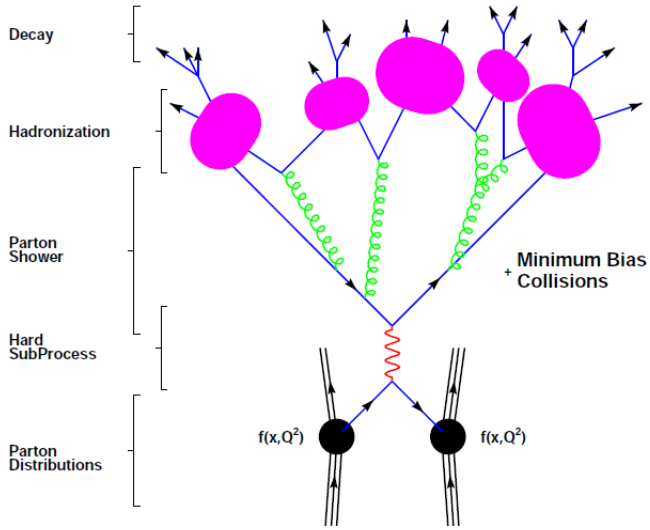

Figure 2.10: Schematic view of the basic structure of an event including showering and hadronization.

2.4.7 Hadronization

As described in Sect. 2.2.2, perturbative QCD in terms of quarks and gluons is only valid at short distances. At long distances pertubative QCD can not be used. At this point the coloured quarks and gluons are combined to colourless hadrons, since they cannot be free in the final state because of confinement. This process is called hadronization or fragmentation. In order to describe this process, three different models are available: the string fragmentation (SF), the independent fragmentation (IF) and the cluster fragmentation (CF). The models, which are currently used in ATLAS are the SF [22, 23] and the CF [24, 25].

3 Experimental Setup

The LHC provides the possibility to answer many open question concerning the SM and beyond. In this chapter the Large Hadron Collider (LHC) and the ATLAS detector is described. The first section gives a short overview over the LHC and the second section describes the ATLAS detector with its main components.

3.1 The Large Hadron Collider

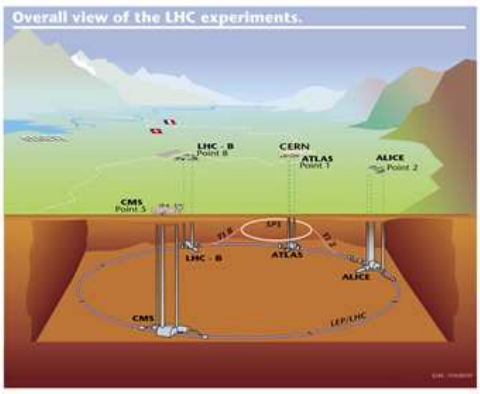

Figure 3.1: Schematic view of the Large Hadron Collider.

The LHC is the biggest experiment ever built. It is a proton-proton collider and is located in the old LEP tunnel $70 - 100$ meters underground at CERN in Geneva. The LHC has a circumference of 27 km and a nominal centre of mass energy of 14 TeV. Each proton beam includes 2808 bunches with about 10^{11} protons per bunch. The LHC provides a collision rate of 40 MHz, which results in a collision every 25 ns. The event rate, R, of a special process can be characterized by the cross section σ of this process and by the instantaneous luminosity $\mathcal{L}$. It is given in Eq. 3.1.

$$R = \mathcal{L} \cdot \sigma. \tag{3.1}$$

The instantaneous luminosity is defined as

$$\mathcal{L} = n_b \frac{n_1 \cdot n_2}{A_{eff}} f, \tag{3.2}$$

with n_b the number of bunches, n_1 and n_2 the number of protons per bunch, f the collision frequency and the effective interaction area $A_{eff} = 4\pi\sigma_x\sigma_y$. The design luminosity of the LHC is $\mathcal{L} = 10^{34}$ cm^{-2}s^{-1}.

Fig. 3.2 shows the cross section of various physics processes as a function of the centre of mass energy.

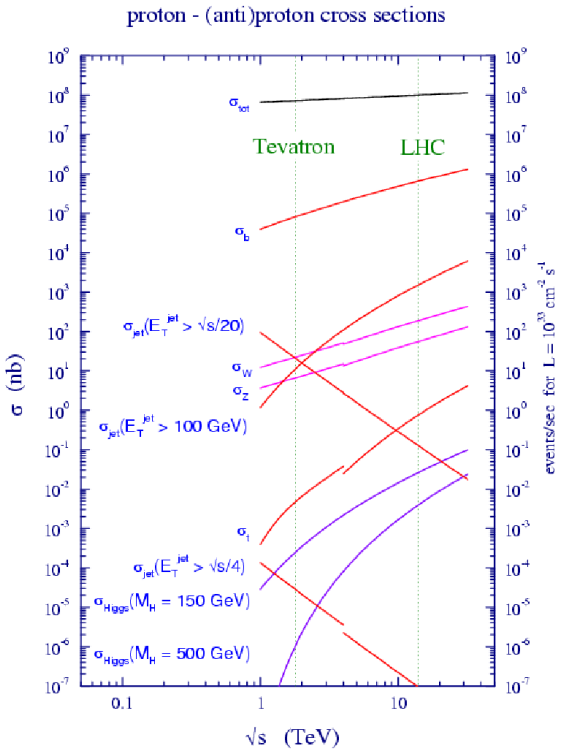

Figure 3.2: Expected cross section and event rate for proton-proton collisions [18].

Due to the low cross section for interesting processes a large integrated luminosity is needed to reach the significance for an observation or a discovery.

The LHC has four experiments ATLAS, CMS, ALICE and LHCb. The ATLAS experiment is multi-purpose detector, as is CMS. In the following section the ATLAS detector is described in more details. ALICE is a heavy-ion experiment with the purpose of studying the equation of state of matter at high energy densities. In this case lead ions will collide with a centre of mass energy up to 1150 TeV. The LHCb detector is specialized in the study of particles that contain b-quarks.

3.2 The ATLAS Experiment

The ATLAS detector is a multi-purpose detector with a height of 22 m and a length of 45 m. It weighs $6.4 \cdot 10^{16}$ kg and is located at Point 1 on the LHC ring 100 metres below the surface. The ATLAS detector is the biggest of the four experiments at the LHC.

Based on the large physics program of the LHC, the ATLAS detector has to fulfil a lot of requirements, such as a very good electromagnetic calorimeter for the electron and photon identification and measurement or a full-coverage hadronic calorimeter. The ATLAS detector, shown in Fig. 3.3, consists of five different detector components: the magnet system, the inner detector, the calorimeter system, the muon system and the trigger. These systems are placed around the beam axis and designed such that they complement each other to provide the best

results.

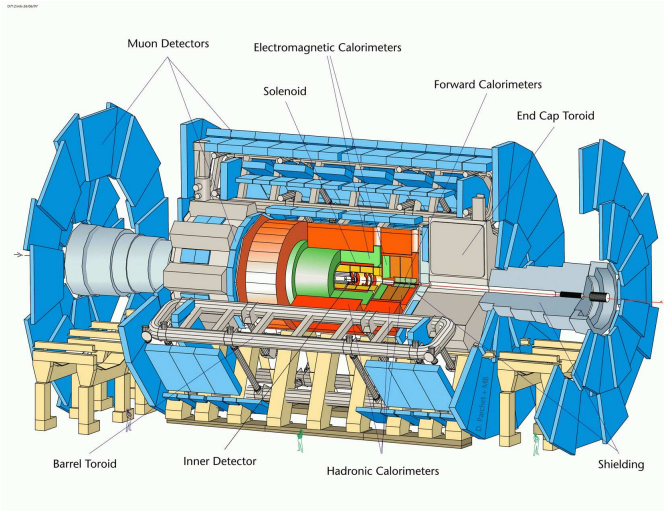

Figure 3.3: Schematic view of the ATLAS detector [26].

The coordinate system of the ATLAS detector is chosen such that the z-axis points in the direction of the beam axis and the x-y plane is transverse to it. The x-axis points from the interaction point to the center of the LHC ring and the y-axis points upwards. In addition, cylindric coordinates can be used to parametrise the detector geometry. ϕ is defined as the azimuthal angle perpendicular to the z-axis and θ is defined as the polar angle perpendicular to the x-axis with the z-axis at $\theta = 0°$. The angle of a particle is described via the pseudo rapidity, which is defined as

$$\eta \equiv -\frac{1}{2} \ln \left(\frac{|\vec{p}| + p_z}{|\vec{p}| - p_z} \right) = -\ln \left(\tan \frac{\theta}{2} \right) \tag{3.3}$$

In the following the main components of the ATLAS are briefly described, for a complete description see [27, 28].

3.2.1 Magnet System

The magnet system, as shown in Fig. 3.4, is one of the central components of the ATLAS detector and consists of two parts, the toroid and the solenoid system. The solenoid system is used for the momentum measurement of charged particles in the inner detector. It is placed inside the EM calorimeter and produces a nearly homogeneous field of 2T. The solenoid is a superconducting magnet, which must be kept at a temperature of 4.5 K. The solenoid covers a pseudo rapidity range up to $|\eta| < 2.7$. The toroid system, consisting of three large air-core toroids, one barrel toroid and two end-cap toroids, encloses the electromagnetic and hadronic calorimeter. Each toroid consists of eight air coils, which are radially and symmetrically arranged around the beam axis. The toroid magnetic system is used for the transverse momentum measurement of the muons. The barrel toroid has a bending power of 2 to 6 T·m and covers a range of $0 \leq |\eta| \leq 1.3$. Contrary to that, both end-cap toroids provide a bending power of 4 to 8 T·m and cover a range of $1.6 \leq |\eta| \leq 2.7$. In the range between $1.3 < |\eta| < 1.6$ the barrel toroid overlaps with the end-cap toroids.

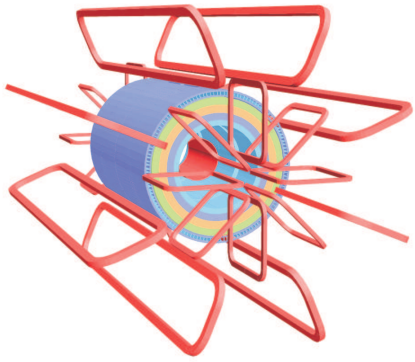

Figure 3.4: Schematic view of the magnet system including the solenoid and the three toroids [27].

3.2.2 Inner Detector

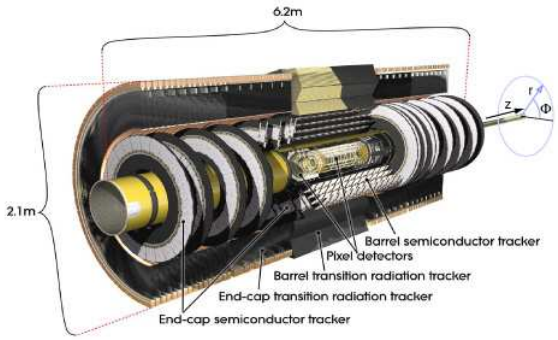

Figure 3.5: Schematic view of the ATLAS inner detector [27].

The inner detector, shown in Fig. 3.5, consists of three sub-detectors: the silicon pixel detector, the silicon strip detector (SCT) and the transition radiation tracker (TRT). The first two are solid state detectors while the third one is a gaseous detector. The inner detector is used for charged particles for the track and vertex reconstruction starting from $p_T = 0.5$ GeV/c. The innermost part of the inner detector is the silicon pixel detector, which is very close to the interaction point and gives high granularity. The silicon pixel detector consists of three barrel cylinders around the beam axis and three disks on each side. It is mainly used to find the vertex and covers a range up to $|\eta| = 2.5$. The SCT surrounds the pixel detector and consists of 4 double layers in the barrel region ($|\eta| < 2.4$), using a small stereo angle (40 mrad) to provide a z-axis measurement. In addition, the SCT has 9 end-cap disks covering a pseudo rapidity region 1.4 to 2.5. The outermost part of the inner detector is covered by the TRT, which consists of three parts - a barrel and two end-caps. The TRT is made of drift straw tubes parallel to the beam direction, which are filled with gas and covered by a radiator. The TRT works with two different effects: transition radiation and drift-time. The transition radiation is used to identify particles via their probability to produce transition radiation for a given transverse momentum. Electrons begin to produce transition radiation for a transverse momentum larger than 1 GeV/c contrary to pions which produce transition radiation above 100 GeV/c. The combination of the

solid state detectors with the TRT gives a very good pattern recognition and high precision in the measurements of coordinates. Overall the inner detector provides 43 space points per track, three space points by the pixel detector, four by the SCT and 36 by the TRT.

3.2.3 Calorimeter System

The ATLAS calorimeter contains a liquid argon (LAr) accordion calorimeter, a tile calorimeter, a LAr hadronic end-cap calorimeter (HEC) and a LAr forward calorimeter (FCAL). The calorimeter system is used for the energy measurement of the high energetic particles up to a range of $|\eta| = 4.9$.

Electromagnetic Calorimeter

The electromagnetic calorimeter (EM calorimeter) is a sampling calorimeter with lead as absorber and LAr as the active material. It is divided into a barrel part, two end-caps, one on each side and a pre-sampler. The barrel covers a range up to $|\eta| = 1.475$ with a thickness larger than 24 radiation lengths (X_0) and the two end-caps cover a range of $1.375 < |\eta| < 3.2$ with a thickness larger than 28 X_0. In the region which is used for precision measurements ($|\eta| < 2.5$) the EM calorimeter is split into three longitudinal segments with different granularities: the strip section, the middle section and the back section. The strip section has a very fine granularity of $\Delta\eta \times \Delta\phi = 0.0031 \times 0.0982$. It acts as a pre-shower detector and provides precise position measurements in η. The middle section with granularity of $\Delta\eta \times \Delta\phi = 0.025 \times 0.0245$ is used for energy measurements. It absorbs most of the energy from EM showers. The third section is used for leakage control, it absorbs the remaining energy from the EM showers and has a granularity of $\Delta\eta \times \Delta\phi = 0.050 \times 0.0245$. For the high η region ($2.5 < |\eta| < 3.2$), the EM calorimeter is split into two longitudinal sections with a coarser granularity, which is sufficient to fulfil the physics requirements such as for reconstruction of jets and missing transverse energy.

In 2006 a part of the EM barrel and end-cap calorimeter have been exposed to the CERN SPS H8 electron test-beam to determine the resolution and the response properties of the EM calorimeter. After noise subtraction the measurements are fitted with Eq. 3.4

$$\frac{\sigma_E}{E} = \frac{a}{\sqrt{E}} \oplus b, \tag{3.4}$$

where a describes the stochastic term and b the constant term. From the fit the parameters were determined to $a = (10.1 \pm 0.01)\% \times \sqrt{\text{GeV}}$ and $b = (0.7 \pm 0.04)\%$, which are in a good agreement with results from Monte Carlo simulations [29].

Hadronic Calorimeter

The hadronic calorimeter surrounds the EM calorimeter and covers a range up to $|\eta| = 4.9$. It consists of three components: the tile calorimeter ($|\eta| < 1.7$), the HEC ($1.5 < |\eta| < 3.2$) and the FCAL ($3.1 < |\eta| < 4.9$). The tile calorimeter is a sampling calorimeter using iron as absorber together with a scintillator. Similar to the electromagnetic LAr calorimeter, the tile calorimeter is longitudinally split into three segments. The combined energy resolution of the electromagnetic LAr calorimeter and the tile calorimeter was estimated from test-beam to be $a = (52.0 \pm 1.0)\% \times \sqrt{\text{GeV}}$ and ($b = 3.0 \pm 0.1)\%$ for hadronic processes using Eq. 3.4 [30]. The HEC is also a sampling calorimeter, using copper as absorber and liquid argon as the active material. Finally, the FCAL has a very challenging job, due to the fact that it is close to the beamline and therefore it has to cope with a high particle flux. The FCAL is split into three sections,

one uses copper as the passive medium while the other two use tungsten. In order to increase the response time of the system, the gaps, filled with liquid argon, are smaller. The estimated resolution from test-beam measurements of 2003 for the FCAL is $a = (94.2 \pm 1.6)\% \times \sqrt{\text{GeV}}$ and $b = (7.5 \pm 0.4)\%$ using Eq. 3.4 [31].

3.2.4 Muon Chambers

The outermost part of the ATLAS detector is the muon spectrometer [27, 32]. It consists of four parts: the monitored drift tubes (MDT), the cathode strip chambers (CSC), the resistive plate chambers (RPC) and the thin gap chambers (TGC). The system is designed to measure the muon momentum of a few GeV/c up to 3 TeV/c, providing a high resolution for a standalone measurement. The range up to $|\eta| = 2.7$ is used for the momentum measurement. In addition the muon system provides a trigger system. The MDT's are used as precision measurement tracking chambers up to $|\eta| = 2.7$ except the innermost end-cap layer. In this layer CSC's are used, because of their higher rate capability and time resolution. The RPC's and TGC's are used as trigger system. The RPC's are present in the barrel region and in the end-caps the TGC's are used.

3.2.5 Data Acquisition and Trigger System

Given the high luminosity of the LHC, an event rate of 1 GHz is expected. The memory needed per event is on average 1.5 MB, which requires a very efficient data acquisition system (DAQ). The maximum storage rate is restricted to < 200 Hz, which is low compared to the total interaction rate, therefore only 1 event out of 200000 events can be stored. That means that an efficient trigger system for the physics goals is required. So, the trigger system has to fulfil two main requirements: first it has to provide a high rejection rate and second to provide an efficient selection. The trigger system in ATLAS consists of three levels: Level-1 (L1), Level-2 (L2) and the the event filter (EF). Fig. 3.6 shows the trigger system with its tree levels. L1 is a hardware trigger in contrast L2 and EF are software triggers. In addition, L2 and EF are combined to the High-Level Trigger (HLT). Each level decreases the rate of the passed events in order to give the following level more time for the data processing.

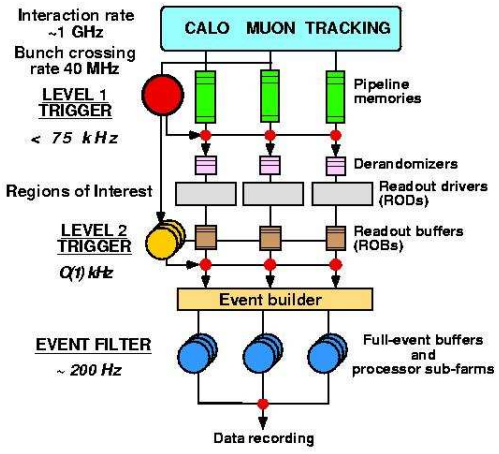

Figure 3.6: The ATLAS Trigger System with its three levels [33].

- **L1** decision is based on data from the calorimeters and the muon trigger chambers. It makes a first classification of the particles, calculation of the total and the missing transverse energy and defines a region of interest. The event rate is reduced from 40 MHz to 75 kHz.
- **L2** uses the region of interest defined by L1 but takes data from all detector components into account. Thus, the event rate is reduced from 75 kHz to 1 kHz.
- **EF** is the last level of the ATLAS trigger system and is a part of the DAQ. It has access to the full event information and can perform a much more refined event reconstruction with a more complex software. The event rate is reduced to 200 Hz.

For a more detailed description of the ATLAS trigger system see [33].

4 Phenomenology

4.1 Phenomenology of the Z Boson

The Z boson was discovered in the Super Proton Synchrotron (SPS) at CERN in 1983, which was a $p\bar{p}$ collider. The properties of the Z boson are well known from e^+e^- collisions at the Large Electron Collider (LEP) at CERN and the Stanford Linear Collider (SLC) at SLAC. The mass of the Z boson is determined with a high precision to be $m_Z = 91.1876 \pm 0.0021$ GeV/c^2 [1]. At the ATLAS experiment at the LHC the selection of Z bosons is a very important part of the physics program. The decay of the Z boson provides a very clean signature and the large production cross section, see Fig. 3.2, gives the possibility to collect a sufficiently high amount of Z bosons with the first LHC data. Due to the fact that the properties of the Z boson are well known, the selection of Z bosons are extremely important for the understanding of the detector and to tune the MC generators, which are currently used in ATLAS and described in Sect. 5.1. In addition, they are interesting for testing pertubative QCD, as well as understanding an important background for SM and beyond SM physics processes, such as the Higgs boson production. At the LHC the Z boson is produced via Drell-Yan processes (see Fig. 4.1) modified by higher order QCD corrections. For a detailed description see [34].

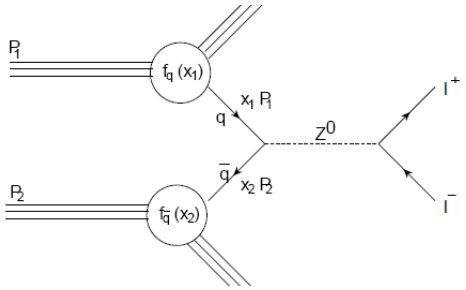

Figure 4.1: Z boson production via Drell-Yan process.

The decay properties of the Z boson are predicted by the SM. Tab. 4.1 shows the different branching ratios of the Z boson.

Z decay modes	Fraction (Γ_i/Γ) [%]
e^+e^-	3.363 ± 0.004
$\mu^+\mu^-$	3.366 ± 0.007
$\tau^+\tau^-$	3.370 ± 0.008
invisible	20.00 ± 0.06
hadrons	69.91 ± 0.06

Table 4.1: Different decay modes of the Z boson with their corresponding branching ratio [1].

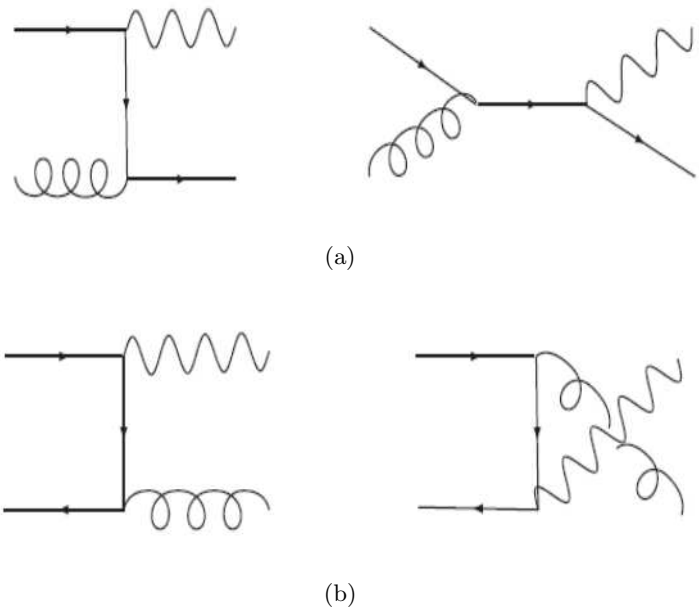

(a)

(b)

Figure 4.2: Feynman diagrams for the production of Z bosons in association with jets via Compton process (a) and $q\bar{q}$ annihilation (b).

For the production of Z bosons in association with jets two contributions are important: the Compton process and the $q\bar{q}$ annihilation. Fig. 4.2 shows the Feynman diagrams for these processes. At LHC the production is dominated by the Compton process.

4.2 Phenomenology of the Higgs Boson

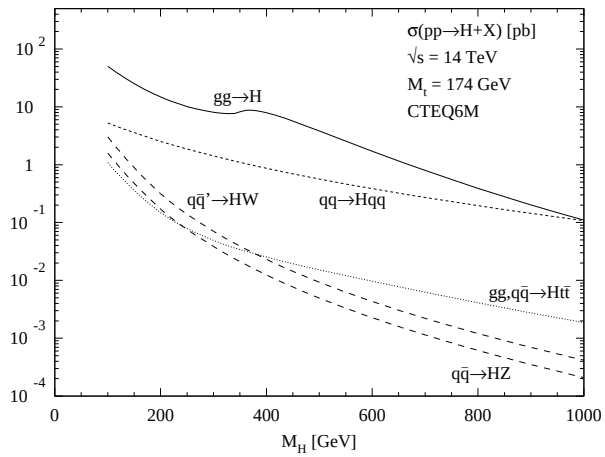

Figure 4.3: Production cross section for the SM Higgs boson as a function of its mass for a centre of mass energy of 14 TeV in proton-proton collisions. The results include fully pertubative QCD corrections [35].

The Higgs boson can be produced in different channels at the LHC, which gives the possibility to cover the entire mass range of the Higgs boson. Fig. 4.3 shows the cross section for the different production channels as a function of the Higgs boson mass for a centre of mass energy of 14 TeV. Over the whole mass range gluon fusion is the dominant process. The Higgs boson is produced via a top quark or bottom quark loop, more often from top since it is heavier. The second highest contribution to the over all production cross section comes from the Vector Boson Fusion (VBF). Other possible processes are, for example, the associated Higgs boson production with vector bosons or top quarks, however, they have a much smaller cross section compared to the dominant processes.

Concerning the decay channels of the Higgs boson, for small masses the dominant decay channel is $H \rightarrow b\bar{b}$ (see Fig. 2.3). Due to the large QCD background this channel is difficult to use for searches, since no additional signatures are available for separating the signal from the background. For small masses, $m_H < 135\,\mathrm{GeV/c^2}$, the decays to $\tau^+\tau^-$ and to photons are the most important ones. For large masses the decay to W and Z bosons become dominant.

The different cross sections and branching ratios results in many different channels for the discovery of the Higgs boson, however, concerning their sensitivity they vary considerably.

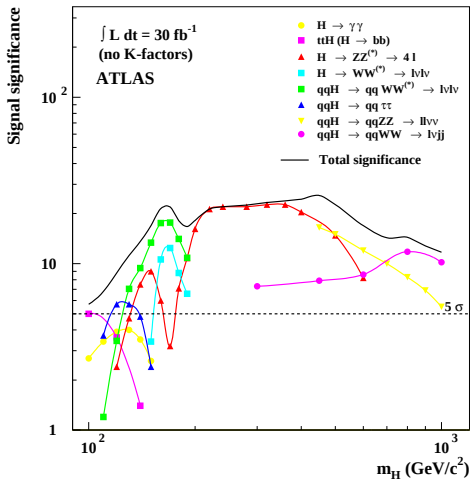

Figure 4.4: Sensitivity for a Higgs boson discovery at the ATLAS experiment [36]. The figure shows the signal significance as a function of the Higgs boson mass in the range between $100\,\mathrm{GeV/c^2}$ and $1\,\mathrm{TeV/c^2}$.

Fig. 4.4 shows the individual signal significance for the different channels and the total significance as a function of the Higgs boson mass at the ATLAS detector. For low masses one of the most promising channels is the Higgs boson production via Vector Boson Fusion with $H \rightarrow \tau^+\tau^-$ decay. This channel provides a reasonably high signal to background ratio. For the following analysis the focus is on this channel.

5 Monte Carlo Generators and Monte Carlo Datasets

5.1 Monte Carlo Event Generators

Theoretical predictions play an essential role for any particle physics experiment. The best way to to map theoretical predictions to the experimental results is the usage of the so-called Monte Carlo (MC) event generators. This section briefly describes MC generators and then goes into detail on the specific generators used in the analysis presented.

In general, generators are divided into two types, tree level matrix element generators [37] and general purpose showering and hadronization event generators [37]. Tree level matrix element generators are parton level generators, such as ALPGEN, which uses fixed order matrix elements to describe a specific final state in the lowest order - virtual corrections are not included. In addition fragmentation is not included and the final state consists of free quarks and gluons. Therefore they have to be interfaced to showering and hadronization programs. The event shape in the low p_T region is dominated by parton shower and in high p_T by the Matrix Element calculations. General purpose showering and hadronization event generators, such as PYTHIA and HERWIG, start with leading order hard sub processes. Higher order corrections are done using parton shower.

5.1.1 PYTHIA

PYTHIA [21] is a general purpose showering and hadronization generator, which can be used for generating hadronic events in $\mathrm{p}\overset{(-)}{\mathrm{p}}$, $\mathrm{e^+e^-}$ and ep collisions. It describes initial and final state radiation using Q^2-ordered parton showers, underlying evnet (UE), hadronization and decays. PYTHIA uses the Lund string hadronization model and for the modelling of the UE, PYTHIA uses colour string fragmentation and p_T-ordered parton shower. In general PYTHIA is used for $2 \to 1$ or $2 \to 2$ processes, it includes 240 different $2 \to n$ subprocesses.

5.1.2 HERWIG

HERWIG [20], like PYTHIA, is a general purpose generator that generates hadronic events in $\mathrm{p}\overset{(-)}{\mathrm{p}}$, $\mathrm{e^+e^-}$ and ep collisions. A large range of hard scattering processes is simulated together with initial and final state radiation using the angular-ordered parton shower. Hadronisation and underlying event are included in the simulation as well. The former is done by the cluster hadronization model and the latter by using the cluster fragmentation algorithm for the simulation of the underlying event. In addition HERWIG has to be interfaced with JIMMY [19], if the multiple scattering model needs to be included in the simulation of the underlying event. HERWIG covers a large number of hard $2 \to n$ scattering processes for the Standard Model and supersymmetric models.

5.1.3 ALPGEN

As mentioned before, ALPGEN [38] belongs to the tree-level matrix element generators. ALPGEN is a Monte Carlo generator, which is designed to generate events for hard multi-parton processes in hadronic collisions. It provides exact leading order matrix element calculations for a huge number of processes. It describes partonic processes, that are of interest for the LHC and the Tevatron, such as $W/Z + n\ jets$, where $n \leq 5$. ALPGEN is interfaced with PYTHIA or HERWIG to evolve the event by parton shower. In order to prevent double counting for the jets MLM-matching[1] [39, 40] is used. Jets with a transverse momentum smaller than a certain value are produced by parton shower and the others are calculated by the hard matrix element. For the following analysis ALPGEN is interfaced with HERWIG.

5.1.4 MC@NLO

MC@NLO [41] is an event generator that uses the full next-to-leading order QCD calculation for the generation of a given process. This leads to a better description of the radiation of the first parton compared to the other generators. MC@NLO uses parton showers to describe the multiple soft, collinear emissions and gives a description of the final state at hadron level. Contrary to the other standard MC generators, MC@NLO includes negative weights due to its resummation techniques, which are used for the next-to-leading order QCD corrections. On average 15% of the events produced get a weight -1. MC@NLO is interfaced with HERWIG to propagate the event through the parton shower and hadronization.

5.2 MCFM

In this section MCFM (Monte Carlo for FeMtobarn processes at Hadron Colliders) is briefly described, for more information see [42]. MCFM is a fixed order parton level generator, which gives LO, NLO and NNLO predictions for hadronic collisions. In order to fix the input parameters for the electroweak couplings, MCFM allows one to choose between different schemes. For the following analysis the same scheme as in ALPGEN is used (ewscheme=+1), which is also the default scheme of MCFM. Tab. 5.1 shows the parameters for the chosen scheme.

Parameter	Name	Input Value	Output Value
G_F	Gf	1.16639×10^{-5}	input
$\alpha(M_Z)$	aemmz	1/128.89	calculated
$\sin^2\Theta_\omega$	xw	0.2312	calculated
M_W	wmass	80.419 GeV	input
M_Z	zmass	91.188 GeV	input
M_t	mt	172.5 GeV	input

Table 5.1: Parameters for the scheme (ewscheme=+1) used in the following analysis for defining the electroweak couplings [42].

In addition, MCFM allows the choice of the factorization/renormalization scale, which is set to $\mu^2 = M_Z^2 + p_T(Z)^2$. MCFM allows also the choice of PDF sets, that correspond to the process studied and the possibility for LO or NLO calculations. In the following analysis cteq6l

[1] Algorithm which matches the Matrix element calculations and the parton shower to prevent double counting.

or cteq6m are used. However, $\alpha_s(M_Z)$ is hard-wired with the choice of the PDF set. So one cannot tune it, neither it is possible to vary the number of loops used for the running of α_s. For cteq6l and cteq6m $\alpha_s(M_Z)$ is 0.118. MCFM has a lot of available processes. The processes used in the following analysis are shown in Tab. 5.2. An example of an input file to run MCFM is shown in Sect. A.

nproc	$f(p_1) + f(p_2) \to ...$	order
31	$Z^0(\to e^-(p_3) + e^+(p_4))$	NLO
41	$Z^0(\to e^-(p_3) + e^+(p_4)) + f(p_5)$	NLO
44	$Z^0(\to e^-(p_3) + e^+(p_4)) + f(p_5) + f(p_6)$	NLO
45	$Z^0(\to e^-(p_3) + e^+(p_4)) + f(p_5) + f(p_6) + f(p_7)$	LO

Table 5.2: MCFM processes which are used for the following analysis [42]. nproc is the parameter, which has to be set in the input file to choose the process. $f(p_i)$ describes an additional partonic jet.

5.3 Monte Carlo Production at the ATLAS Experiment

The production of MC events at ATLAS is performed in 5 steps from the generation up to the production of Analysis Object Data (AOD). The Athena framework [43] is used for all this steps. Athena jobs are configured to send them via GANGA[2] to the Grid.

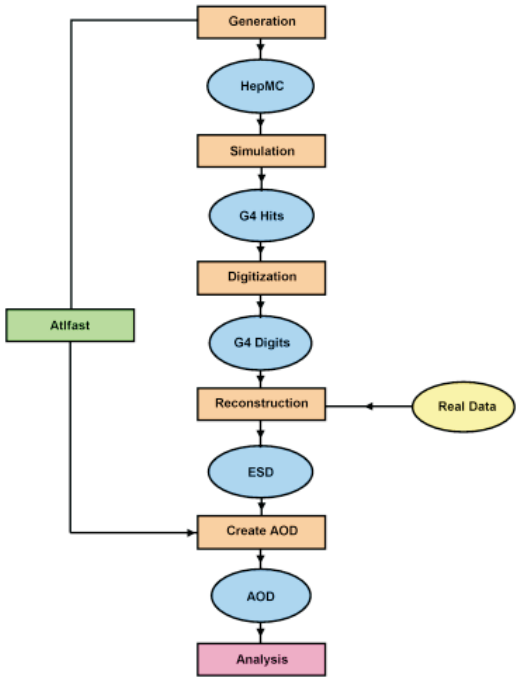

Figure 5.1: Schematic view of the full chain or fast Monte Carlo production for the generation of events in ATLAS [44].

[2]GANGA is a Grid user interface for the ATLAS experiment.

Fig. 5.1 shows a schematic view of the different steps, which have to be done for a full chain Monte Carlo production. There is also the possibility to replace the CPU intensive steps, the simulation, the digitization and the reconstruction by a fast simulation (ATLFAST II). ATLFAST II only needs the output from the generation and creates then directly AODs by a parametrization of the ATLAS detector. So, using ATLFAST II leads to much more available statistics. However, ATLFAST II has the disadvantage that some parts of the detector are not modelled well enough to do precision studies. The following subsections explain the different steps of the full chain Monte Carlo production in more detail.

5.3.1 Event Generation

In the event generation particle four-vectors for the specific physics processes are produced and saved as HepMC. The MC generators, which are used for the following analysis, are explained in the previous two sections, Sect. 5.1 and Sect. 5.2.

5.3.2 Event Simulation

The event simulation is based on previously generated events. Within the simulation process, the generated events are passed through a software called GEANT4 [45]. GEANT4 provides the framework and the functionality for simulating the detector. Solutions for geometry descriptions, material descriptions, physics processes, propagation of particles through the detector and many more are included. The output of the GEANT4 is GEANT4 Hits, which contain for example information about the position and the energy deposition of a particle, as it traversed the detector.

5.3.3 Event Digitization

The event digitization uses the GEANT4 Hits from the event simulation. With the digitization the hits are translated into the output, which is expected as response from the ATLAS detector, GEANT4 Digits. The propagation of charges and light has to be taken into account as well as the design and the performance. The final output format of the event digitization are the Raw Data Objects (RDOs), which simulate the raw data from the detector.

5.3.4 Event Reconstruction

The event reconstruction is the same for both, the digitized MC events and the real data. During the event reconstruction, the raw data with the output of the readout electronics are reconstructed as tracks and energy deposition. The output is saved as Event Summary Data (ESD). The ESDs contain the reconstructed objects and additional information for re-running particle reconstruction procedures (e.g. calorimeter cell energies). For the physics analysis, a less detailed data format is used, the Analysis Object Data (AOD), which contains the reconstructed objects and only minimal additional informations. The analysis in this thesis was performed on AODs.

5.4 Monte Carlo Datasets

In this section the Monte Carlo datasets which are used in this thesis are described; first the samples for the VBF H$\rightarrow \tau^+\tau^-$ analysis and then the samples for the $Z \rightarrow e^+e^-$ analysis.

The Monte Carlo dataset for the signal process VBFH$\rightarrow \tau^+\tau^-$ in which one τ decays hadronically and the other one leptonically is generated with HERWIG 6.510 interfaced with Jimmy 4.1 at a Higgs boson mass of 120 GeV/c^2, using the leading order PDF set CTEQ6L1[3]. The generation is done with a minimum p_T of 5 GeV/c and $|\eta| < 2.7$ for leptons.

The signal process $Z \rightarrow e^+e^-$ is generated with ALPGEN interfaced with HERWIG using again the leading order PDF set CTEQ6L1. Each parton multiplicity up to $n = 5$ is generated separately. All processes except for Z+5 partons are exclusive. The generation is done with a renormalisation and factorization scale of $m_Z^2 + P_T^2(Z)$. In order to prevent double counting as described in Sect. 5.1.3 ALPGEN uses MLM-Matching with a matching cut of $p_T > 20$ GeV/c. For the analysis, the $Z(\rightarrow e^+e^-)$ + n partons (n= $0, 1, .., 5$) samples are merged based on their individual cross sections and their k-factors. For comparison and uncertainty estimation the signal process $Z \rightarrow e^+e^-$ is also generated with PYTHIA 6.417 using again the leading order PDF set CTEQ6L1 and MC@NLO interfaced with HERWIG and Jimmy using the next-to-leading order PDF set CTEQ6M. Both samples are inclusive and include a general event filter cut requiring one lepton with $|\eta| < 2.8$. In addition the di-electron mass is required to be larger than 60 GeV/c^2.

The background processes $Z \rightarrow \tau^+\tau^-$ and $W \rightarrow e\nu$ are generated with ALPGEN with the same configuration and the same generator filter as the ALPGEN $Z \rightarrow e^+e^-$ sample. The top quark pair production is generated with MC@NLO using the next-to-leading order PDF set CTEQ6M. This sample includes only the "no-all-hadronic"part and the leptons have a minimum p_T of 1 GeV. For the QCD multi jet background a filtered QCD sample generated with PYTHIA is used. At least one narrow cluster ($\Delta\eta \times \Delta\phi = 0.06 \times 0.06$) with $|\eta| < 2.7$, $p_T \geq 17$ GeV/c is required at generator level.

Tab. 5.3 summarizes all the signal and background datasets for the VBFH$\rightarrow \tau^+\tau^-$ and the $Z \rightarrow e^+e^-$ analysis.

[3]CTEQ6L1 means leading order fit with a leading order α_s.

sample	process	# events	$\int L\mathrm{d}t$ [pb^{-1}]
ALPGEN + HERWIG			
107650	$Z \to e^+e^- + 0$ partons	269280	299.80
107651	$Z \to e^+e^- + 1$ partons	61767	298.97
107652	$Z \to e^+e^- + 2$ partons	216945	2992.34
107653	$Z \to e^+e^- + 3$ partons	63412	3005.31
107654	$Z \to e^+e^- + 4$ partons	18314	3052.33
107655	$Z \to e^+e^- + 5$ partons	5500	3235.29
107670	$Z \to \tau^+\tau^- + 0$ partons	270649	299.82
107671	$Z \to \tau^+\tau^- + 1$ partons	62678	299.52
107672	$Z \to \tau^+\tau^- + 2$ partons	210234	2996.49
107673	$Z \to \tau^+\tau^- + 3$ partons	89911	4267.25
107674	$Z \to \tau^+\tau^- + 4$ partons	18500	3062.91
107675	$Z \to \tau^+\tau^- + 5$ partons	5479	3204.09
107680	$W \to e\nu + 0$ partons	1191085	116.95
107681	$W \to e\nu + 1$ partons	242424	114.77
107682	$W \to e\nu + 2$ partons	746283	1103.97
107683	$W \to e\nu + 3$ partons	214074	1053.00
107684	$W \to e\nu + 4$ partons	58872	1049.41
107685	$W \to e\nu + 5$ partons	17492	1053.73
HERWIG + JIMMY			
105334	VBF H$\to \tau^+\tau^- \to$lh	49954	593277.91
MCatNLO			
106060	$Z \to e^+e^-$	2493410	1895.79
105200	ttbar (no all hadronic)	1424370	6931.92
PYTHIA			
106050	$Z \to e^+e^-$	4906267	4467.55
105802	Dijets (JF17)	7241000	0.07

Table 5.3: MC samples for VBFH$\to \tau^+\tau^-$ and the $Z \to e^+e^-$ analysis. In addition, the effective number of events and the integrated luminosity for each sample are shown.

For all datasets explained in Tab. 5.3 the fully simulated merged samples with the latest reconstruction tag are used. All of them are produced at a centre of mass energy of 10 TeV with ATHENA version 14. The PDF sets are taken from an external PDF library, LHAPDF [46] and the input parameters for the masses and widths resemble the values listed in the PDG of 2007, see Tab. 5.4.

particle	mass [GeV]	width [GeV]
top	172.5	
W-boson	80.403	2.141
Z-boson	91.1876	2.4952

Table 5.4: Masses and width for the top quark, W boson and Z boson [1].

6 Particle Reconstruction and Identification

For the selection in this thesis, the standard lepton and jet identification, which were recommended by the Higgs group [47], are used. In this chapter these algorithms are described in detail.

6.1 Jet Reconstruction and Identification

For the jet reconstruction, two different representations for signals from jets in the calorimeter are available: calorimeter tower signals and topological cell clusters. Fig. 6.1 shows the schematic view of the reconstruction sequences for both representations.

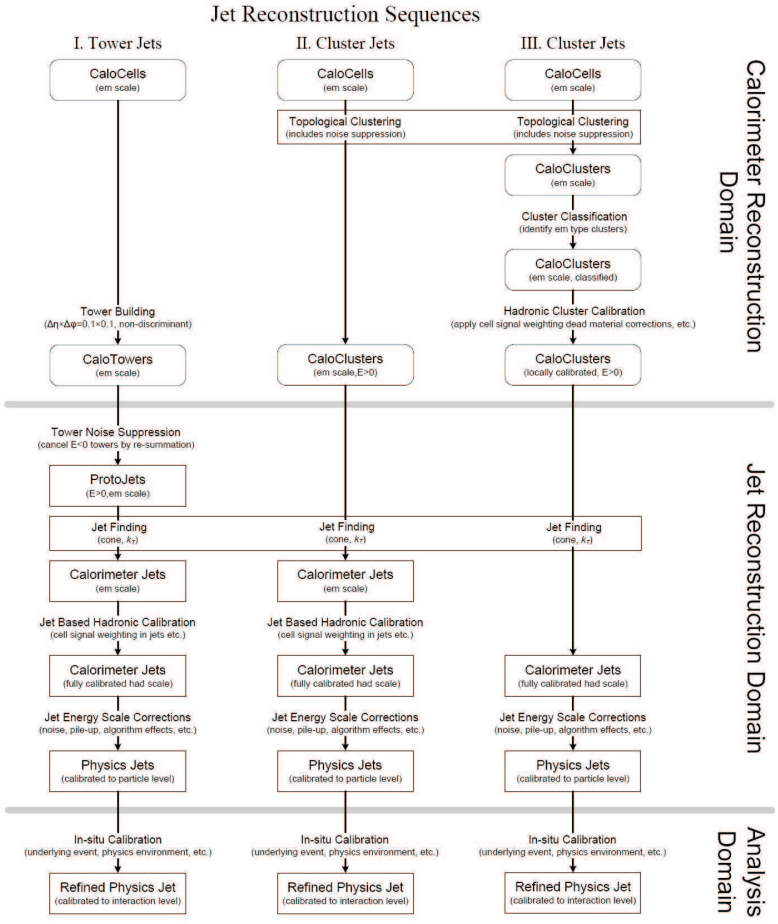

Figure 6.1: Schematic view of the reconstruction sequences for calorimeter tower signals (left) and for topological cell clusters uncalibrated (centre) and calibrated (right) in ATLAS [48].

For the following analysis topological cell clusters are used. Topological cell clusters are basically three dimensional "energy blobs", which describe the showers developing for each particle entering the calorimeter. The cluster formation follows a 4-2-0 algorithm. That means, using first the cells which have an energy above four times the electronic plus pile-up noise of the cells as a seed, then aggregate recursively all neighbours which are above two times the noise. Finally, all remaining cells with $|E| > 0$ are added to the clusters.

For the jet identification jet finders are used. In ATLAS two different jet finders are currently used, the iterative seeded fixed-cone jet finder with split and merge and the k_T algorithm [49]. Other jet finders will be available in the future, e.g. anti-k_T. For the following analysis the seeded fixed-cone jet finder is used. It uses the hardest object as a seed, if the p_T is above a certain threshold (currently $p_T = 1$ GeV/c in ATLAS), and all other objects within a cone of $\Delta R < R_{cone}$ are combined with the seed. From that a new seed direction is calculated by summing up the four momenta of all the objects. Afterwards, a new cone is drawn around it. The previous steps are done in an iterative procedure until the direction of the seed is stable. In addition, a split and merge step after the jet finding is used. In order to calibrate the jets the $H1$-style calibration is used [50].

In the following analysis cone 0.4 topo jets are used and required to have a transverse momentum greater than 20 GeV/c and $|\eta| < 4.8$.

6.2 Tau Reconstruction and Identification

The tau reconstruction and identification is a very difficult task. Taus are heavier than the other leptons and short lived. Therefore, taus are decaying inside the detector. They can decay leptonically or hadronically. At LHC processes with taus in the final state, which have a high production cross section, are available, such as $W \to \tau\nu$ or $Z \to \tau^+\tau^-$. The precision of the measurement of properties of such processes depends strongly on the tau reconstruction and identification efficiency. Hadronically decaying taus are easier to reconstruct than leptonically decaying taus, due to the difficulties in distinguishing between leptonic modes and primary muons or electrons. Hadronic decays happen via a W boson and provide a clean signal with a few tracks and are highly boosted. In contrast, QCD jets are produced by strong interactions and lead to busy events with a high track multiplicity. Therefore hadronically decaying taus can be identified by their key quantities: They are well collimated and have a low track multiplicity.

For the tau reconstruction two different algorithms are available in ATLAS, the calorimeter seeded algorithm and the track seeded algorithm.

- The track seeded algorithm uses a high p_T track with a minimum p_T of 6 GeV/c as a seed. All tracks with $p_T > 1$ GeV/c are collected within a cone of $\Delta R = 0.2$ around the seed.

- The calorimeter seeded algorithm searches for a cone 0.4 Topo jet in the calorimeter with an energy above 10 GeV and use it as a seed. The energy is calibrated using H1 calibration. Finally the jet is matched to tracks with a minimum p_T of 1 GeV/c, in a cone of $\Delta R = 0.3$. η and ϕ are determined by the calorimeter information.

Currently in ATLAS a combination of track and calorimeter seeded algorithm is used, where for each track-seeded tau the algorithm looks for a calorimeter cone 0.4 Topo jet in a cone of $\Delta R = 0.2$. For the tau identification three different methods can be used; a cut based, a compensated neural network or a likelihood method. For the first data the cut based method seems to be the best.

In the following analysis taus are required to fulfil the medium cut based identification and pass the electron and muon veto, for a detailed description see [51]. In addition the taus are required to have one or three tracks and a charge of ± 1. Finally the transverse momentum is required to be larger than 20 GeV/c and the taus must have a $|\eta| < 2.7$.

6.3 Electron Reconstruction and Identification

For the electron reconstruction the standard calorimeter-seeded algorithm [48] is used and for electrons, which are not covered by the inner detector, the "forward"electron reconstruction algorithm [48] is used.

The standard calorimeter-seeded algorithm starts with cluster information reconstructed in the electromagnetic calorimeter. In order to find and reconstruct the electromagnetic clusters the "sliding window"algorithm [52] is used. The size of this window is fixed for a specific particle type and detector region. Comparing electrons and photons, the size of the window for the electrons has to be much larger, because of the higher interaction probability with the material and their bending in the magnetic field. The window is positioned in this way that the covered cluster maximises the amount of energy. For each reconstructed cluster, the algorithm searches for a matched track within a $\Delta\eta \times \Delta\phi$ window of 0.05×0.10 and a momentum p, for which the ratio between the clustered energy and the momentum is smaller than 10. An additional algorithm rejects electrons from photon conversions. The energy of the electrons is obtained from the calorimeter and ϕ, η are obtained from the tracker. Both have to be calibrated. For data the final calibration will be done with $Z \rightarrow e^+e^-$ events.

In contrast to the standard calorimeter-seeded algorithm, the forward electron reconstruction algorithm can only use calorimeter information, because the inner detector covers only a region up to $|\eta| < 2.5$.

For electron identification, three different methods are available for physics analysis; the loose, medium and tight selection. In the following the medium selection is used, which uses calorimeter information and tracking information. For the calorimeter, cuts are applied for the hadronic leakage, on shower shape variables for the middle layers of the electromagnetic calorimeter and on the strips in the first layer of the electromagnetic calorimeter. The strip-based cuts are effective for the rejection of $\pi^0 \rightarrow \gamma\gamma$. For the tracks some basic cuts on the track quality are applied. Using the Medium selection increases the jet rejection efficiency by a factor of $3 - 4$ while reducing the ID efficiency by 10%.

In the following analysis, electrons are required to fulfil the non-isolated medium selection. In addition, isolation is applied using calorimeter cone isolation. The energy deposition in a hollow cone of 0.2 around the electron has to be smaller than 10% of its transverse momentum. For this procedure the energy deposition in the calorimeter in a cone of 0.05 surrounding the electron track is subtracted from the energy deposition in the cone of 0.2 around the electron. The transverse momentum itself is required to be greater than 15 GeV/c and the electrons must have $|\eta| < 2.7$.

6.4 Muon Reconstruction and Identification

For the muon reconstruction the STACO algorithm [48] is used, which is the current ATLAS default for physics analysis. First of all standalone muons are reconstructed in the muon spectrometer by finding tracks and extrapolating them to the beam line. Within the STACO algo-

rithm this is combined with measurements of tracks from the inner detector by matching the two measurements (see Fig.6.2).

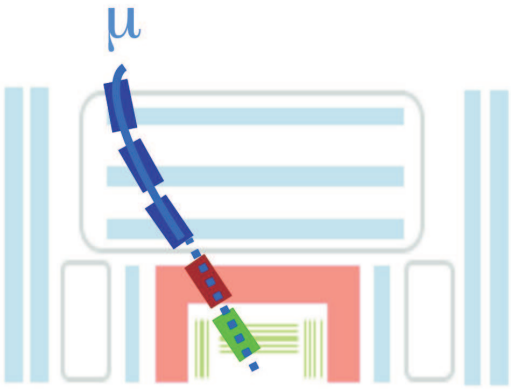

Figure 6.2: Sketch of the combined muon reconstruction [44].

For this matching, a χ^2 is defined by the following relation

$$\chi^2_{match} = (T_{MS} - T_{ID})^T (C_{ID} + C_{MS})^{-1} (T_{MS} - T_{ID}). \tag{6.1}$$

It provides the quality of this matching procedure and can be used to decide which combination has to be rejected.

The momentum of the muon is measured in the muon spectrometer and is corrected for energy loss in the calorimeter. The use of combined muons gives the best resolution for low and high momentum.

Muons are required to have a $p_T > 10$ GeV/c and $|\eta| < 2.7$, which is the region which is covered by the muon spectrometers. In addition calorimeter isolation for the muons is applied. The energy deposition in the calorimeter within a hollow cone of 0.2 around the muon divided by the p_T of the muon has to be smaller than 0.1. For this procedure the energy deposition in the calorimeter in a cone of 0.05 surrounding the muon track is subtracted from the energy deposition in the cone of 0.2 around the muon. To ensure a good quality of the muon, a cut on the matching χ^2 ($\chi^2_{match} < 100$) and a cut on the χ^2 of the fit ($\chi^2_{match} < 500$) are also applied.

6.5 Overlap Removal

In order to prevent that one detector signature is interpreted as two physics objects, an overlap removal is applied. Especially, for $Z(\rightarrow e^+e^-) + \ jets$ events it is crucial to have an overlap removal between electron and jets. Each electron candidate is as well reconstructed as a jet.

In this thesis, an overlap removal in the order of muon → electron → tau → jet in a cone of 0.2 is applied on the particles, which fulfil the requirements for the lepton and jet identification explained above.

7 Search for Higgs Boson Production via Vector Boson Fusion in Tau Final States

In this chapter the VBF production of the Higgs boson via semileptonic tau channel is presented. First a short introduction into the process with its key quantities is given. Afterwards, the event selection and the predictions for the first data are shown.

7.1 Process

As mentioned in Sect. 4.2, the Higgs boson production via VBF in $H \rightarrow \tau^+\tau^-$ decay mode is one of the most promising channels for low Higgs boson masses. In addition, it provides a reasonably large signal to background ratio.

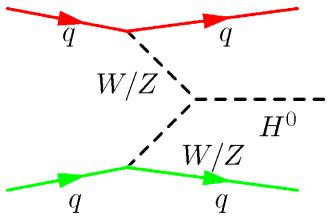

Figure 7.1: Feynman diagram for the Higgs boson production via Vector Boson fusion. The red and green line indicate the colour flow between the jets.

Fig. 7.1 shows the Feynman diagram of the VBF production of the SM Higgs boson. For the following study the Higgs boson decay to two taus is considered. Afterwards, the two taus undergo a further decay. Either both taus decay to two light leptons (dileptonic channel), or one tau decays to a light lepton and the other decays hadronically (semileptonic channel), or, finally, both taus decay to light-quark jets (all hadronic channel). The corresponding branching ratios (BR) are shown in Tab. 7.1.

decay mode	BR
dileptonic	13%
semileptonic	46%
all hadronic	41%

Table 7.1: Branching ratios for the different decay modes in the di-tau decay

In this analysis, the semileptonic channel is studied. Because, although the all hadronic channel has large BR, the jet-ID is difficult with first data, and the dileptonic, although its a very clean channel has low BR. Hence, the detector signature of the event in this channel consists of a lepton (e/μ), a jet coming from one tau and two very forward jets coming from

the VBF. The two forward jets are expected to have a high transverse momentum and are well separated in pseudorapidity.

Other SM decays can result in similar final states. The main backgrounds are $Z + jets$ (EW and QCD), $W + jets$ (EW and QCD) ttbar and QCD jets [48].

Due to the colour coherence of the jets in the final state, indicated by the red and green line in Fig. 7.1, QCD radiation between them is suppressed in contrary to most of the background processes, like e.g. QCD $Z + jets$, ttbar or QCD jets. They have a much larger probability for QCD radiation. The only exception is the electroweak $Z + jets$ background, see Fig. 7.2, which has a very low cross section.

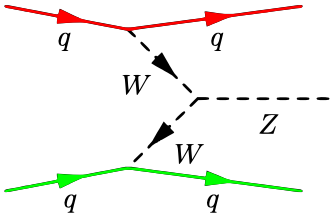

Figure 7.2: Feynman diagram for the electroweak $Z + jets$ production. The red and green line indicate again the colour flow between the jets.

Hence, a central jet veto is a good way to separate between signal and background. This is shown and motivated in Fig. 7.3.

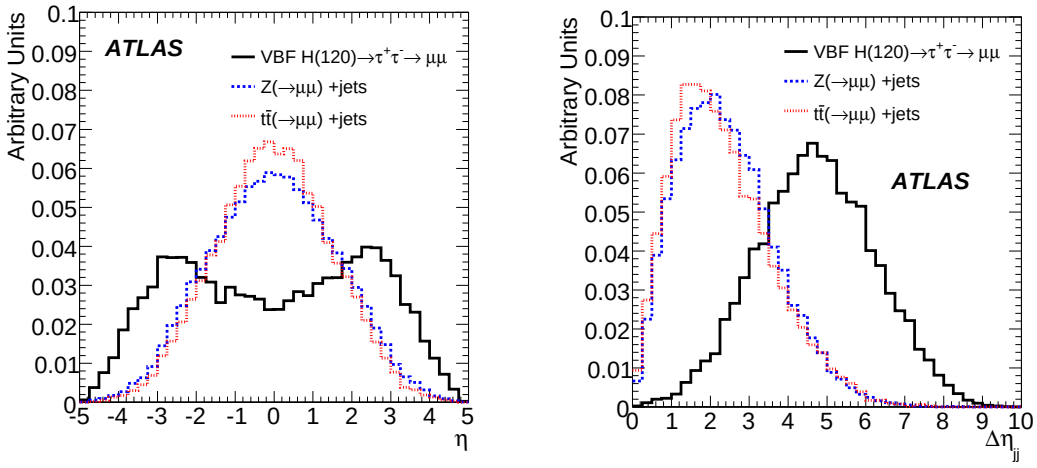

(a) (b)

Figure 7.3: Pseudorapidity of the leading jet (a) and pseudorapidity gap between the tagging jets (b) for signal events and the relevant background [48].

Another very important property is the missing transverse energy because of the neutrinos from tau decays.

In the following section, the pseudorapidity gap between the tagging jets and the presence of a third jet in the central region of the detector, called VBF Higgs boson key quantities, are studied in detail.

7.2 Event Selection

The event selection starts by applying the object selection, described in Chapter 6, on the reconstructed particles. Afterwards, the cutflow, shown in Tab. 7.2, is applied on each event. This cutflow is recommended by the ATLAS Higgs Working Group and optimized to get a high acceptance of the Higgs boson signal events at a centre of mass energy of 14 TeV. For a detailed description of the different cuts see [48].

Trigger	loose single electron trigger with $p_T > 20$ GeV/c or the single muon trigger with $p_T > 20$ GeV/c
Trigger Lepton	trigger electron $p_T > 25$ GeV/c and trigger muon $p_T > 20$ GeV/c
Dilepton Veto	number of electrons+muons < 2
Tight Tau requirement	number of tau $= 1$ and opposite charge with trigger lepton
Missing p_T requirement	$\not{E}_T > 30$ GeV
Transverse Mass requirement	$M_T(\text{lepton}, \not{E}_T) < 30$ GeV/c^2
Collinear Approximation	$0 < x_l < 0.75$, $0 < x_h < 1$, $\lvert\cos(\Delta\phi)\rvert < 0.9$
Tight Jet requirement	Number of jets ≥ 2, leading jet $p_T > 40$ GeV/c
Forward Jet requirement	leading and 2nd leading jet in opposite hemispheres $\eta_{j_1} \cdot \eta_{j_2} < 0$
Centrality requirement	$\min(\eta_{j_1}, \eta_{j_2}) < \eta_\tau, \eta_{lepton} < \max(\eta_{j_1}, \eta_{j_2})$
Jet Separation	$\Delta\eta_{j_1 j_2} > 4.4$
Di-jet mass	$M_{j_1 j_2} > 700$ GeV/c^2
Central Jet Veto	veto if $\lvert\eta_{\text{other jet}}\rvert < 3.2$
Mass window	$m_H - 15$ GeV/c^2 $< m_{\tau\tau} < m_H + 15$ GeV/c^2

Table 7.2: Event selection cuts for the VBF production of the Higgs boson in the semileptonic tau channel [44].

7.3 Expected Signal for 10 TeV

This section shows the cutflow for VBF H$\rightarrow \tau^+\tau^- \rightarrow lh$ process at a centre of mass energy of 10 TeV. Tab. 7.3 summarizes the expected events after each cut for the current available Monte Carlo statistics. The effective cross section for this sample is 84.2 fb. Therefore, the number of events corresponds to a luminosity of 593.3 fb^{-1}.

Process	**VBFH**$\rightarrow \tau^+\tau^- \rightarrow lh$			
	with trigger		**w/o trigger**	
	events	**cut efficiency**	**events**	**cut efficiency**
Start	49954		49954	
Trigger	24524	0.49 ± 0.01	-	-
Trigger Lepton	18496	0.75 ± 0.01	21036	0.42 ± 0.01
Dilepton Veto	16497	0.89 ± 0.01	18871	0.90 ± 0.01
Tight Tau requirement	3174	0.19 ± 0.01	3644	0.19 ± 0.01
Missing p_T requirement	1918	0.60 ± 0.01	2189	0.60 ± 0.02
Transverse Mass requirement	1430	0.75 ± 0.01	1629	0.74 ± 0.02
Collinear Approximation	883	0.62 ± 0.02	1006	0.62 ± 0.02
Tight Jet requirement	744	0.84 ± 0.02	843	0.84 ± 0.04
Forward Jet requirement	627	0.84 ± 0.02	706	0.84 ± 0.04
Centrality requirement	578	0.92 ± 0.02	648	0.92 ± 0.05
Jet Separation	303	0.52 ± 0.03	342	0.53 ± 0.04
Di-jet mass	239	0.79 ± 0.03	270	0.79 ± 0.06
Central Jet Veto	213	0.89 ± 0.03	238	0.88 ± 0.08
Mass window	190	0.89 ± 0.03	212	0.89 ± 0.08

Table 7.3: Signal events for VBF H$\rightarrow \tau^+\tau^- \rightarrow lh$ for the current available statistics after each cut.

From that the trigger efficiency can be calculated to 89.6% after the mass window. Therefore, for the first 100 pb^{-1} of data 0.036 VBF H$\rightarrow \tau^+\tau^- \rightarrow lh$ events are expected.

Fig. 7.4 shows the distributions for the VBF Higgs boson key quantities for signal events at a centre of mass energy of 10 TeV estimated from the Monte Carlo events. For the estimation of the distribution from the relevant background processes, Monte Carlo samples with a preselection are needed to have enough statistics.

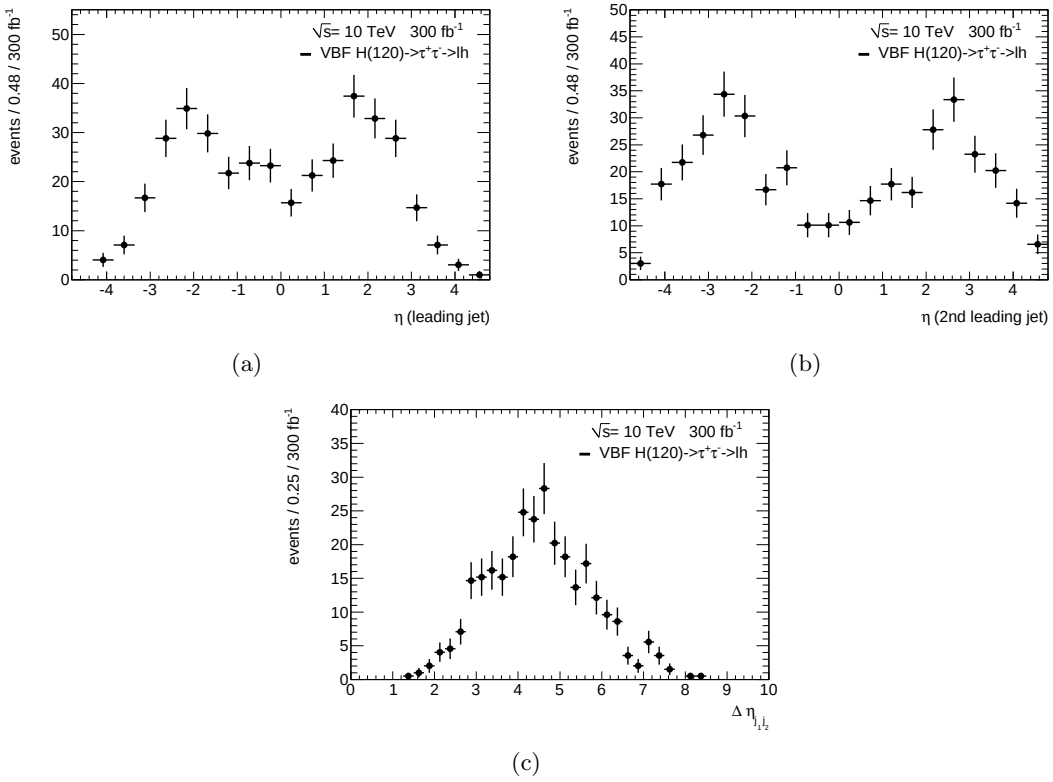

(a) (b)

(c)

Figure 7.4: Distributions of the pseudorapidity of the leading jet (a) and the second leading jet (b) and the pseudorapidity gap between the tagging jets (c). The plots show the expectation for a luminosity of 300 fb^{-1}.

The expected distributions for 10 TeV look similar to the expected distributions for 14 TeV, but the separation between the tagging jets is a bit smaller. Due to the small number of expected signal events for the first 100 pb^{-1} of data, analyse the signal process makes no sense for the first data. It is better to concentrate on background processes and try to validate the generators in a Higgs boson signal free region with respect to the VBF Higgs boson key quantities.

Part II

Measurement of the $Z(\rightarrow e^+e^-) + \ jets$ Cross Section at the LHC

8 Motivation

The aim of the following analysis is to compare theoretical predictions for the inclusive and differential $Z(\rightarrow e^+e^-) + \ jets$ cross section with measurements from the detector and to determine the corresponding statistical and systematic limitations. The comparison is done on hadron level, as shown in Fig. 8.1, to be independent from the detector setup, by determining the ratios between the cross section of the data over the cross section of the theory. Thus, uncertainties have to be determined in three different levels; the detector level, the hadron level and the parton level. In addition, the comparison of different methods for the correction of detector effects and the possibility to validate generators with respect to the VBF H$\rightarrow \tau^+\tau^-$ key quantities is studied.

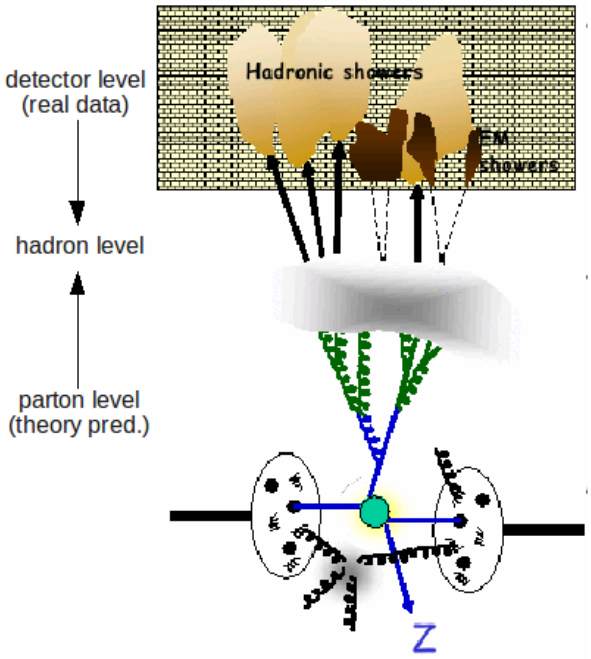

Figure 8.1: Schematic view of jet production and reconstruction. The different levels are shown; parton level, hadron level and detector level.

The full analysis is split into two main parts, which are described in the following two chapters. The first chapter describes the theory part of the analysis including theoretical uncertainties and corrections from parton level to hadron level. The second chapter describes the $Z(\rightarrow e^+e^-) + \ jets$ cross section measurement in data and the correction to hadron level, including the event selection, background predictions, the methods for the correction of detector effects and the statistical and systematic uncertainties.

Finally, the results are summarized and the direct comparison between parton level predictions and detector measurements is made on hadron level including the uncertainties.

8.1 Comparison between Monte Carlo Generators and MCFM on Hadron Level

The section describes a prestudy for the following analysis. Several MC generators are available in the ATLAS framework for the process $Z(\rightarrow e^+e^-) + \ jets$ (see Sect. 5.1).

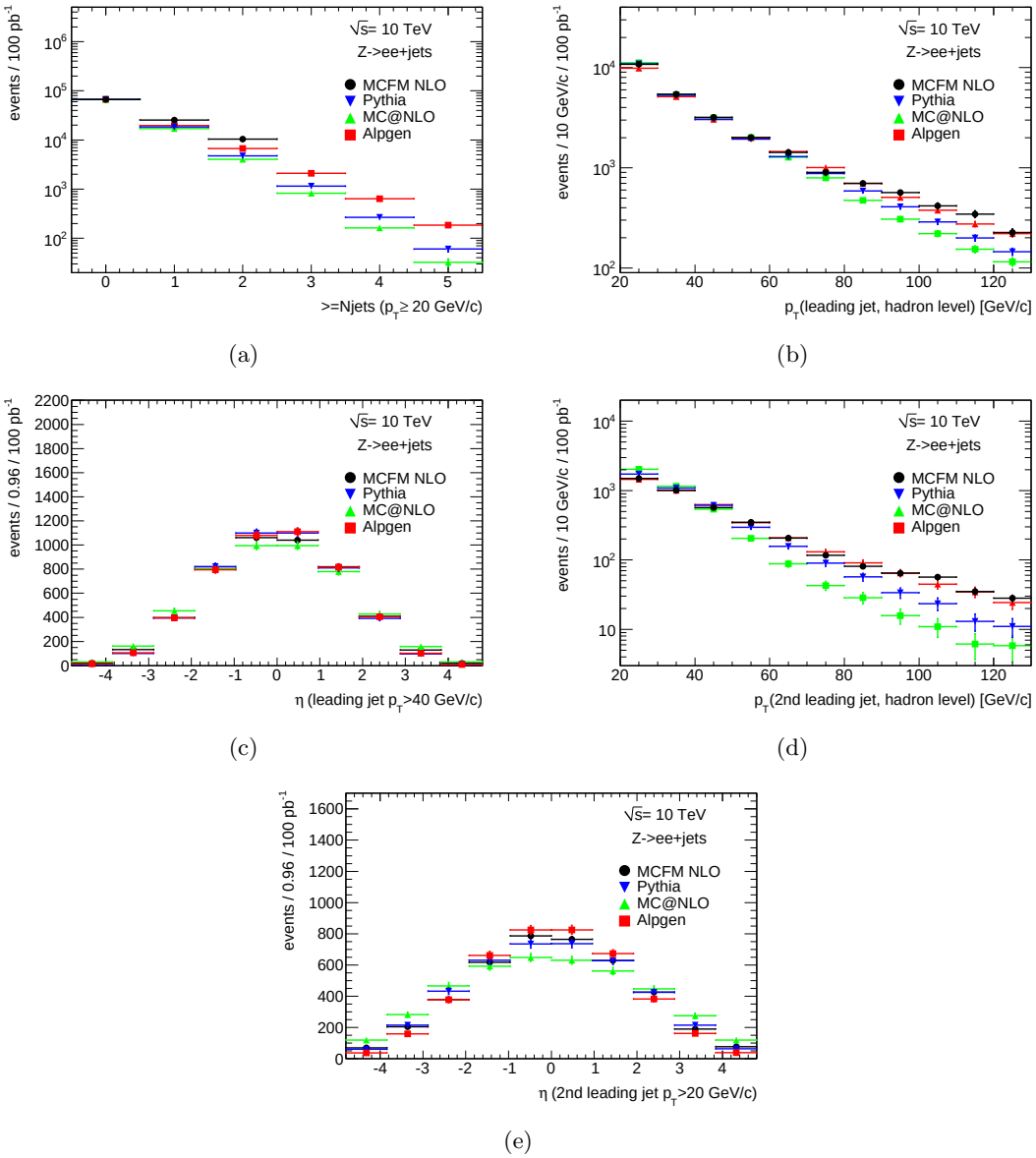

Figure 8.2: Comparison between perturbative QCD calculations made by MCFM and the different MC generators for the inclusive $Z(\rightarrow e^+e^-) + \ jets$ cross section (a), p_T (b) and η (c) of the leading jet and p_T (d) and η (e) of the second leading jet.

Fig. 8.2 shows the comparison of the inclusive and differential $Z(\rightarrow e^+e^-) + \ jets$ cross

sections at hadron level predicted by different MC generators with the theoretical predictions from MCFM corrected for UE and fragmentation, which are described in detail in Sect. 9.1. The inclusive $Z(\rightarrow e^+e^-) + \ jets$ cross section is normalized to the inclusive $Z(\rightarrow e^+e^-)$ cross section, predicted by NLO calculations from MCFM. The differential $Z(\rightarrow e^+e^-) + \ jets$ cross sections are normalized to the total number of jets with $p_T > 20$ GeV.

From Fig. 8.2(b) and Fig. 8.2(d) follows that ALPGEN (red) gives a good agreement with MCFM and predicts a harder p_T spectrum compared to the other two generators. PYTHIA (blue) has a very soft p_T spectrum. Only for the first jet PYTHIA is comparable with ALPGEN, because of a special tuning for the first jet. Looking at MC@NLO (green), the prediction for the pseudorapidity differs a lot from the predictions of the other generators. The shape is much broader and deviates more for jets of a higher order (see Fig. 8.2(c) and Fig. 8.2(e)). The origin of this effect is not justified yet. It is independent from p_T and does not arise from the difference between LO and NLO MC generators because in that case the effect would also be visible in MCFM. Fig. 8.3 shows the comparison of the different generators for the VBF $H \rightarrow \tau^+\tau^-$ key quantities. The first plot shows the distribution for the pseudorapidity gap between the tagging jets, the second shows the transverse momentum of the third jet and the last shows the centrality of the third jet.

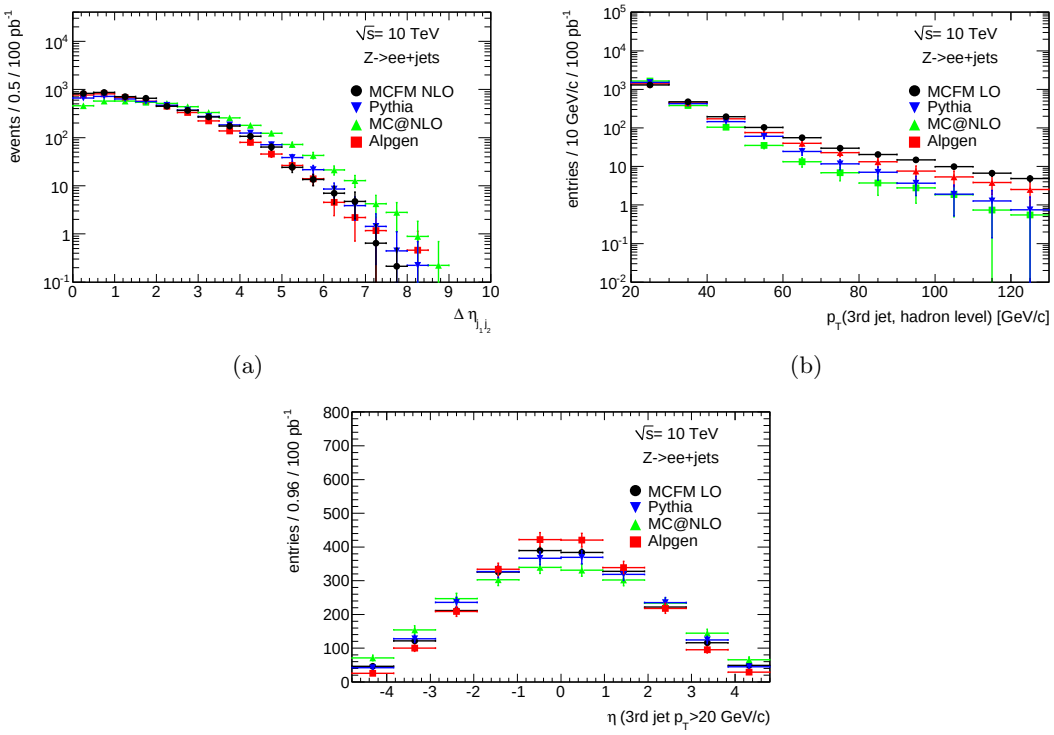

Figure 8.3: Comparison between perturbative QCD calculations done by MCFM and the different MC generators for the VBF $H \rightarrow \tau^+\tau^-$ key quantities: pseudorapidity gap (a), p_T of the third jet (b) and the centrality of the third jet (c).

Generators used in ATLAS differ a lot in the predictions of the VBF $H \rightarrow \tau^+\tau^-$ key quantities. As well as for the pseudorapidity distributions, MC@NLO differs from the other generators for

the pseudorapidity gap. MC@NLO predicts jets which are much more separated in η which is due to the broader η distributions of the leading and second leading jet.

9 From Parton Level to Hadron Level

This chapter describes how the theory predictions for the $Z(\rightarrow e^+e^-) + \ jets$ cross section are derived and corrected to the hadron level. The prediction for the theory is calculated with perturbative QCD in LO and NLO via MCFM. On parton level uncertainties of the PDFs have an impact on the theoretical cross section. In addition theoretical calculations depend on the choice of the renormalisation and factorization scale. For the extraction from parton level to hadron level the theory prediction has to be corrected for non-pertubative effects, i.e. underlying event and fragmentation.

9.1 Corrections for Non-perturbative Effects

The corrections for non-pertubative effects are determined using MC generators. In this study this is done by event generation with PYTHIA 6.4 using the current ATLAS tune for MC08 [53]. Three different samples are generated, one with the standard tune, one without fragmentation (MSTJ(1)=0) and the last one without fragmentation and underlying event (MSTP(81)=0). In the case where the fragmentation is switched off, PYTHIA generates bare quarks and gluons on which the jet algorithm is running during the reconstruction. The correction has to be done for each observable separately due to the fact that the correction for non-perturbative effects is a simple bin-by-bin correction. As a result, the non-perturbative corrections are highly shape dependent. Fig. 9.1 - 9.4 show the ratio between the number of events with $\geq N \ jets$ with the standard tune and the number of modified jets. The derived corrections can be applied on MCFM in order to develop and refine the method, but they have to be re-calculated with the underlying event measurement from ATLAS, using di-jet events [54].

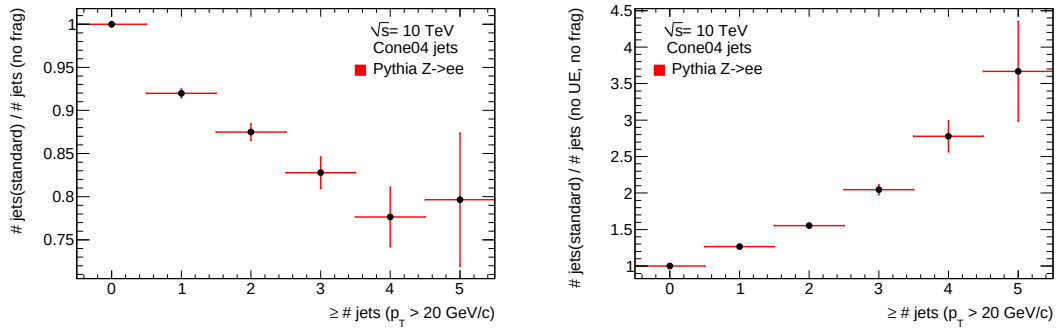

(a) (b)

Figure 9.1: Ratio of Cone04 inclusive jet multiplicity distributions between standard PYTHIA and PYTHIA without fragmentation (a) and between standard PYTHIA and PYTHIA without fragmentation and underlying event (b).

Fig. 9.1 shows the correction from parton to hadron level on the inclusive cross section from fragmentation (a) and from fragmentation and UE (b). As expected, due to the fact that the

out-of-cone energy loss without fragmentation is smaller, the number of low p_T jets is higher without fragmentation. UE produces additional jets at low $p_T \approx 1$ GeV/c, therefore additional energy deposition is available for the jets of the hard interactions. Looking at both effects together, the correction is highly dominated by UE.

Due to lack of statistics for the second and third leading jet and the fact that PYTHIA does not model them adequately, the correction for the transverse momentum spectrum of the jets is derived for all jets together. The bias from calculating the transverse momentum globally compared to the bias from using the PYTHIA shape and doing a different correction for each jet is smaller. Therefore, it could be better to use ALPGEN for the calculation of the correction. Fig. 9.2 shows the global corrections for the transverse momentum distribution of the jets.

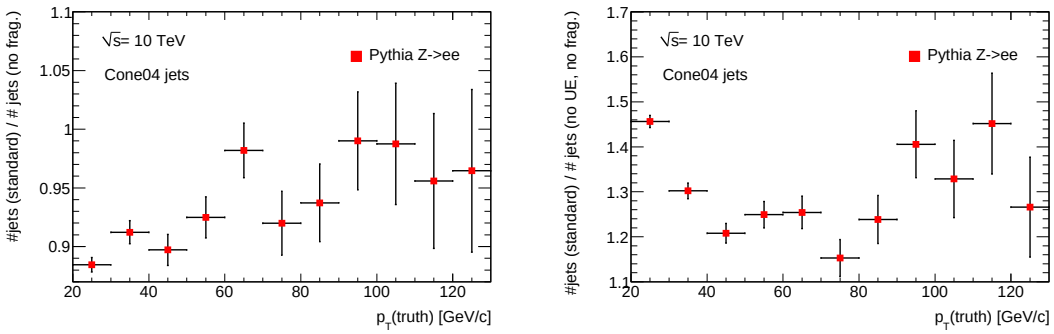

(a) (b)

Figure 9.2: Ratio of Cone04 jet p_T distributions between standard PYTHIA and PYTHIA without fragmentation (a) and between standard PYTHIA and PYTHIA without fragmentation and underlying event (b).

As expected, the effect of UE dominates the effect of fragmentation.

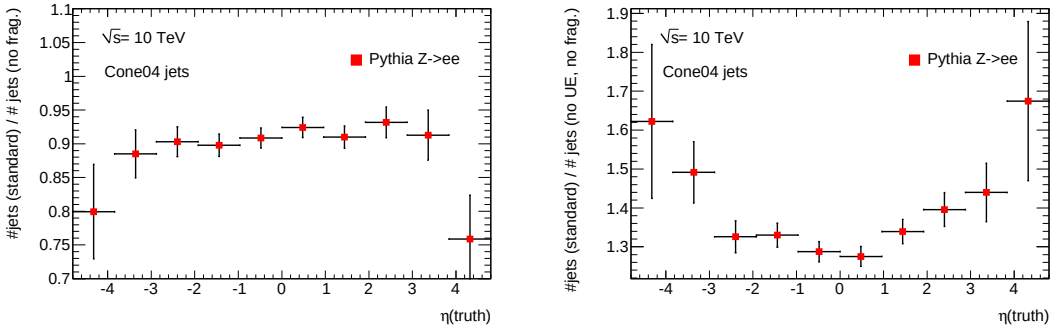

(a) (b)

Figure 9.3: Ratio of Cone04 jet η distributions between standard PYTHIA and PYTHIA without fragmentation (a) and between standard PYTHIA and PYTHIA without fragmentation and underlying event (b).

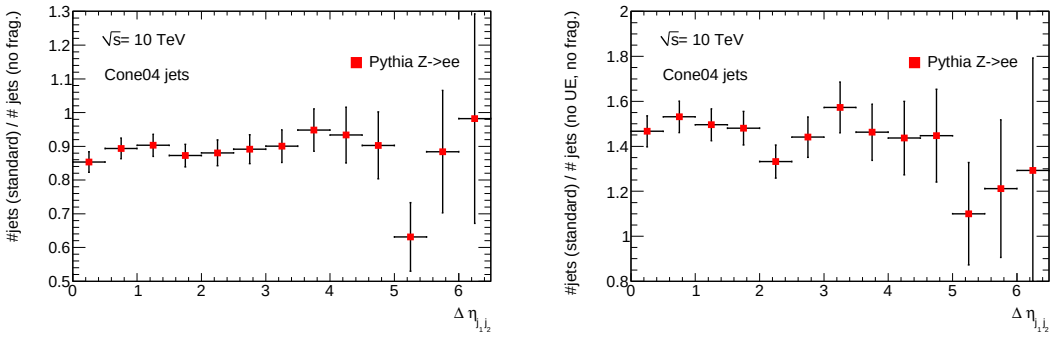

(a) (b)

Figure 9.4: Ratio of Cone04 jet distributions for the pseudorapidity gap between the two leading jets between standard PYTHIA and PYTHIA without fragmentation (a) and between standard PYTHIA and PYTHIA without fragmentation and underlying event (b).

Fig. 9.3 shows the global correction for η of the jets and Fig. 9.4 shows the correction for the pseudorapidity gap between the two leading jets. Due to the fact that jets with a high η have smaller p_T compared to jets with a small η, the correction for UE and fragmentation increases in the forward range.

Due to the migration effect in p_T from the UE, a correct simulation of the p_T shape is very important for the bin-by-bin correction for non-pertubative effects. In addition, due to the fact that generators currently used in ATLAS have different UE predictions and later the UE measurement from data is taken, it is necessary to compare this results with other UE predictions [55, 56]. The corrections derived above are only valid for Cone04 jets. Using a different cone or jet algorithm the correction has to be re-done.

In the following, the MCFM predictions are corrected with the bin-by-bin corrections derived in this section in order to compare them with hadron level predictions of several generators.

9.2 Uncertainties

This section describes the sources of uncertainties, which have to be included for the total uncertainty on the theory. On the parton level uncertainties coming from statistics and the PDF estimation has to be taken into account. In addition, uncertainties from the choice of the factorization and renormalization scale have to be included. For the change from parton level to hadron level an uncertainty on the correction for UE and fragmentation has to be taken into account.

9.2.1 Statistical Uncertainties

The theory predictions in this analysis are made using MCFM. Due to the generated statistics from MCFM, an uncertainty has to be included. With the recent statistics, the uncertainty on the inclusive cross section of $Z(\rightarrow e^+e^-)+1-3\ jets$ is smaller than 0.5% and for the differential cross section depending on p_T of the leading jet the uncertainty is between 0.4% and 2.4% increasing with p_T.

9.2.2 Systematic Uncertainties

This subsection describes the systematic uncertainties on the theory predictions. First the uncertainties coming from the estimation of PDFs are explained. As a second step, the influence of the choice of the renormalisation/factorization scale is discussed and finally the uncertainties coming from the correction for non-pertubative effects are presented.

Uncertainties from PDF's

This study is done with PDF sets provided by the CTEQ group, CTEQ6m and CTEQ6l. Therefore, as described in Sect. 2.4.1, the uncertainty determination is done with 41 different PDF sets, consisting of the PDF set S_0 representing the best fit and the PDF sets for the eigenvector basis S_i^+ and S_i^- differentiate in plus and minus direction. For the calculation of the uncertainties two possibilities are available; symmetric uncertainties (see Eq. 9.1) or asymmetric uncertainties (see Eq. 9.2).

$$(\Delta X) = \frac{1}{2}(\sum_{i}^{N_p}[X(S_i^+) - X(S_i^-)]^2)^{1/2}. \tag{9.1}$$

$$\begin{aligned}(\Delta X)_+ &= (\sum_{i}^{N_p} \max\left\{X(S_i^+) - X(S_0), X(S_i^-) - X(S_0), 0\right\}^2)^{1/2} \\ (\Delta X)_- &= (\sum_{i}^{N_p} \max\left\{X(S_0) - X(S_i^+), X(S_0) - X(S_i^-), 0\right\}^2)^{1/2}\end{aligned} \tag{9.2}$$

In this thesis, asymmetric errors have been calculated, because they describe the uncertainties of PDFs in a more realistic way. For the inclusive cross section the uncertainty for $Z(\rightarrow e^+e-)+ \geq 1\ jet$ is $(+4.41/-3.35)\%$ and for $Z(\rightarrow e^+e-)+ \geq 3\ jets$ $(+1.90/-1.83)\%$. For the differential cross section depending on p_T of the leading jet the uncertainty is $(+5.05/-3.99)\%$ for 20 GeV/c $\leq p_T <$ 30 GeV/c decreasing to higher transverse momentum. For example, for 120 GeV/c $\leq p_T <$ 130 GeV/c the uncertainty is $(+2.41/-1.80)\%$.

Uncertainties from the Choice of the Renormalisation and Factorization Scale

As described in Sect. 2.4.2, the calculation of the cross section of a hard-scattering process depends on the explicit choice of the renormalisation/factorization scale, if it is not a complete perturbation expansion. Therefore, an additional uncertainty on the theory predictions has to be included.

In order to get a first estimate of this scale dependence, the input parameter for the renormalisation/factorization scale in MCFM was changed from $\mu^2 = M_Z^2 + p_T(Z)^2$ to $\mu^2 =< p_T^{jet} >^2$ for the calculation of the inclusive cross section for $Z(\rightarrow e^+e-)+ \geq 1\ jet$. The variation of the renormalisation/factorization scale results in a 6% variation of the inclusive cross section. For a complete description of this uncertainty, the calculation has to be done for more values of the renormalisation/factorization scale. In addition, one should check the predictions with different PDF sets, like MRST PDFs.

Uncertainties from Underlying Event and Fragmentation Corrections

For the correction from parton to hadron level an additional uncertainty on the corrections for non-perturbative effects has to be taken into account. This uncertainty is due to the statistical

fluctuations in the MC sample used for the UE and fragmentation corrections.

The correction results in an uncertainty on the inclusive cross section for $Z(\rightarrow e^+e^-)+ \geq 1-3$ *jets* smaller than 1.5% and on the differential cross section depending on the p_T of the leading jet between 1% and 9%. For the analysis on real data, there will be an additional uncertainty coming from the precision of the UE measurement in data, which will be used to tune Pythia and has not been taken into account yet.

9.2.3 Total uncertainty

This section summarizes briefly all contributions to the uncertainty on the theoretical predictions. Fig. 9.5 shows the different contributions to the total uncertainty on the theory prediction for the inclusive $Z(\rightarrow e^+e^-) + jets$ cross section (a), the differential cross section depending on the p_T of the leading jet (b) and the second leading jet (c). Uncertainties from the choice of the renormalisation/factorization scale as well as uncertainties from the precision of the UE measurement are not included.

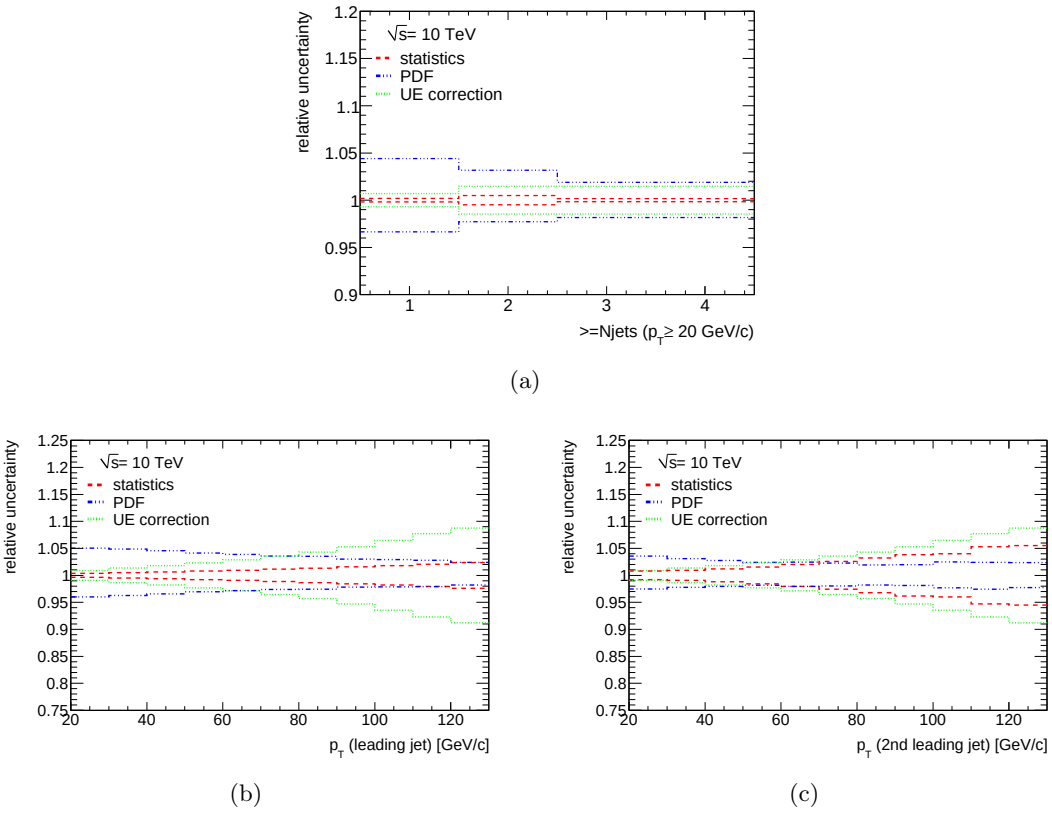

Figure 9.5: Different contributions to the total uncertainty on the theory prediction for the inclusive $Z(\rightarrow e^+e^-) +$ *jets* cross section (a), the differential cross section depending on p_T of the leading jet (b) and the differential cross section depending on p_T of the second leading jet (c).

The inclusive $Z(\rightarrow e^+e^-)+$ *jets* cross section (see Fig. 9.5(a)) is dominated by the contribution of the PDF uncertainty, decreasing with higher jet multiplicities. For high jet multiplicities the uncertainty of the PDFs is at the same order of magnitude as the uncertainty from the UE and fragmentation correction. The contribution from statistics is quite small. Tab. 9.1 summarizes

the different uncertainties on the theory predictions for the inclusive cross section, taking $Z(\rightarrow e^+e^-)+ \geq 1-3\ jets$ as examples.

Uncertainty	$Z+ \geq 1\ jet$	$Z+ \geq 2\ jets$	$Z+ \geq 3\ jets$
statistics	$\pm 0.19\%$	$\pm 0.49\%$	$\pm 0.16\%$
PDF	$(+4.41/-3.35)\%$	$(+3.17/-2.29)\%$	$(+1.90/-1.83)\%$
UE corrections	$\pm 0.70\%$	$\pm 1.46\%$	$\pm 1.46\%$
total uncertainty	$(+4.47/-3.43)\%$	$(+3.52/-2.76)\%$	$(+2.40/-2.35)\%$

Table 9.1: Different contributions to the total uncertainty on the theory predictions for the inclusive $Z(\rightarrow e^+e^-)+ \geq 1-3\ jets$ cross section.

For p_T of the leading jet, the total uncertainty on the differential cross section (see Fig. 9.5(b)) is dominated for low p_T by the PDF uncertainty and for high p_T by the uncertainty coming from the UE and fragmentation correction. The contribution from statistics is quite small. For the p_T of the second leading jet the differential cross section (see Fig. 9.5(c)), the total uncertainty is again dominated for low p_T by the PDF uncertainty and for high p_T by the uncertainty coming from the UE and fragmentation correction. But, the contribution from statistics is relatively large. Looking at further distribution, e.g. the differential cross section depending on p_T of the third jet, the total uncertainty is dominated by statistics. Tab. 9.2 summarizes the different uncertainties on the theory predictions for the differential cross section, taking two p_T ranges for the leading jet as an example.

Uncertainty	**Leading jet**	
	$20\ \mathbf{GeV/c} \leq p_T < 30\ \mathbf{GeV/c}$	$110\ \mathbf{GeV/c} \leq p_T < 120\ \mathbf{GeV/c}$
statistics	$\pm 0.37\%$	$\pm 2.06\%$
PDF	$(+5.05/-3.99)\%$	$(+2.81/-2.09)\%$
UE corrections	$\pm 0.91\%$	$\pm 7.71\%$
total uncertainty	$(+5.14/-4.11)\%$	$(+8.46/-8.25)\%$

Table 9.2: Different contributions to the total uncertainty on the differential $Z(\rightarrow e^+e^-)+\ jets$ cross section, taking two p_T ranges for the leading jet as an example.

Adding all uncertainties quadratically results in a total uncertainty for the inclusive $Z(\rightarrow e^+e^-)+ \geq 1-3\ jets$ cross section of less than 4.5%, decreasing with increasing number of jets. In contrast, the total uncertainty on the differential $Z(\rightarrow e^+e^-)+\ jets$ cross section depending on p_T of the different jets increases with increasing p_T, but is smaller than 8.5%. Nonetheless, the only real limiting factor of the total uncertainty is the precision of the PDF sets. The contribution from statistics and the UE correction, can be obtained by generating much more events.

10 From Detector Level to Hadron Level

The aim of the analysis is to measure the inclusive and the differential $Z(\rightarrow e^+e^-) + jets$ cross section. This chapter describes a feasibility study with fully simulated MC for 100 pb^{-1} at a centre of mass energy of 10 TeV including background predictions and statistical and systematic uncertainties. The reconstructed data is corrected for detector effects, using different methods.

10.1 Event Selection

As a starting point of the event selection at least two electrons are required that fulfil the identification and reconstruction requirements for electrons discussed in Sect. 6.3. For the reconstruction of the Z boson, the two electrons with invariant mass closer to the Z boson mass are chosen. In addition, the di-electron invariant mass, m_{ee}, should be within a mass window around the Z boson mass, 81 GeV/c^2 $< m_{ee} <$ 101 GeV/c^2. Finally, the electrons from the Z boson have to be well separated ($\Delta R_{ee} > 0.2$).

For the studies on VBF $H \rightarrow \tau^+\tau^-$ key quantities, at least two jets are required fulfilling the identification and reconstruction requirements described in Sect. 6.1. In addition, the leading jet is required to have a p_T above 40 GeV/c. In case the first two tagging jets are well separated in η, the behaviour of the third jet is studied by applying a cut on $\Delta\eta_{j_1 j_2}$.

10.2 Expected Signal and Background

This section describes the expected signal and background distributions for a luminosity of 100 pb^{-1} estimated by Monte Carlo. The main backgrounds for $Z(\rightarrow e^+e^-) + jets$ are QCD jets, $t\bar{t}$, $Z \rightarrow \tau^+\tau^-$ and $W \rightarrow e\nu$. In order to get enough statistics for the QCD jets background, the analysis does not apply the ID cuts. Instead the events are scaled with the rejection.

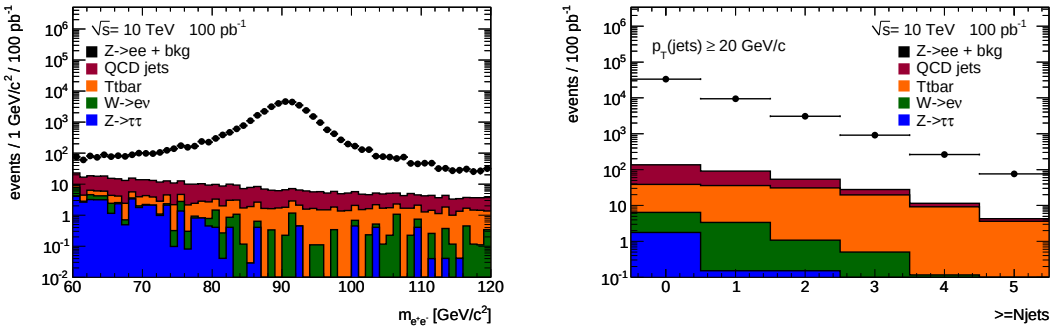

(a) (b)

Figure 10.1: Distributions for the expectation of signal and background from Monte Carlo (a) invariant di-electron mass (b) jet multiplicity after requiring a reconstructed Z with a mass between 81 GeV/c^2 and 101 GeV/c^2. The points show the expectation in data and the filled histograms represent the different background contributions.

Fig. 10.1(a) shows the invariant di-electron mass in signal and backgrounds. Outside the di-electron mass range between 81 GeV/c^2 and 101 GeV/c^2 the distribution for the invariant di-electron mass is mainly given by the background. Fig. 10.1(b) shows the inclusive $Z(\rightarrow e^+e^-)+jets$ cross section and Tab. 10.1 summarizes the contributions from the main backgrounds.

	$Z(\rightarrow e^+e^-)+\geq 1jet$	$Z(\rightarrow e^+e^-)+\geq 2jets$	$Z(\rightarrow e^+e^-)+\geq 3jets$
Process	**# events**	**# events**	**# events**
$Z \rightarrow e^+e^-$	9413.2 ± 97.1	3032.2 ± 55.1	889.1 ± 29.9
$QCDjets$	54.8 ± 7.4	23.1 ± 4.8	7.8 ± 2.8
$t\bar{t}$	23.9 ± 4.9	21.9 ± 4.7	14.3 ± 3.8
$W \rightarrow e\nu$	3.2 ± 1.8	0.9 ± 1.0	0.5 ± 0.7
$Z \rightarrow \tau^+\tau^-$	0.2 ± 0.4	0.2 ± 0.4	0.0 ± 0.2
total background	82.1 ± 9.1	46.0 ± 6.8	22.6 ± 4.8
	fraction [%]	**fraction** [%]	**fraction** [%]
$Z \rightarrow e^+e^-$	99.14 ± 1.03	98.51 ± 1.79	97.52 ± 3.27
$QCDjets$	0.58 ± 0.08	0.75 ± 0.16	0.86 ± 0.31
$t\bar{t}$	0.25 ± 0.06	0.71 ± 0.16	1.57 ± 0.42
$W \rightarrow e\nu$	0.03 ± 0.02	0.03 ± 0.04	0.05 ± 0.07
$Z \rightarrow \tau^+\tau^-$	0.002 ± 0.005	0.005 ± 0.02	0.004 ± 0.03
total background/all events	0.86 ± 0.10	1.49 ± 0.22	2.48 ± 0.53

Table 10.1: Summary of the contributions from different backgrounds to the inclusive $Z(\rightarrow e^+e^-)+1-3\ jets$ cross section measurement.

The background is dominated by QCD jets and $t\bar{t}$. However, the backgrounds are mostly negligible. With increasing number of jets in the event the $t\bar{t}$ background becomes more and more important. Nevertheless, the contribution is smaller than 2% for $Z(\rightarrow e^+e^-)+\geq 3\ jets$. For the QCD jets background, even if it was underestimated by a factor of 5, the contribution for $Z(\rightarrow e^+e^-)+\geq 3\ jets$ would still correspond to less than 8%.

Fig. 10.2 - 10.5 show the expected signal and backgrounds for the differential $Z(\rightarrow e^+e^-)+jets$

cross section measurement.

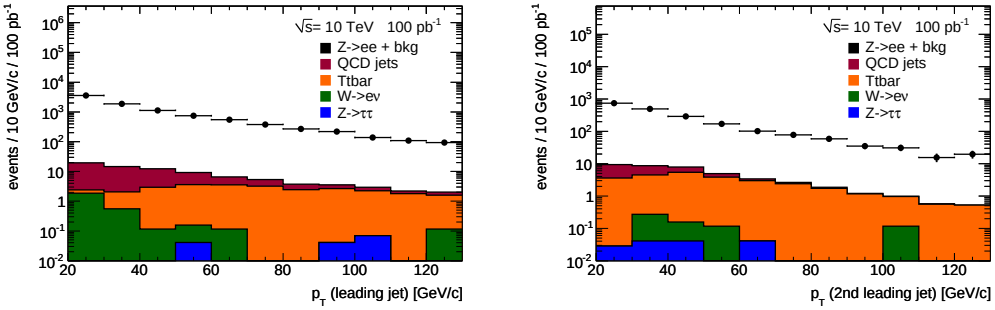

(a) (b)

Figure 10.2: Distributions for the expectation of signal and backgrounds from Monte Carlo for the p_T of the leading jet (a) and the p_T of the second leading jet (b). The points show the expectation in data and the filled histograms represent the different background contributions.

Fig. 10.2 shows the expected signal and backgrounds for the p_T of the leading jet (a) and the p_T of the second leading jet (b). $t\bar{t}$ has a harder p_T distribution for the jets compared to $Z(\rightarrow e^+e^-) + \ jets$.

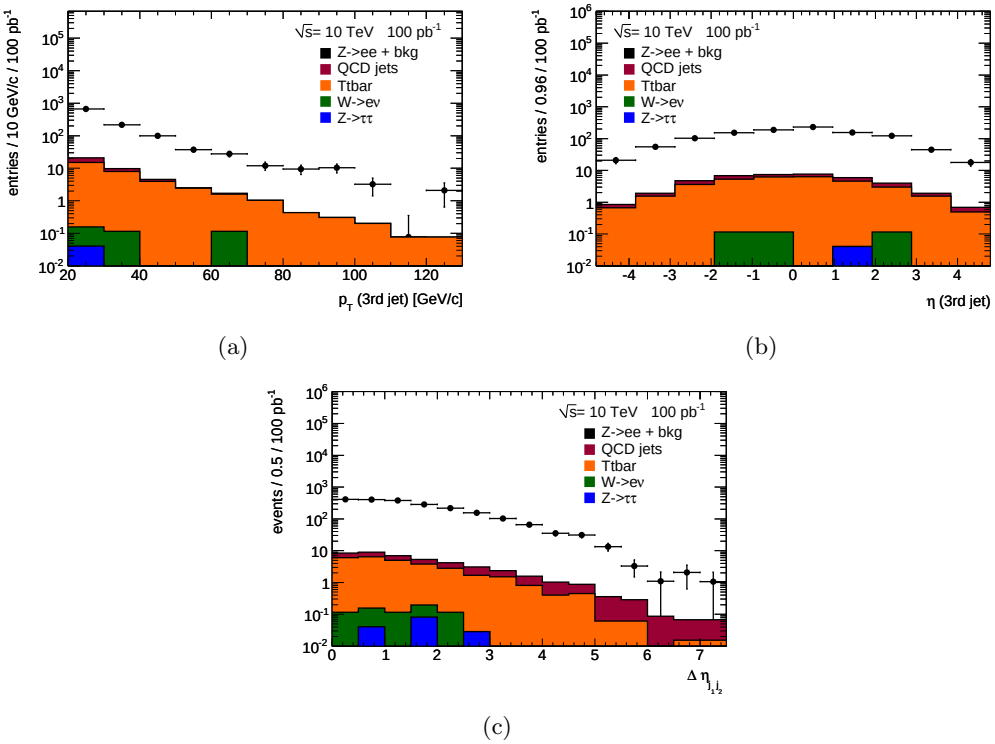

(a) (b)

(c)

Figure 10.3: Distributions for the expectation of signal and backgrounds from Monte Carlo for the p_T of the third jet (a), the η of the third jet (b) and the pseudorapidity gap between the two tagging jets (c). The points show the expectation in data and the filled histograms represent the different background contributions.

Fig. 10.3 shows the expected signal and backgrounds for the VBF H$\rightarrow \tau\tau$ key quantities. The

distributions for the third jet are shown without a cut on the pseudorapidity gap. Contrary to that, Fig. 10.4 and Fig. 10.5 show a comparison of both distributions with two different cuts on the pseudorapidity gap, once with the cut predicted from the Higgs group $\Delta\eta_{j_1 j_2} > 4.4$ and once with a smaller cut to gain statistics $\Delta\eta_{j_1 j_2} > 3.0$.

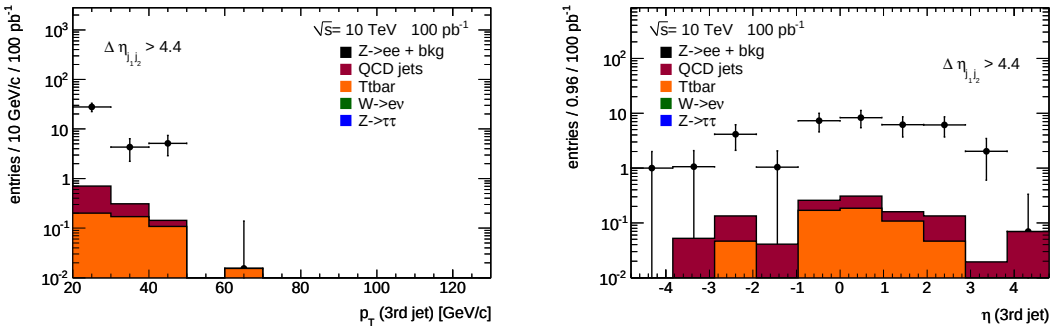

(a) (b)

Figure 10.4: Distributions for the expectation of signal and backgrounds from Monte Carlo for the third jet with a cut on the pseudorapidity gap $\Delta\eta_{j_1 j_2} > 4.4$ (a) p_T (b) η. The points show the expectation in data and the filled histograms represent the different background contributions.

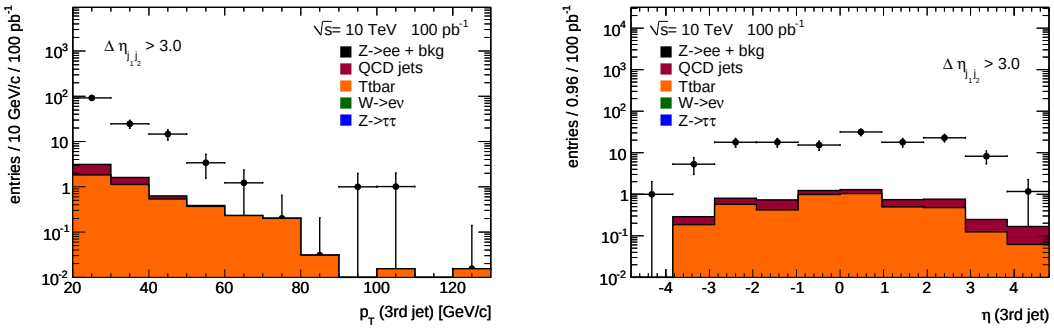

(a) (b)

Figure 10.5: Distributions for the expectation of signal and backgrounds from Monte Carlo for the 3rd jet with a cut on the pseudorapidity gap $\Delta\eta_{j_1 j_2} > 3.0$ (a) p_T (b) η. The points show the expectation in data and the filled histograms represent the different background contributions.

For $\Delta\eta_{j_1 j_2} > 4.4$ only 36 $Z \to e^+e^-$ events with a third jet are expected. The choice of a cut at the pseudorapidity gap at 3.0 provides 132 $Z \to e^+e^-$ events with a third jet, which is much better suited for a first estimate how the distributions will look like.

10.2.1 Comparison between 10 TeV and 14 TeV

Fig. 10.6 shows the comparison of the inclusive $Z(\rightarrow e^+e^-) + \ jets$ cross section between 10 TeV (see Fig. 10.6(a)) and 14 TeV (see Fig. 10.6(b)). In this case the jets are required to have a minimum p_T of 40 GeV/c. The absolute contributions are summarized in Tab. 10.2. The results for 14 TeV are taken from [48].

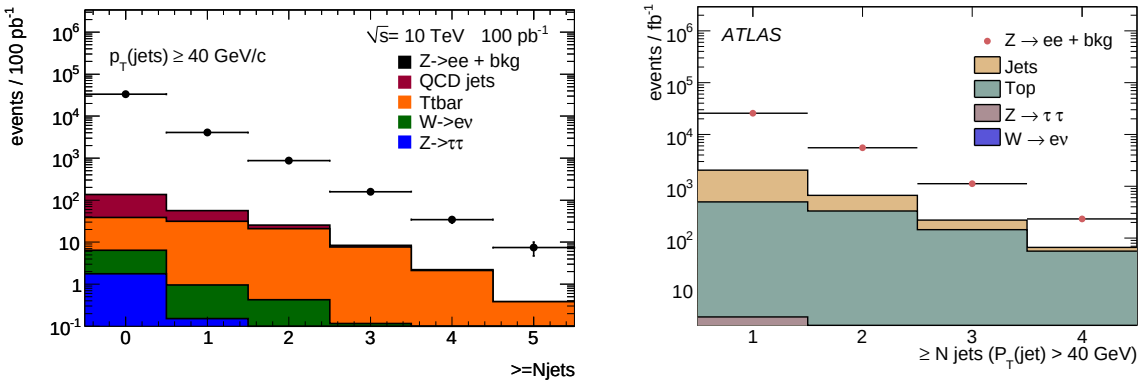

(a) (b)

Figure 10.6: Jet multiplicity distributions for jets with $p_T > 40$ GeV/c for a centre of mass energy of 10 TeV for $\int \mathcal{L} = 100$ pb^{-1} (a) and 14 TeV for $\int \mathcal{L} = 1$ fb^{-1} (b).

Process	$Z \rightarrow e^+e^- + \geq 1jet$ **fraction** [%]	$Z \rightarrow e^+e^- + \geq 2jets$ **fraction** [%]	$Z \rightarrow e^+e^- + \geq 3jets$ **fraction** [%]
	10 **TeV**		
$Z \rightarrow e^+e^-$	98.81 $\pm$ 1.56	97.68 $\pm$ 3.37	95.91 $\pm$ 7.81
$QCDjets$	0.61 $\pm$ 0.13	0.52 $\pm$ 0.25	0.46 $\pm$ 0.55
$t\bar{t}$	0.55 $\pm$ 0.12	1.75 $\pm$ 0.46	3.55 $\pm$ 1.51
$W \rightarrow e\nu$	0.02 $\pm$ 0.03	0.04 $\pm$ 0.07	0.07 $\pm$ 0.22
$Z \rightarrow \tau^+\tau^-$	0.004 $\pm$ 0.01	0.01 $\pm$ 0.04	0.00 $\pm$ 0.00
total background/all events	1.19 $\pm$ 0.18	2.32 $\pm$ 0.52	4.09 $\pm$ 1.62
	14 **TeV**		
$Z \rightarrow e^+e^-$	91.9 $\pm$ 0.8	87.9 $\pm$ 1.3	80.0 $\pm$ 2.4
$QCDjets$	6.0 $\pm$ 0.4	6.0 $\pm$ 0.8	6.9 $\pm$ 1.8
$t\bar{t}$	1.9 $\pm$ 0.1	6.0 $\pm$ 0.4	13.0 $\pm$ 1.4
$W \rightarrow e\nu$	0.1 $\pm$ 0.05	0.1 $\pm$ 0.05	0.05 $\pm$ 0.1
$Z \rightarrow \tau^+\tau^-$	0.01 $\pm$ 0.01	0.01 $\pm$ 0.01	0.01 $\pm$ 0.01
total background/all events	8.0 $\pm$ 0.6	12.1 $\pm$ 0.9	20.0 $\pm$ 2.3

Table 10.2: Comparison of the different contribution to the inclusive $Z(\rightarrow e^+e^-) + \ jets$ cross section for a centre of mass energy of 10 TeV and 14 TeV.

The background contributions from $t\bar{t}$ and QCD are less important for a centre of mass energy of 10 TeV. The cross section for $t\bar{t}$ increases much more with increasing centre of mass energy compared to the one for $Z(\rightarrow e^+e^-) + \ jets$, see Fig. 3.2. The difference in the contribution

for QCD jets cannot be ascribed to different slopes of the cross sections between 10 TeV and 14 TeV of $Z(\rightarrow e^+e^-) + \ jets$ and QCD jets. Instead, the difference comes from applying an additional cone isolation for the electrons, which was not used for the CSC studies because of a bug in the reconstruction.

10.2.2 Background Estimation

The estimation of the $t\bar{t}$ background will be done using Monte Carlo, which has to be validated with $t\bar{t}$ selection in the first data [48]. For the estimation of the QCD jets background a data-driven method has to be used. This can be done using side band fits to the Z mass peak in the distribution of the invariant di-electron mass. In case that the $t\bar{t}$ background is well known, it can be subtracted from the background distribution. The remaining background distribution of the di-electron mass is highly dominated by QCD jets, see Tab. 10.1. The remaining total distribution, including signal and backgrounds, is fitted with the sum of an exponential function and a Breit-Wigner distribution folded with a Gaussian distribution. The fitted function is dominated by the exponential function at the sides and by the Breit-Wigner/ Gaussian distributions in the centre. Therefore, the background from QCD jets can be described by the exponential function using the fit parameters and then extrapolated over the whole range.

10.3 Corrections for Detector Effects

For comparison with theoretical predictions at the hadron level, the reconstructed data has to be corrected from the detector level to the hadron level. The reconstructed data has to be corrected for resolution effects, non linearities and efficiencies for the lepton and jet reconstruction. In the following sub sections four different methods for the corrections of detector effects are presented using two statistically independent MC sets of 100 pb^{-1}. The different sources of uncertainties are discussed in Sect. 10.4. The comparison of the different methods with their advantages and disadvantages is made in Sect. 11.1.

10.3.1 Preliminary Studies on the Event Topology

The jet multiplicity in $Z(\rightarrow e^+e^-)+$ *jets* events has an impact on the kinematics of the electrons and jets. Fig. 10.7 shows the p_T of the electron (a), the p_T of the jet (b), the ΔR between the electrons (c) and the minimum ΔR between the electrons and the jets (d) at generator level for different jet multiplicities.

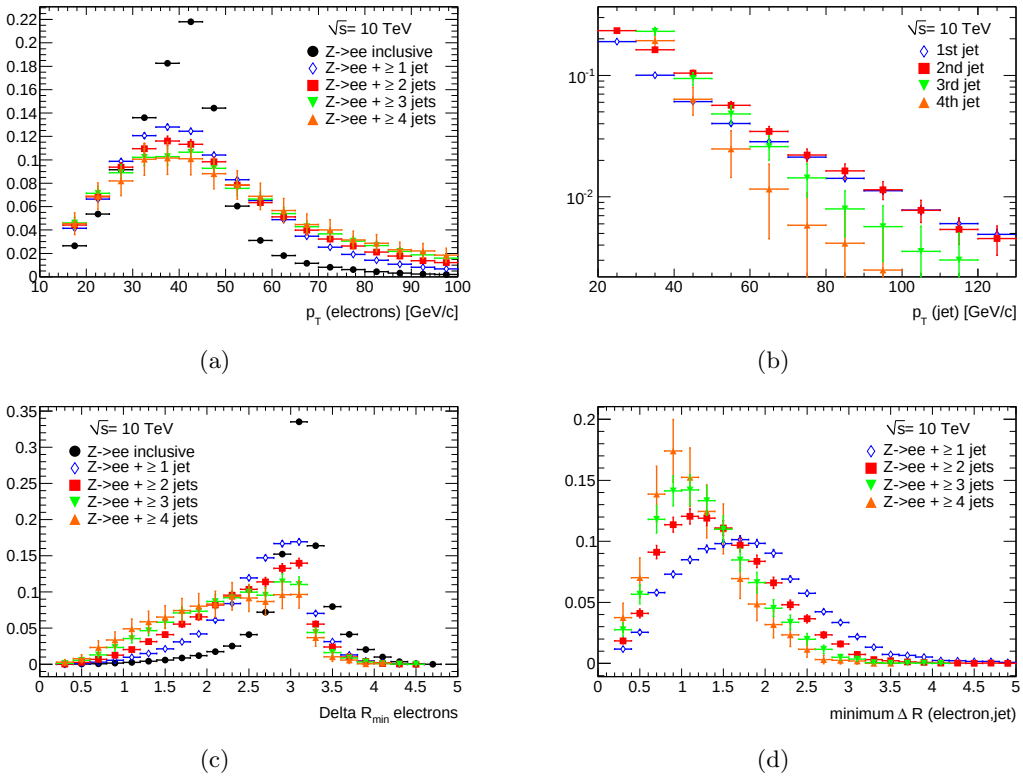

Figure 10.7: Distributions of (a) p_T of the electrons, (b) p_T of the jet, (c) Δ R between the two electrons and (d) minimum Δ R between one of the electrons and one of the jets at generator level for different jet multiplicities. The histograms are normalized to unity.

The transverse momentum distribution for the electrons is highly correlated with the numbers of jets in the event. The higher the boost of the Z boson, which decays to two electrons, the higher the probability that the Z boson is balanced with a larger number of jets with small transverse momentum. Due to higher boost of the Z boson, the electrons are much more collimated with increasing number of jets. Hence the stability of the electron reconstruction efficiency with increasing boost of the Z boson has to be checked. The transverse momentum distributions of the various jets vary a lot, which implies that corrections on the jets have to be calculated for each jet separately. With increasing number of jets in the event the minimum ΔR between the electrons and the jets becomes smaller, which may have an impact on the electron reconstruction efficiency. Fig. 10.8 shows the Z boson reconstruction efficiency as a function of the jet multiplicity (a) and the p_T of the leading jet (b).

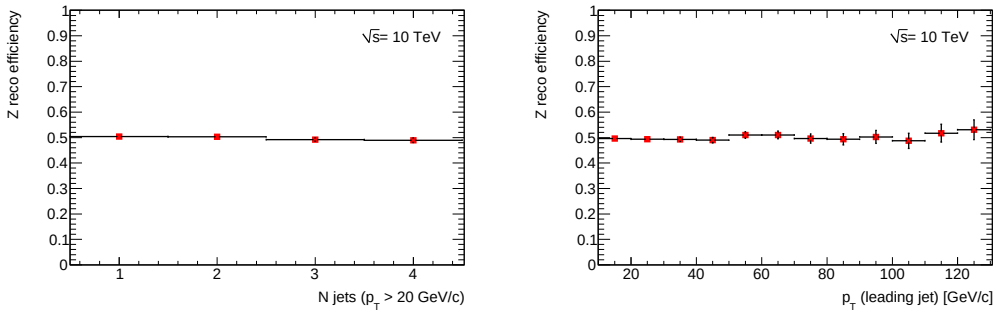

(a) (b)

Figure 10.8: *Z* boson reconstruction efficiency as a function of (a) the jet multiplicity and (b) the p_T of the leading jet.

From these plots follows that the Z boson reconstruction efficiency is stable with respect to the jet multiplicity and the p_T of the leading jet.

10.3.2 Factorized Corrections

The first method for the correction of detector effects makes the assumption that in leading order all corrections for detector effects factorize and therefore can be treated separately. The factorized corrections are splited in three parts:

- **Corrections for residual miscalibrations:**
  Due to the fact that the detector is not one homogeneous body and effects like inactive material, noise, pile-up and out-of-cone showering exist, energy-scale corrections depend on p_T or η. In order to make sure that the transverse momentum on detector level is the same as on hadron level, the reconstructed objects have to be corrected for these miscalibrations. This correction has to be applied on every object.

- **Corrections for shape distortion due to resolution effects:** After correcting for the nonlinearity of the jet energy scale, the transverse momenta of the objects are on average the same, but the shapes look quite different. This difference can be ascribed to resolution effects of the detector. Due to the shape of the jet p_T distribution, more jets migrate to larger values of p_T than to lower values of p_T.

- **Corrections for reconstruction efficiency:**
  Again due to the fact that the detector is not a fully homogeneous body and does not cover the whole 4π region, some cracks exist in which objects can not be reconstructed. The split-and-merge procedure in the jet reconstruction can lead to different results on hadron level and on reconstructed level. The possibility of reconstruction is also dependent on p_T; the higher the p_T of an object the higher the probability for this to be reconstructed.

Corrections for shape distortion due to resolution effects and corrections for reconstruction efficiencies are treated as weights of the event depending on the requirements of the selection (e.g. asking for at least two jets, the event has to be weighted two times with the corresponding weight of each jet).

For $Z \rightarrow ee + \ jets$, the corrections for detector effects have to be applied for electrons and jets. The dominant contribution comes from the reconstruction efficiency of the electrons. Corrections on jets have a small impact on the inclusive $Z \rightarrow e^+e^-$ cross section but highly bias the differential cross sections, especially the p_T spectra of the different jets. Low p_T jets are much more influenced by detector effects.

As a starting point truth electrons are matched to reconstructed electrons in η and ϕ ($\Delta R < 0.2$). The p_T of the reconstructed electron divided by the p_T of the corresponding truth electrons is plotted ones for different bins of the reconstructed η and p_T and ones for different bins of the truth η and p_T. Both distributions are fitted with a Gaussian in the range $0.95 - 1.05$. From the mean value of the first distribution the non-linearity of the electron energy can be determined and sigma of the second distribution gives σ_{p_T}/p_T for the chosen bin combination. Fig. 10.9 and Fig. 10.10 show some examples of the fitted distributions for the determination of linearity and σ_{p_T}/p_T.

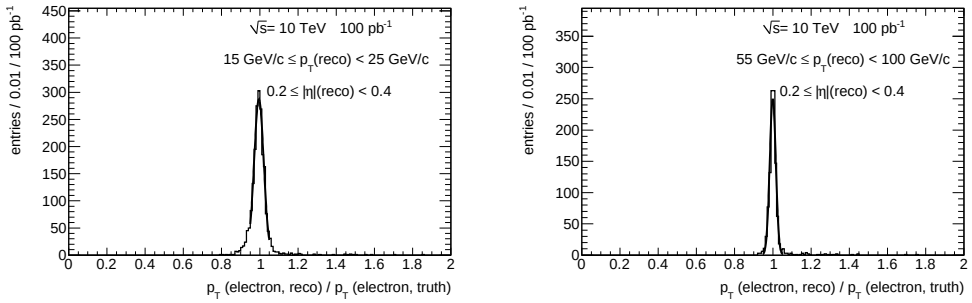

(a) (b)

Figure 10.9: Examples for the fitted distribution of the p_T of the reconstructed electron (matched to a truth electron) over the p_T of the truth electron for the determination of linearity. The fits are applied for different reconstructed p_T and η bins: 15 GeV/c $\leq p_T(reco) <$ 25 GeV/c and $0.2 \leq |\eta|(reco) < 0.4$ (a) and 55 GeV/c $\leq p_T(reco) <$ 100 GeV/c and $0.2 \leq |\eta|(reco) < 0.4$ (b).

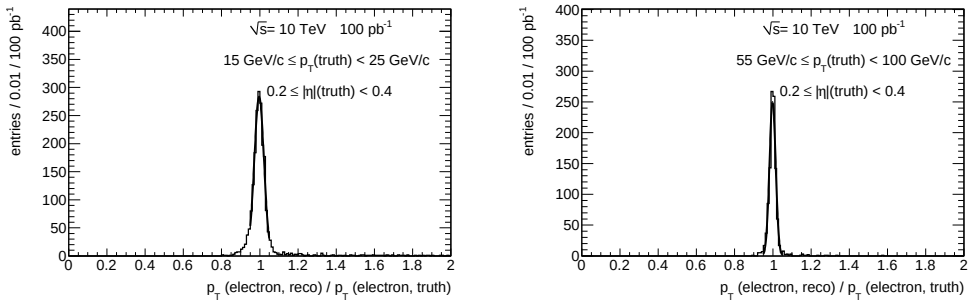

(a) (b)

Figure 10.10: Examples for the fitted distribution of the p_T of the reconstructed electron (matched to a truth electron) over the p_T of the truth electron for the determination of σ_{p_T}/p_T. The fits are applied for different truth p_T and η bins: 15 GeV/c $\leq p_T(truth) <$ 25 GeV/c and $0.2 \leq |\eta|(truth) < 0.4$ (a) and 55 GeV/c $\leq p_T(truth) <$ 100 GeV/c and $0.2 \leq |\eta|(truth) < 0.4$ (b).

From the different mean values the residual miscalibration (p_T(electron,reco)/p_T(electron,truth)) can be directly plotted as a function of η for the different p_T ranges (see Fig. 10.11(a)). σ_{p_T}/p_T is shown in Fig. 10.11(b). For electrons with a low p_T the distributions are clearly wider. σ_{p_T}/p_T is larger in the calorimeter cracks than in the central and forward regions. The effect of resolution is shown by smearing the truth electrons with their corresponding σ_{p_T}/p_T and dividing it by the original truth spectrum (see Fig. 10.11(c)). Fig. 10.11(d) shows the electron ID (medium no isolated + calorimeter isolation) efficiency.

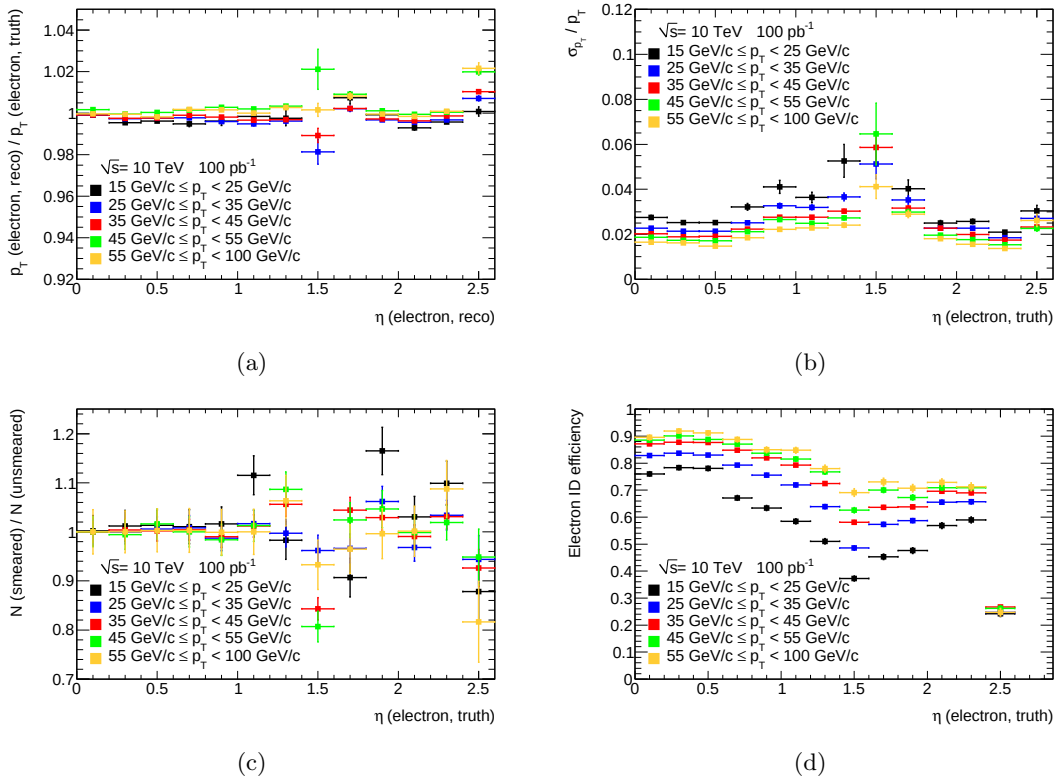

(a) (b) (c) (d)

Figure 10.11: Residual miscalibrations for electrons (a), σ_{p_T}/p_T (b), shape distortion due to resolution effects (c) and electron ID efficiency for medium no isolated electrons with calorimeter isolation (d).

In order to correct the electrons in an event for detector effects, both electrons are corrected for the residual miscalibrations. Afterwards, the event is weighted with the corrections for the shape distortion and the reconstruction efficiency of each electron.

In the following, the corrections for the jets are explained. For the jets two different factorized corrections are used. One is only p_T dependent and the other one distinguishes in addition between the central and the forward region of the detector. Afterwards, both methods are compared.

p_T dependent Correction

For the binning in p_T 17 bins are chosen such that in every bin the number of events is nearly the same. The procedure to determine the jet corrections is the same as for the electrons. But instead of fitting the reconstructed matched jet p_T normalized to the corresponding truth jet p_T with a Gaussian in the range of $0.95 - 1.05$, the fitting is done in a range of $0.8 - 1.2$. The resolution of the jets is lower than the resolution of the electrons.
Fig. 10.12 and Fig. 10.13 show some extreme examples for the fitted distributions and Fig. 10.14 shows the different distributions, which are necessary for the correction.

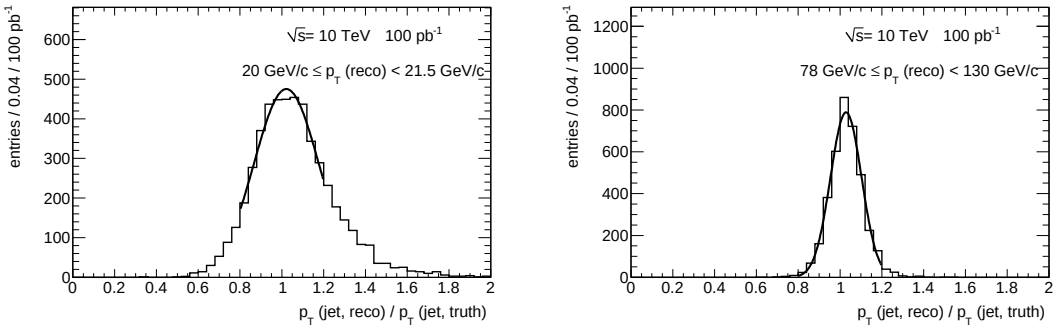

(a) (b)

Figure 10.12: Examples for the fitted distribution of the p_T of the reconstructed jet (matched to a truth jet) over the p_T of the truth jet for the determination of linearity. The fits are applied for different reconstructed p_T bins: 20 GeV/c $\leq p_T(reco) <$ 21.5 GeV/c (a) and 78 GeV/c $\leq p_T(reco) <$ 130 GeV/c (b).

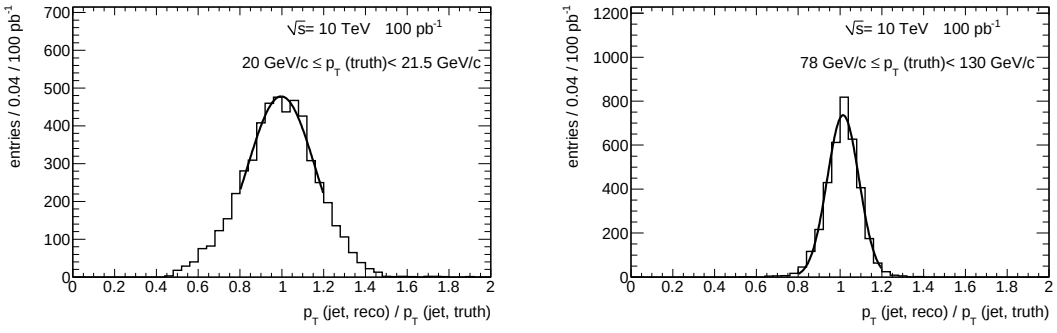

(a) (b)

Figure 10.13: Examples for the fitted distribution of the p_T of the reconstructed jet (matched to a truth jet) over the p_T of the truth jet for the determination of σ_{p_T}/p_T. The fits are applied for different truth p_T bins: 20 GeV/c $\leq p_T(truth) <$ 21.5 GeV/c (a) and 78 GeV/c $\leq p_T(truth) <$ 130 GeV/c (b).

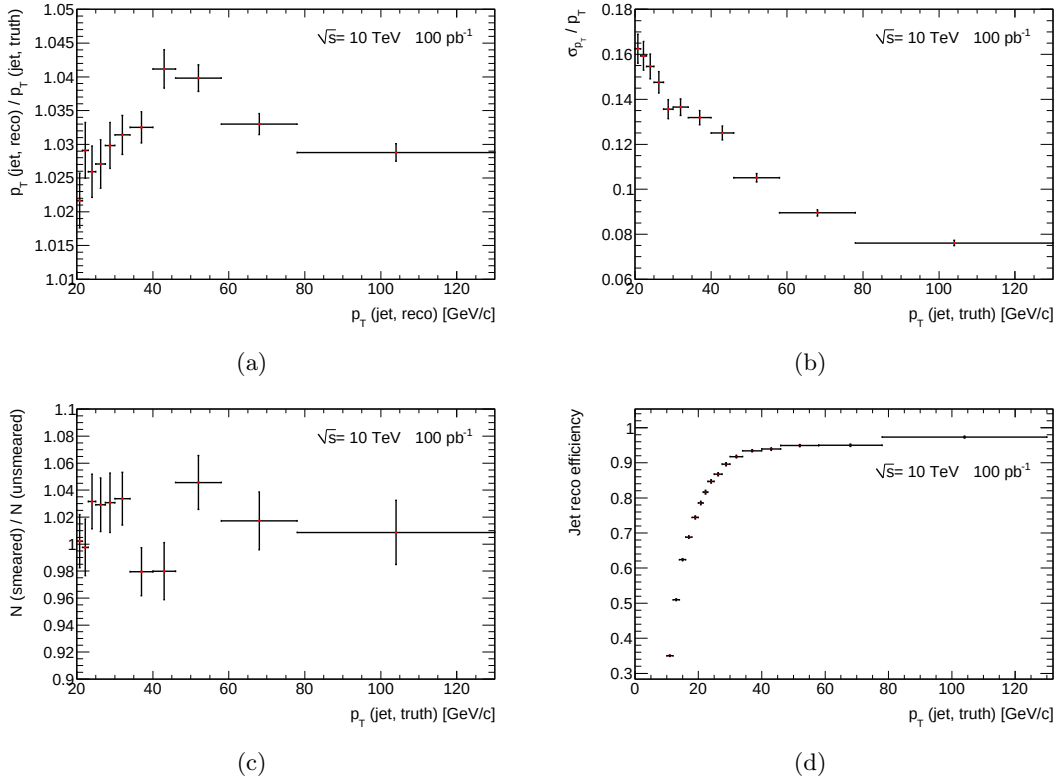

Figure 10.14: Residual miscalibration for jets (a), σ_{p_T}/p_T (b), shape distortion due to resolution effects (c) and jet reconstruction efficiency (d).

p_T and η dependent Correction

In addition to the binning in p_T, a separation in central ($0 \leq \eta < 1.7$) and forward region ($1.7 \leq \eta < 4.8$) of the detector is done. Examples for the fitted distribution of the p_T of the reconstructed jet (matched to a truth electron) over the p_T of the truth jet are shown in Fig. 10.15 and Fig. 10.16. Fig. 10.17 shows the different distributions for the corrections of detector effects resulting from the fits.

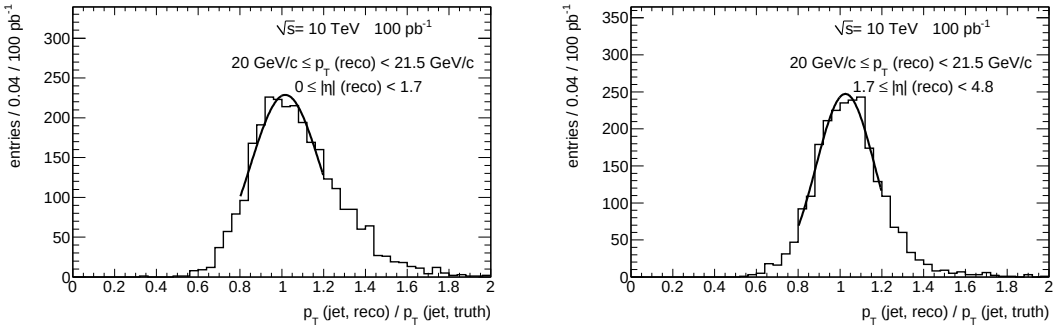

(a) (b)

Figure 10.15: Examples for the fitted distribution of the p_T of the reconstructed jet (matched to a truth jet) over the p_T of the truth jet for the determination of linearity. The fits are applied for different reconstructed p_T and η bins: $0 \leq |\eta|(reco) < 1.7$, 20 GeV/c $\leq p_T(reco) <$ 21.5 GeV/c (a) and $1.7 \leq |\eta| < 4.8$, 20 GeV/c $\leq p_T(reco) <$ 21.5 GeV/c (b).

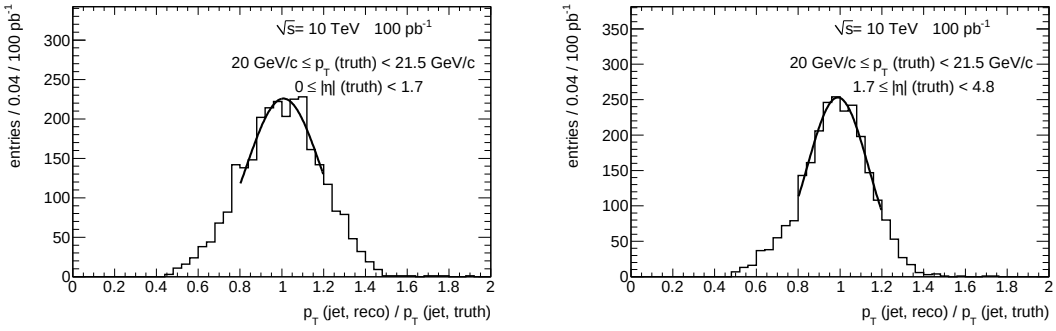

(a) (b)

Figure 10.16: Examples for the fitted distribution of the p_T of the reconstructed jet (matched to a truth jet) over the p_T of the truth jet for the determination of σ_{p_T}/p_T. The fits are applied for different truth p_T and η bins: $0 \leq |\eta|(truth) < 1.7$, 20 GeV/c $\leq p_T(truth) <$ 21.5 GeV/c (a) and $1.7 \leq |\eta|(truth) < 4.8$, 20 GeV/c $\leq p_T(truth) <$ 21.5 GeV/c (b).

The corrections for residual miscalibrations and shape distortion are smaller in the forward region than in the central region. The reconstruction efficiency for low p_T jets in the forward regions is better than in the central region.

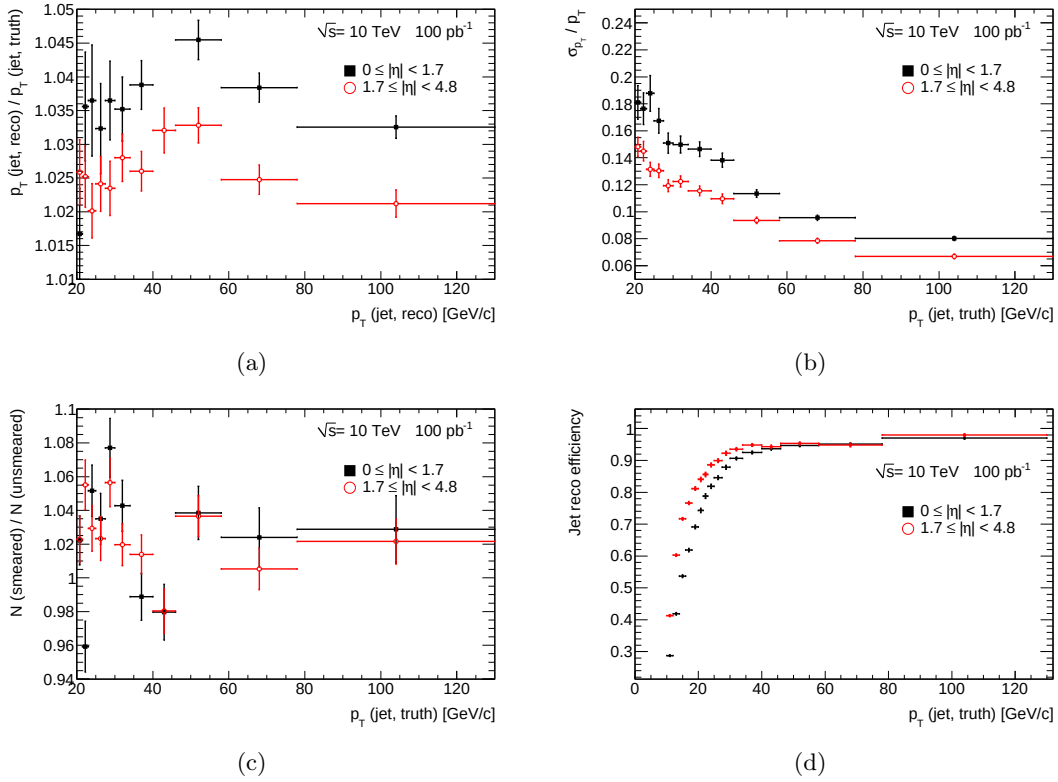

Figure 10.17: Residual miscalibration for jets (a), σ_{p_T}/p_T (b), shape distortion due to resolution effects (c) and jet reconstruction efficiency (d) depending on p_T and η.

Comparison of Distribution with and without Corrections

Fig. 10.18-10.21 show the comparison of p_T and η distributions for the leading and the second leading jet at different stages of the correction procedure with the p_T and η distribution given from the Monte Carlo generator. The corrections are applied on a test sample, which is statistically independent from the training sample. Both samples correspond to an integrated luminosity of 100 pb^{-1}. In addition the relative residuals are shown, which are the reconstructed distributions corrected for electrons and jets in p_T and η minus the truth distributions divided by the truth distributions.

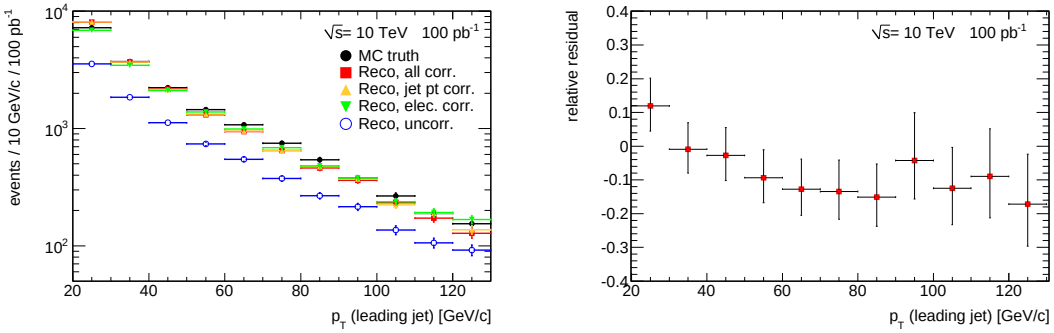

(a) (b)

Figure 10.18: Comparison of the p_T distributions for the leading jet (a) and the concerning relative residual (b). The uncorrected reconstructed distribution is shown in blue and the truth distribution is shown in black. On the green distribution only an electron correction has been applied whereas the orange distribution includes in addition the p_T dependent corrections for the jets. The red distribution incorporates the electron corrections and the p_T and η dependent jet corrections.

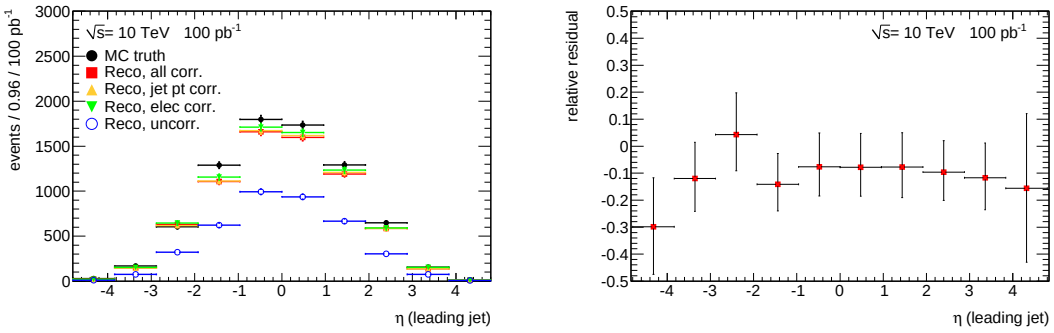

(a) (b)

Figure 10.19: Comparison of the η distribution for the leading jet (a) and the concerning relative residual (b). The uncorrected reconstructed distribution is shown in blue and the truth distribution is shown in black. On the green distribution only an electron correction has been applied whereas the orange distribution includes in addition the p_T dependent corrections for the jets. The red distribution incorporates the electron corrections and the p_T and η dependent jet corrections.

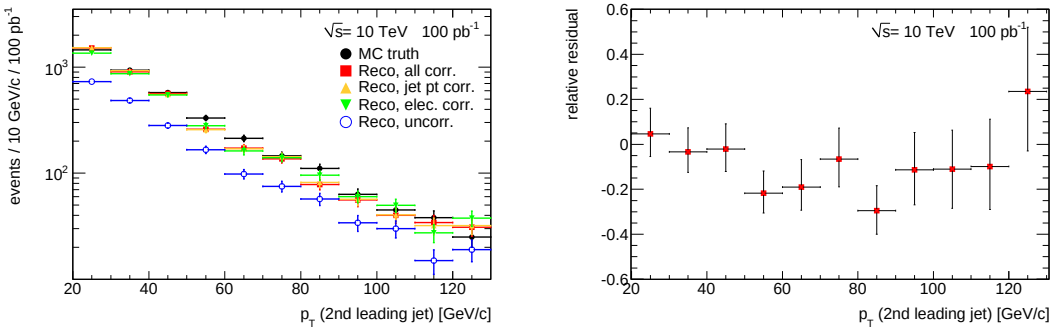

(a) (b)

Figure 10.20: Comparison of the p_T distributions for the second leading jet (a) and the concerning relative residual (b). The uncorrected reconstructed distribution is shown in blue and the truth distribution is shown in black. On the green distribution only an electron correction has been applied whereas the orange distribution includes in addition the p_T dependent corrections for the jets. The red distribution incorporates the electron corrections and the p_T and η dependent jet corrections.

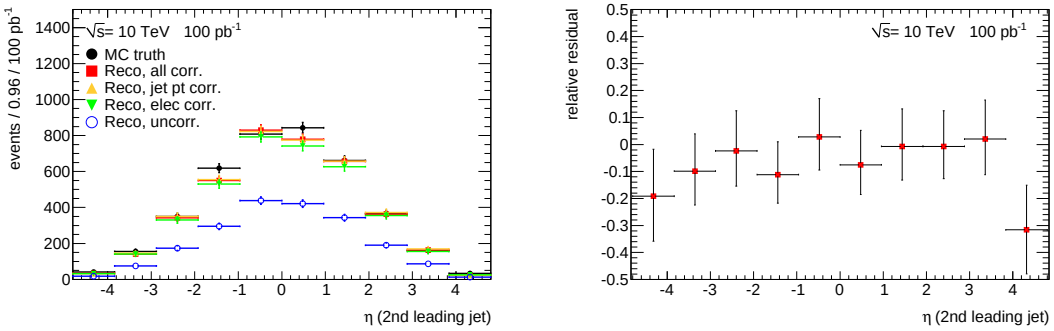

(a) (b)

Figure 10.21: Comparison of the η distribution for the second leading jet (a) and the concerning relative residual (b). The uncorrected reconstructed distribution is shown in blue and the truth distribution is shown in black. On the green distribution only an electron correction has been applied whereas the orange distribution includes in addition the p_T dependent corrections for the jets. The red distribution incorporates the electron corrections and the p_T and η dependent jet corrections.

As mentioned before, the correction for the electrons has the highest influence in total, but the corrections for the jets characterize the shape. Deriving the corrections separately for the two η regions has not a high influence within errors on the distributions of the leading and second leading jet. From the relative residuals follows that the method has a precision of $10\% - 20\%$, which seems to come from a bias of the method, due to the assumption that all corrections factorize. In addition, the bin centre is used to determine the corrections. It might be better to use the centre of gravity of each bin to take the distribution in each bin into account.

Fig. 10.22-10.24 show the distributions for the key quantities of the Higgs boson analysis. From Fig. 10.23(a) and Fig. 10.24(a) follow that the improvement of the additional η correction is not negligible for the η and p_T distributions of the third jets. However, this additional correction

does not reduce the difference between the truth and the corrected reconstructed distributions in the very central region. Increasing the number of bins for the pseudo rapidity in the central region could solve this problem. For the pseudo rapidity gap (see Fig. 10.22(a)) there is no improvement. This is because this distribution is built by the η distributions of the leading and second leading jet, which, as mentioned before do not change.

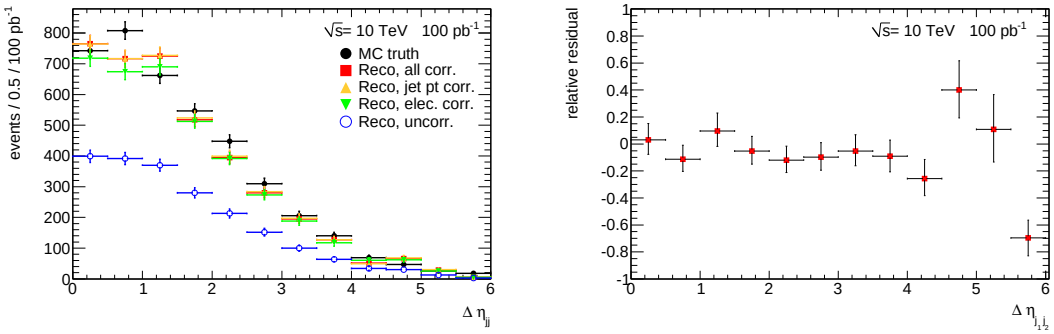

(a) (b)

Figure 10.22: Comparison of the pseudorapidity gap distributions (a) and the concerning relative residual (b). The uncorrected reconstructed distribution is shown in blue and the truth distribution is shown in black. On the green distribution only an electron correction has been applied whereas the orange distribution includes in addition the p_T dependent corrections for the jets. The red distribution incorporates the electron corrections and the p_T and η dependent jet corrections.

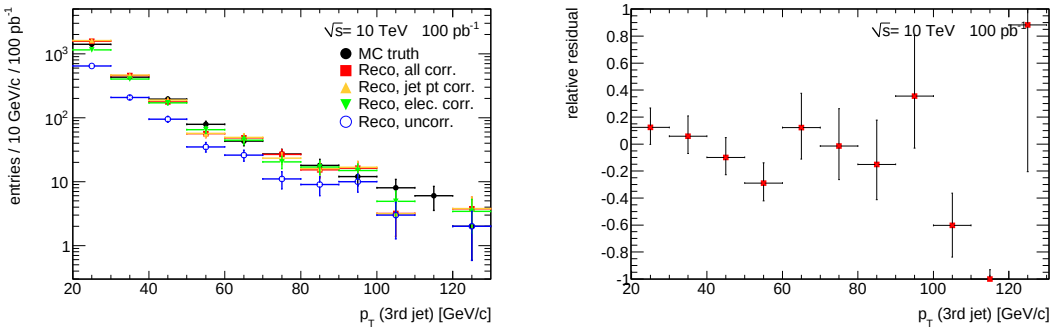

(a) (b)

Figure 10.23: Comparison of the p_T distributions for the third jet (a) and the concerning relative residual (b). The uncorrected reconstructed distribution is shown in blue and the truth distribution is shown in black. On the green distribution only an electron correction has been applied whereas the orange distribution includes in addition the p_T dependent corrections for the jets. The red distribution incorporates the electron corrections and the p_T and η dependent jet corrections.

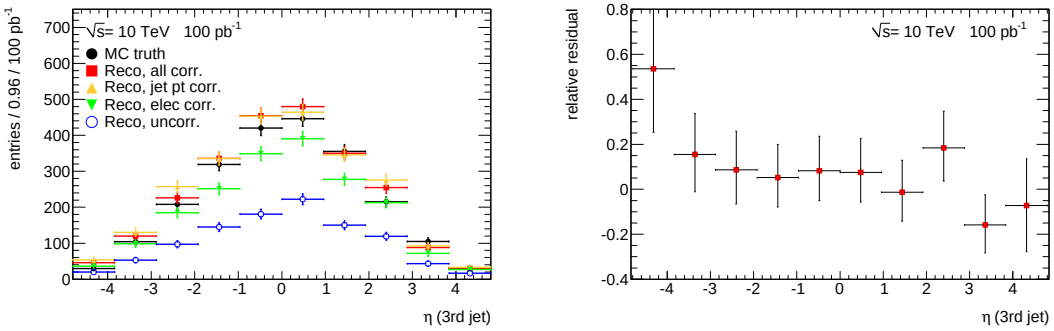

(a) (b)

Figure 10.24: Comparison of the η distribution for the third jet (a) and the concerning relative residual (b). The uncorrected reconstructed distribution is shown in blue and the truth distribution is shown in black. On the green distribution only an electron correction has been applied whereas the orange distribution includes in addition the p_T dependent corrections for the jets. The red distribution incorporates the electron corrections and the p_T and η dependent jet corrections.

In order to optimize the results of the factorized correction, the correction has to be calculated for each jet separately, as discussed previously, such that the different shapes are taken into account. In addition using more bins in η can provide a better result. For both optimisations more statistics for the MC sets are needed. Finally, due to the fact that the detector measures the energy and forward jets are important, it could be better to use the energy instead of the transverse momentum for the correction.

10.3.3 Matrix Inversion

In the second method all corrections are summarized in one black-box. In the Monte Carlo sample, a binned Matrix, M_{ij}, is constructed which includes event by event the observable on detector level vs. hadron level. The following equation describes the transformation from hadron level h to detector level d for the spectrum of this observable

$$d = M \cdot h. \tag{10.1}$$

Using the reconstruction efficiency as a function of the observable, the matrix is normalized to the probability p that an event, which belongs to the j bin at hadron level is reconstructed in a special bin i at detector level

$$p(i,j) = \text{number of events in } M_{ij} \cdot \frac{\text{reconstruction efficiency for an event in bin } j}{\text{Sum of all events in column } j}. \tag{10.2}$$

In order to correct the measured observables for detector effects, Eq. 10.1 has to be solved for h

$$h = M^{-1} d. \tag{10.3}$$

Here, the inverse matrix is calculated using Octave-2.1.57 [57]. Using this method there is no global correction, every spectrum of an observable of a particle has to be treated separately. The next section describes the method taking p_T and η of the leading jet as an example.

Corrections for the Leading Jet

The matrix M_{ij} is binned into twelve bins of 10 GeV/c each, ranging from 10 GeV/c to 130 GeV/c, for the observable p_T using a training sample corresponding to an integrated luminosity of 100 pb^{-1}, shown in Fig. 10.28(a). Fig. 10.28(b) shows the jet reconstruction efficiency for the same binning and Fig. 10.25(c) shows the resulting normalized matrix. Then the inverse matrix is calculated (see Fig. 10.25(d)).

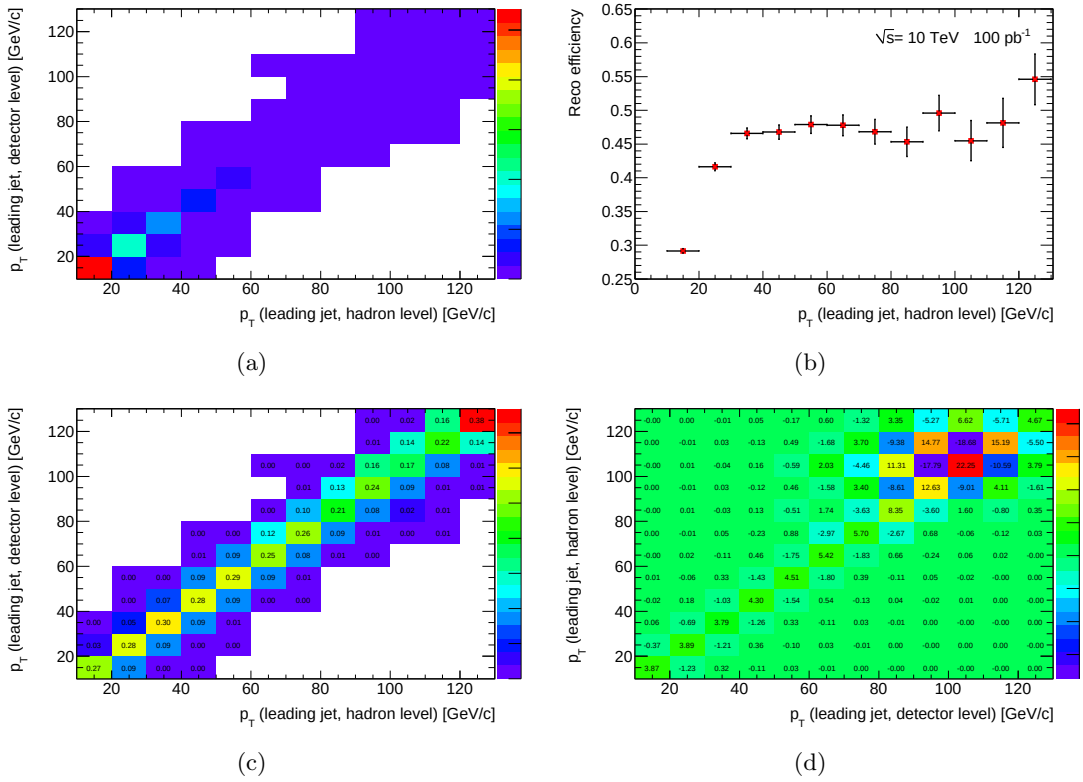

Figure 10.25: The migration matrix (a), the jet reconstruction efficiency (b), the normalized correction matrix (c) and the inverse normalized correction matrix (d) for the leading jet depending on p_T

Due to the low statistics for high p_T, the inverse matrix shows fluctuations between negative and positive values.

For the η of the leading jet, the matrix M_{ij} is divided into 10 bins with a width of 0.96 for $-4.8 < \eta < 4.8$. Fig. 10.26(b) shows the jet reconstruction efficiency as a function of η for this binning and Fig. 10.26(c) shows the resulting normalized matrix. From that the inverse matrix is calculated (see Fig. 10.26(d)).

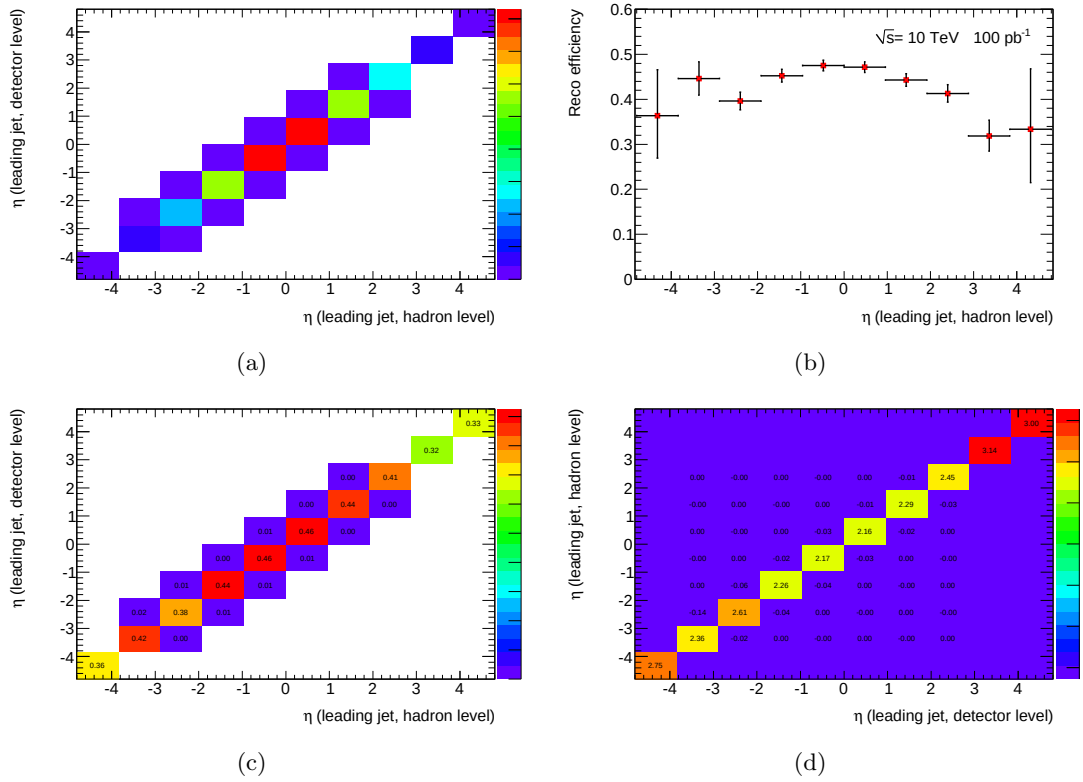

Figure 10.26: Jet reconstruction efficiency (b), the normalized correction matrix (c) for the leading jet depending on η

In order to do the correction in a more correct way, taken the correlation between p_T and η into account, the p_T binning has to be done for different η regions. Thus, the migration of p_T in different detector regions and the migration in η is taken into account. The migration in η is very low, see Fig. 10.26(c), therefore a lot of additional bins in η are needed. For the current statistic already a separation in central and forward region causes problems in the matrix inversion.

Comparison of Distribution with and without Corrections

Fig. 10.27 shows the p_T distributions for the leading and the second leading jet with and without corrections compared to the truth distribution. The corrections are applied on a test sample corresponding to an integrated luminosity of 100 pb^{-1}, which is statistically independent of the training sample. In addition the relative residuals between the corrected and the truth distribution are shown.

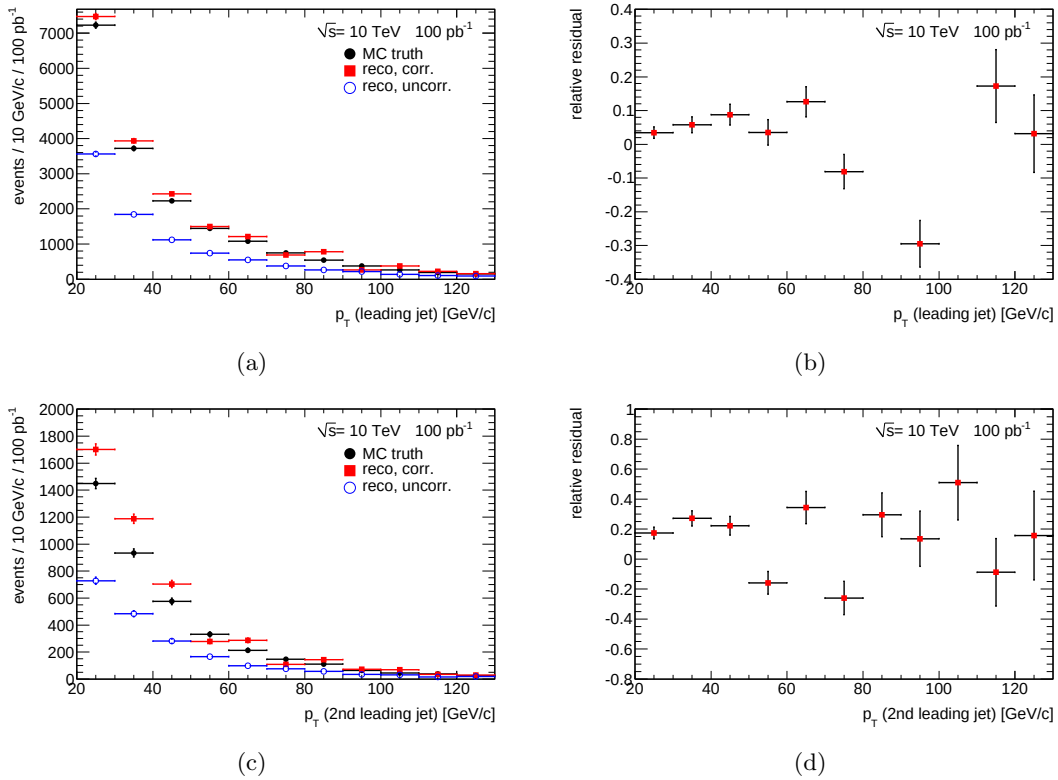

Figure 10.27: Comparison of the truth distribution with the corrected and the uncorrected reconstructed distributions of the transverse momentum of the leading jet (a) with the corresponding relative residual (b) and the second leading jet (c) with its corresponding relative residual (d).

The fluctuations seen in Fig. 10.25(d) are reflected in the relative residuals, increasing for the second leading jet. These fluctuations are typical for this method in regions of low statistics. Similar effects were obtained in studies at the Tevatron [58]. For regions with high statistics the method seems to be very precise, but due to the fluctuations in low statistics regions, there is no adequate result for the detector correction. In the following no further studies for this method are done, but probably it can be a good alternative with more statistics. There is also the possibility to use regularisation to improve this method [59, 60].

10.3.4 Iterative (Bayes) Method

The iterative Bayes method [61], which is implemented in the ROOT software package RooUnfold [62], is in the beginning comparable to the matrix method. It uses the same migration matrix. The method uses the matrix and two training distributions as an input. The training distributions are the measured M_j and the truth T_i. The matrix contains the fraction R_{ji} of events T_i which end up in M_j. Instead of inverting the matrix, this method uses the Bayes theorem, to recalculate an improved truth distribution μ_i from the measured distribution n_j with previous truth assumptions using Eq. 10.4.

$$\hat{\mu}_i = \frac{1}{\epsilon_i} \sum_{j=1}^{N} \frac{R_{ji} p_i}{\sum_k R_{jk} p_k} n_j, \tag{10.4}$$

where ϵ_i describes the efficiency and p_i the probability.

These calculations are done iteratively. The number of iterations has to be set in the beginning as an additional input parameter. The iteration is done to avoid statistical fluctuations as seen in Sect. 10.3.3 for the matrix inversion.

Fig. 10.28 shows the input distributions for this method using the p_T of the leading jet as an example.

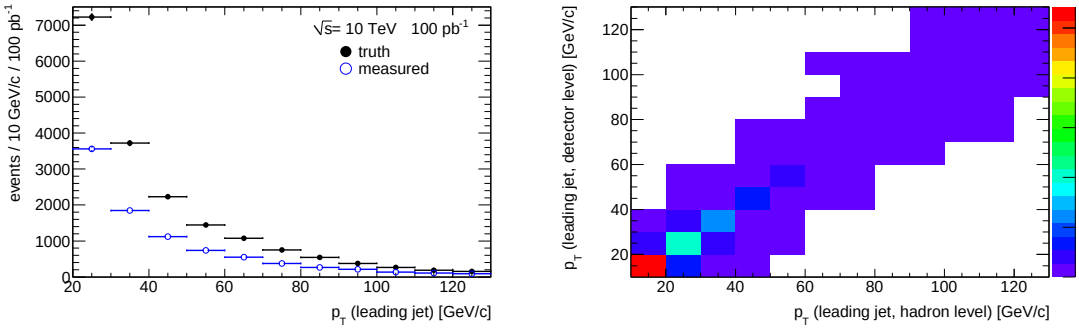

(a) (b)

Figure 10.28: Trainings distributions (true and measured) (a) and the response matrix (b) for the p_T of the leading jet.

The number of iterations is set to 4. Additional iterations yield no visible improvement. The next section shows the comparison between the corrected, the uncorrected and the truth distribution.

Comparison of Distribution with and without Corrections

Fig. 10.29 shows the comparison of the truth distribution with the corrected and uncorrected reconstructed distribution for the p_T of the leading and second leading jet. In addition the relative residuals are shown. As with the other methods, the correction is applied on a test sample, which is statistically independent from the training samples.

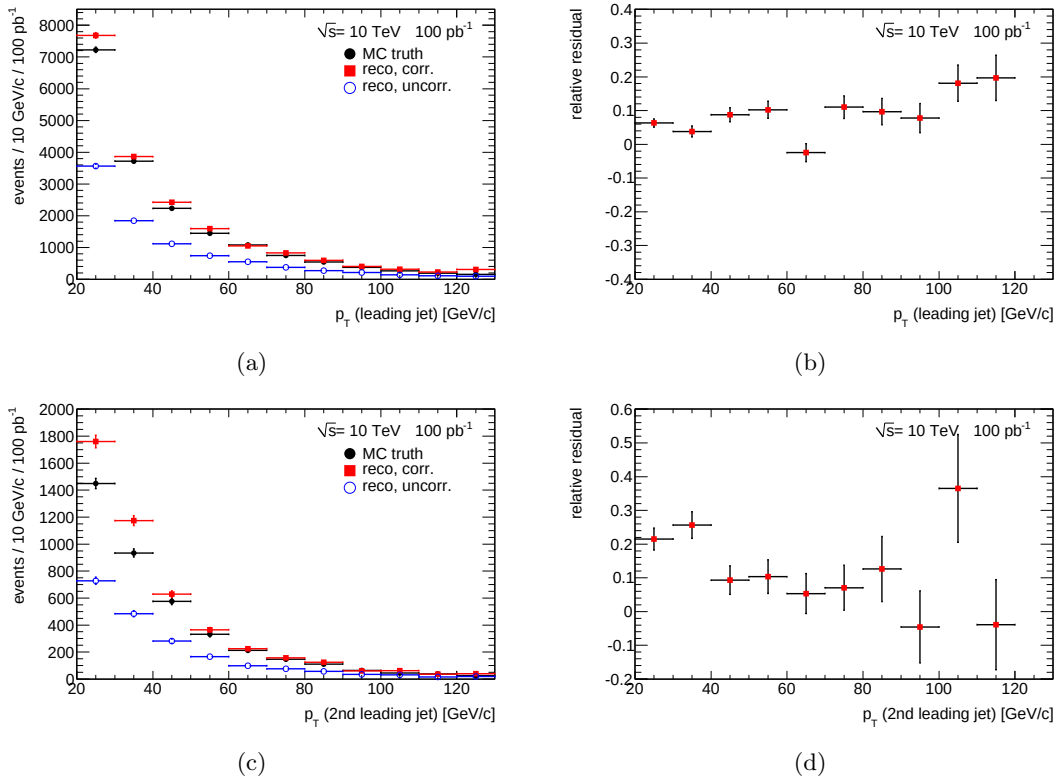

Figure 10.29: Comparison of the truth distribution with the corrected and the uncorrected reconstructed distributions of the transverse momentum of the leading jet (a) with the corresponding relative residual (b) and the second leading jet (c) with its corresponding relative residual (d).

The relative residual shows a bias of 10%. This difference does not belong to the method itself, it is related to the combinatorial jet background, which is not taken into account in the training. In order to avoid such effects the reconstructed distribution has to be corrected first for fake jets. This can be done using for example a simple bin-by-bin correction. Afterwards, the distribution is corrected for detector effects. The problem of fake jets is also present in the two previous methods. Looking at the second leading jet, there is an over correction between 20 GeV/c and 40 GeV/c, which probably refers to the generator cut for jets at 10 GeV/c. The migration of jets with a p_T below 10 GeV/c are not taken into account.

10.3.5 Bin-by-Bin Method

The bin-by-bin method is the method currently used at Tevatron [58]. It is the most intuitive method and is implemented in RooUnfold. For the bin-by-bin method it is assumed, that the migration between the bins is negligible and therefore the migration matrix is diagonal. This assumption is only valid, if the purity of each bin is very high, e.g. the bin size has to be greater than the resolution. The bin-by-bin method only needs the measured distribution and the truth distribution as an input to calculate the correction factor for each bin. A problem with the bin-by-bin method is the high shape dependence in case of non-negligible migration, therefore the shape of the observable in the Monte Carlo used for the training has to be similar to the shape in the data. On the other hand this method does not need to differentiate between real

and fake jets, since the fake jets are automatically included in the training.

Fig. 10.30 shows the measured and the truth distribution for the p_T of the leading jet as an example for the input distributions.

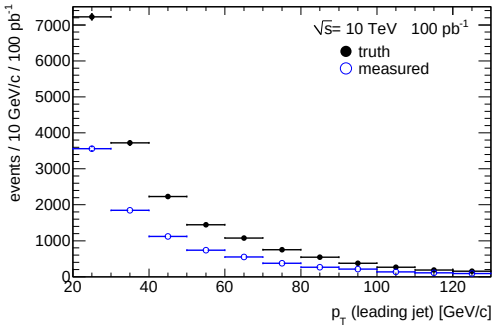

Figure 10.30: Training distributions for the p_T of the leading jet.

Comparison of Distribution with and without Corrections

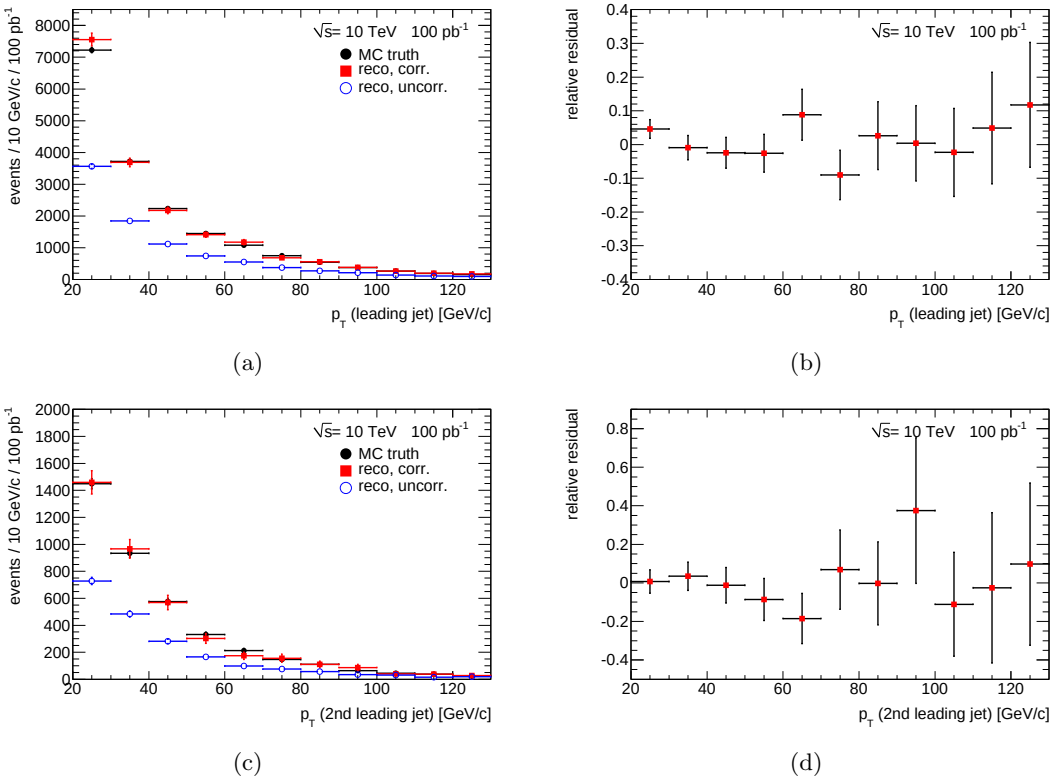

Figure 10.31: Comparison of the truth distribution with the corrected and the uncorrected reconstructed distributions of the transverse momentum of the leading jet (a) with the corresponding relative residual (b) and the second leading jet (c) with its corresponding relative residual (d).

Fig. 10.31(a) and Fig. 10.31(c) show the comparison of the truth distribution with the corrected and uncorrected reconstructed distribution for the p_T of the leading and second leading jet. In addition Fig. 10.31(b) and Fig. 10.31(d) show the relative residuals. The correction is applied on a test sample, which is statistically independent from the training samples.

The relative residuals show a good agreement between the corrected and the truth distributions, the precision is within 5% for high statistical regions. For high p_T the method is dominated by statistical fluctuations from the training samples. In order to get the best result from this method, the purity of each bin has to be checked and probably the binning has to be adapted.

10.4 Uncertainties

In this section, the different sources of uncertainties on the measurement of the inclusive and differential jet cross section in $Z \rightarrow e^+e^-$ events in data are determined. The calculation of the error is exemplary shown for the inclusive cross section and the differential cross section as a function of the transverse momentum of the leading jet. On detector level statistical uncertainties and uncertainties from the background estimation have to be taken into account. For the correction from detector level to hadron level uncertainties coming from the Jet Energy Scale (JES) uncertainty and the correction method (such as statistics, bias, shape dependence, resolution) have to be taken into account.

10.4.1 Statistical Uncertainties

For data statistical fluctuations have an impact on the cross section measurement. The size of the uncertainty depends on the available integrated luminosity. For the first year of data taking $100 - 200$ pb^{-1} are expected. In order to determine the statistical uncertainties for this luminosity, a MC set with the exact number of events which are expected for 100 pb^{-1} is used. A more reliable estimate of the uncertainty is achieved by performing two independent pseudo experiments. For the inclusive cross section of $Z(\rightarrow e^+e^-) + 1 - 3$ *jets* the statistical uncertainty is between $1\% - 4\%$, for the differential cross section depending on p_T of the leading jet the uncertainty is 1.7% for 20 GeV/c $\leq p_T <$ 30 GeV/c and 10.4% for 120 GeV/c $\leq p_T <$ 130 GeV/c.

10.4.2 Systematic Uncertainties

In this subsection the different source of systematic uncertainties are described. First the uncertainties coming from the background estimation are described. Afterwards the different uncertainties due to correction for detector effects are explained and finally the uncertainties which result from the error on the JES are shown.

Uncertainties from Background

As seen in Sect. 10.2 the backgrounds from $W \rightarrow e\nu$ and $Z \rightarrow \tau^+\tau^-$ are negligible. The QCD background is assumed to be estimated from data with a precision of better than 20% using side band fits, see Sect. 10.2.2. The precision for the modelling of the $t\bar{t}$ background is assumed to be better, since the jets stem directly from the NLO matrix element such that the cross section can be predicted with a larger precision. In addition, the $t\bar{t}$ cross section will be measured with a reasonable precision in the first data [63]. For the following analysis a precision of 10% is applied. The real precision has to be taken from data. A first estimate of the uncertainty from the background is given by calculating the quadratical sum of the uncertainties from the different

backgrounds. For the inclusive cross section of $Z(\rightarrow e^+e^-)+ \geq 1\ jet$ to $Z(\rightarrow e^+e^-)+ \geq 3\ jets$, the total uncertainty from the background is between $0.1\% - 0.4\%$. For the differential cross section depending on p_T of the leading jet the uncertainty is about 0.25% over the whole range.

Uncertainties from the Corrections for Detector Effects

The different sources of uncertainties from the corrections for detector effects are discussed in the following. The errors are exemplary derived for the factorized corrections. A similar procedure is performed for the other methods. In order to be independent from statistical fluctuations in the determination of the systematic uncertainties the full statistics of the different Monte Carlo samples are used. It is assumed that the bias from statistical fluctuations is much higher than the bias coming from the fact that training and test sample are statistically dependent.

The observable bias of the different methods is not discussed in case of uncertainties. These differences mostly do not refer to a bias of the method, they can be ascribed to some facts, e.g. combinatorial background or the purity of the bins. In order to determine the additional uncertainty coming from the real bias of the methods, these facts have to be taken into account.

Uncertainties from the Method Due to statistical fluctuations in the training samples of the different methods, a systematic uncertainty on the different methods is introduced. For the factorized corrections this uncertainty is determined by varying the different correction distributions within their errors. It is assumed that the different uncertainties are independent from each other. Therefore, the variation is done for each correction distribution separately and the total uncertainty is determined from the square root of the quadratic sum of them. For the inverse Bayes method and the bin-by-bin method the uncertainty is determined by the RooUnfold software [62]. The uncertainty from the Bayes method is small compared to the uncertainties from the factorized corrections and the bin-by-bin method. A further improvement can be achieved by using the error computation recommended by G. D'Agostini [61].

Mismeasurement of the Resolution Due to the fact that the jet resolution measurement is not perfect, an additional uncertainty on the correction for detector effects from the mismeasurement of the resolution is introduced. Conservatively, a mismeasurement of $\pm 50\%$ is assumed to derive the uncertainty. The extraction of the errors is done by varying the jet resolution within the mismeasurement and propagating it into the correction. Later, the uncertainty on the jet resolution measurement is taken from data.

In spite of the extreme assumption for the mismeasurement of the jet resolution, the uncertainty on the inclusive cross section for $Z(\rightarrow e^+e^-)+ \geq 1-3\ jets$ is still between 1% and 3% for the factorized correction. The uncertainty on the differential cross section depending on p_T of the leading jet varies also between 1% and 3% for the factorized correction. The uncertainties for the other methods are expected to be at the same order of magnitude.

Shape Dependence An additional systematic uncertainty on the correction for detector effects is introduced due to the uncertainty of the shape. This uncertainty highly depends on the method which is used for the correction of detector effects. Unfolding methods as the matrix inversion are shape independent contrary to the bin-by-bin method, which is highly shape dependent. In order to get an estimate for the shape dependence and the corresponding uncertainty, the correction is derived from the predictions of different Monte Carlo generators and applied on the test sample. In the following the predictions from PYTHIA and ALPGEN are used for the

training and for the test sample ALPGEN is used. As described in Sect. 8.1, PYTHIA predicts a softer p_T spectrum compared to ALPGEN.

Fig. 10.32 shows the comparison between the corrected distributions for the factorized correction; one corrected with corrections derived from PYTHIA and one corrected with corrections derived from ALPGEN. The error bands describe the systematic uncertainty of the correction method coming from statistical fluctuations in the training samples and the statistical uncertainty of the test sample. Apart from the first bin a small bias to lower values of the residual is visible between the distribution corrected with ALPGEN and the distribution corrected with PYTHIA. However, this bias is small compared to the other systematic uncertainty of the factorized method. The small shape dependence results in a systematic uncertainty at the percentage level.

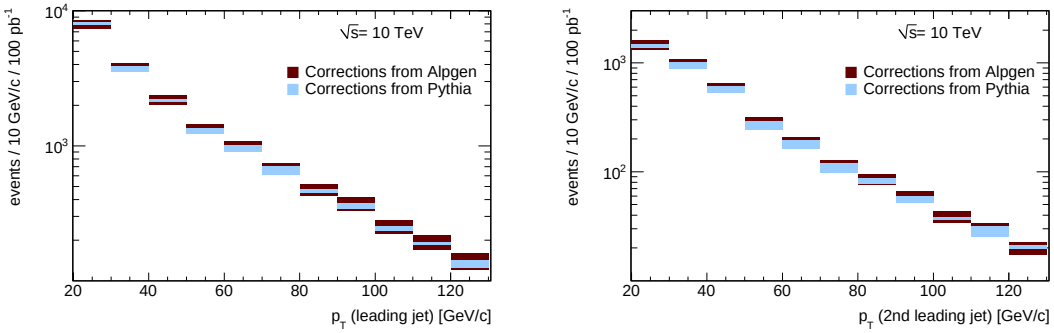

(a) (b)

Figure 10.32: Corrected reconstructed distributions of the transverse momentum once with ALPGEN and once with PYTHIA of the leading jet (a) and the second leading jet (b).

Combined Uncertainty of the Correction for Detector Effects In the following, the combination of the different uncertainties of the correction for detector effects is discussed. Fig. 10.33 shows the relative uncertainties for the different contributions to the combined uncertainty of the factorized correction method.

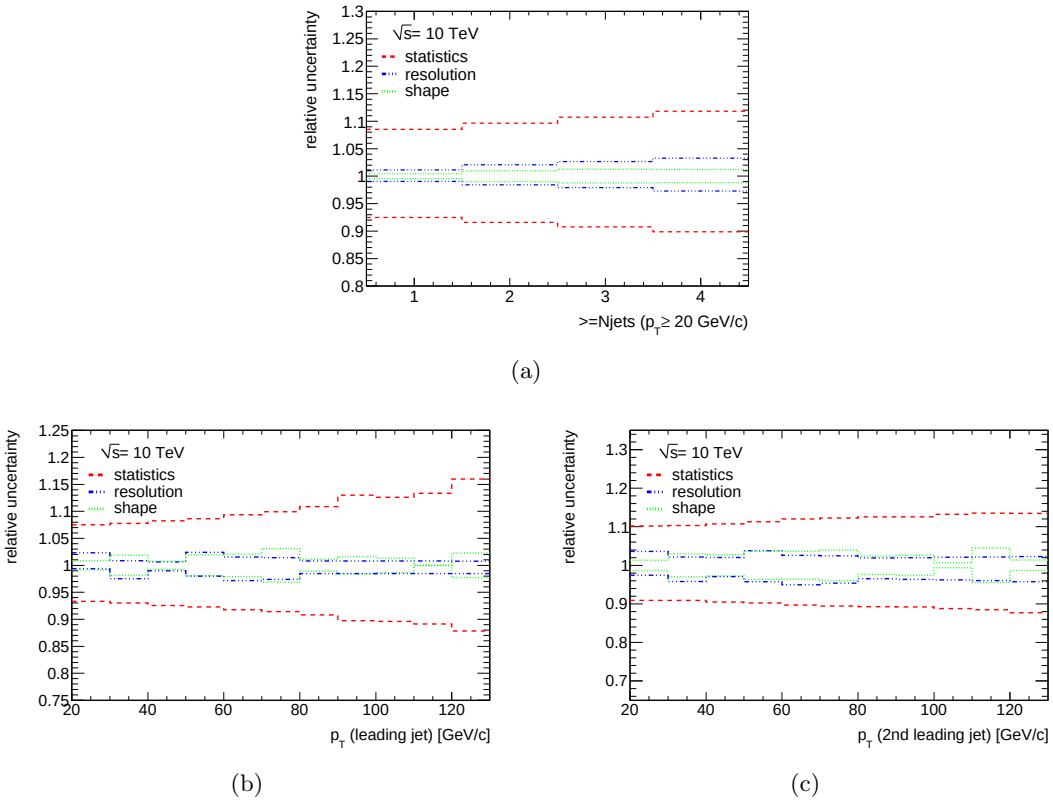

Figure 10.33: Different contributions to the combined relative uncertainty from various factorized corrections for inclusive cross section (a), the differential cross section depending on p_T of the leading jet (b) and the differential cross section depending on p_T of the second leading jet (c).

Fig. 10.33(a) shows the contributions of the combined relative uncertainty for the inclusive $Z(\rightarrow e^+e^-) + \ jets$ cross section and Fig. 10.33(b) and 10.33(c) shows the contributions for the differential cross section depending on p_T of the leading and the second leading jet. The combined uncertainty of the method is clearly dominated by the statistical fluctuations of the training samples. The uncertainties coming from the mismeasurement of the jet resolution and the shape dependence of this method are quite small. However, the uncertainty coming from the statistical fluctuations is not a limiting factor of the combined uncertainty for the correction of detector effects. It can be decreased by generating much more Monte Carlo events for the training samples. The uncertainty from the mismeasurement of the jet resolution is limited by the detector, but the uncertainty shown in Fig. 10.33 is determined for an extreme assumption. Therefore, this uncertainty will be smaller using the real uncertainty on the jet resolution, which has to be determined from data. In order to minimize the shape dependence, the distributions predicted from the Monte Carlo have to be very close to the real distributions from data.

The size of the different contributions to the combined uncertainty is expected to look quite the same for all methods except for the contribution from the shape dependence. As discussed

before the shape dependence is expected to vary for the different methods.

JES

For the beginning of data taking ATLAS expects a JES uncertainty of 10%, later probably down to 5% and eventually reaching 1%. In the following, three different benchmark scenarios are shown by propagating positive and negative shifts of the JES uncertainty of 1%, 5% or 10% into the measured cross section. Fig. 10.34 presents the absolute uncertainty for the inclusive cross section (a) and the p_T of the leading jet (b) for the factorized corrections.

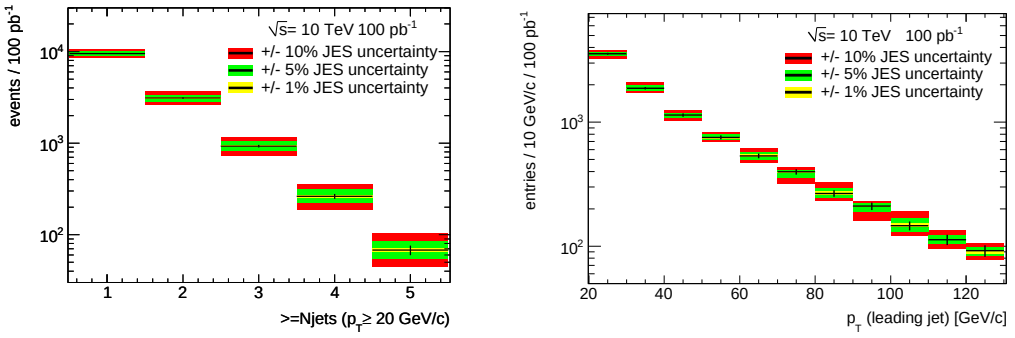

(a) (b)

Figure 10.34: Distributions for absolute uncertainty from the JES uncertainty on the inclusive cross section (a) and the p_T of the leading jet. The errors are derived for JES uncertainties of 1%, 5% and 10%.

In order to get a better feeling of the impact of these uncertainties, Fig. 10.35 shows the relative uncertainty for the inclusive cross section (a) and the p_T of the leading jet (b).

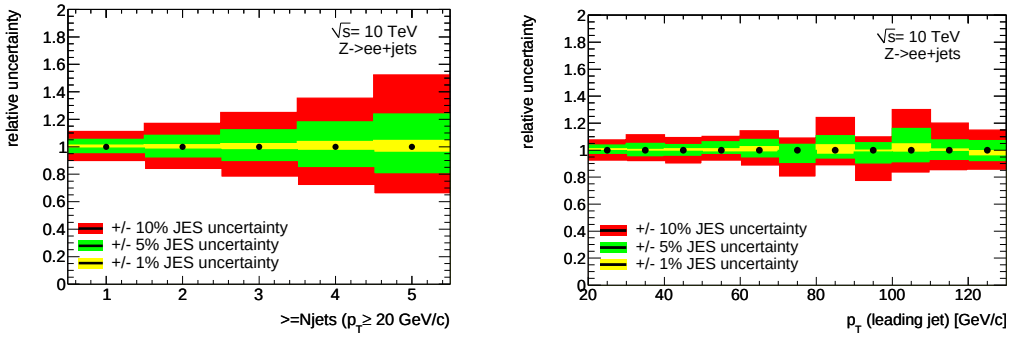

(a) (b)

Figure 10.35: Distributions for absolute uncertainty from the JES uncertainty on the inclusive cross section (a) and the p_T of the leading jet (b). The errors are derived for JES uncertainties of 1%, 5% and 10%. The shown uncertainties are for the factorized corrections.

As expected, the uncertainty on the inclusive cross section increases with increasing number of jets. For $Z(\rightarrow e^+e^-)+ \geq 1-3\ jets$ the uncertainty is $6\% - 12\%$ for a JES uncertainty of 5% and $13\% - 25\%$ for a JES uncertainty of 10%. For the differential cross section depending on p_T of the leading jet, the uncertainty varies between 4% and 17% for a JES uncertainty of 5% and between 8% and 31% for a JES uncertainty of 10%. The uncertainties from JES uncertainty for the other correction methods are expected to be at the same order of magnitude by reason of the fact that all methods use MC events for training.

10.4.3 Total Uncertainty

Tab. 10.3 and Tab. 10.4 summarize all uncertainties of the $Z \rightarrow ee+\ jets$ cross section measurement from detector to hadron level and shows the order of magnitude for some examples. The table only includes the uncertainties from the factorized corrections. But the uncertainties from the bin-by-bin and the Bayes method, due to the JES uncertainty or resolution effects, are expected to be at the same order of magnitude. The uncertainty due to statistical fluctuations in the training sample is lower for the Bayes method and higher for the bin-by-bin method compared to the factorized corrections. Concerning the shape dependence the Bayes method is expected to be independent and the shape dependence of the bin-by-bin method depends on the migration in the particular case.

Uncertainty		$Z+ \geq 1\ jet$	$Z+ \geq 2\ jets$	$Z+ \geq 3\ jets$
statistics		$\pm 1.03\%$	$\pm 1.80\%$	$\pm 3.32\%$
background		$\pm 0.15\%$	$\pm 0.25\%$	$\pm 0.38\%$
Uncertainties for detector correction				
statistics		$(+8.50/-7.51)\%$	$(+9.64/-8.41)\%$	$(+10.71/-9.23)\%$
shape dependence		$\pm 0.44\%$	$\pm 0.98\%$	$\pm 1.25\%$
resolution	$\pm 50\%$	$(+1.15/-0.97)\%$	$(+2.06/-1.60)\%$	$(+2.66/-2.10)\%$
JES	5%	$(+5.40/-5.17)\%$	$(+8.33/-8.35)\%$	$(+12.39/-10.88)\%$
	10%	$(+11.10/-10.87)\%$	$(+17.02/-16.69)\%$	$(+24.94/-22.29)\%$
total uncertainty	JES 5%	$(+10.20/-9.24)\%$	$(+13.07/-12.14)\%$	$(+16.97/-14.86)\%$
	JES 10%	$(+14.07/-13.30)\%$	$(+19.78/-18.87)\%$	$(+27.5/-24.48)\%$

Table 10.3: Total uncertainty on the inclusive $Z \rightarrow ee+ \geq 1-3\ jets$ cross section.

Adding all uncertainties quadratically results in a total uncertainty on the inclusive $Z(\rightarrow e^+e^-)+ \geq 1-3\ jets$ between 5.4% and 12.4% for a JES uncertainty of 5% and between 11.1% and 25% for a JES uncertainty of 10%.

Uncertainty		20 **GeV/c** $\leq p_T <$ 30 **GeV/c**	110 **GeV/c** $\leq p_T <$ 120 **GeV/c**
statistics		$\pm$1.70%	$\pm$10.00%
background		$\pm$0.10%	$\pm$0.24%
Uncertainties for detector correction			
statistics		$(+7.50/-6.69)$%	$(+13.36/-10.89)$%
shape dependence		$\pm$0.85%	$\pm$0.04%
resolution	$\pm$50%	$(+2.33/-0.63)$%	$(+0.78/-1.54)$%
JES	5%	$(+3.79/-3.39)$%	$(+7.53/-7.87)$%
	10%	$(+7.61/-8.43)$%	$(+20.04/-15.42)$%
total uncertainty	JES 5%	$(+8.93/-7.76)$%	$(+18.33/-16.82)$%
	JES 10%	$(+11.10/-10.95)$%	$(+26.09/-21.42)$%

Table 10.4: Total uncertainty on the differential $Z(\rightarrow e^+e^-) + \ jets$ cross section depending on p_T of the leading jet for two example bins.

For the differential $Z(\rightarrow e^+e^-) + \ jets$ cross section depending on the p_T of the leading jet the total uncertainty is increasing from 3.8% for low p_T to 7.9% for high p_T for a JES uncertainty of 5% and from 8.5% for low p_T to 20.1% for high p_T for a JES uncertainty of 10%.

11 Results

Finally, in this chapter the results from the previous chapters 9 and 10 are discussed. First the different methods for detector corrections are compared. Afterwards, the uncertainties on the ratio between the measured cross section corrected to the hadron level and the theoretical cross section corrected to the hadron level are calculated. Both statistical and systematic uncertainties are included. Finally, the statistical and systematic limitations of the measurement are compared to the differences between the MC generator predictions. The results are discussed for a luminosity of 100 pb^{-1}.

11.1 Comparison of the Different Methods for Correction of Detector Effects

In this section, the comparison of the different methods for the correction of detector effects, described in Sect. 10.3 excluding the matrix inversion, is done.

Fig. 11.1 shows the direct comparison of the relative residuals of the different correction methods for the p_T of the leading jet (a) and the second leading jet (b). The plots only include the uncertainties due to the statistical fluctuations of the training and test sample. Here, the training and the test sample are two statistically independent samples of 100 pb^{-1}.

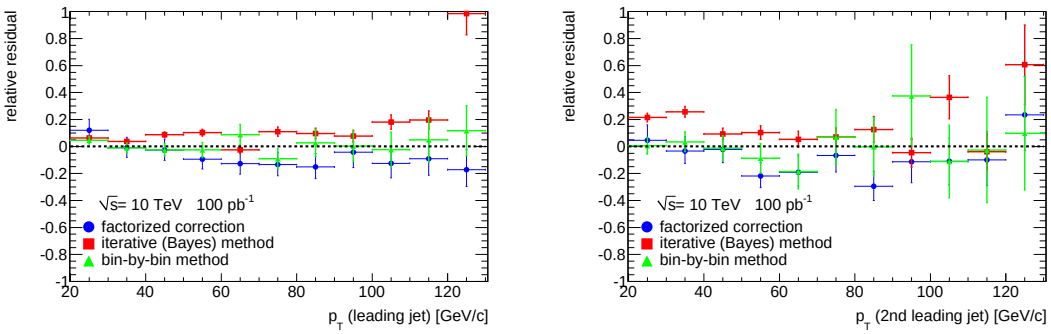

(a) (b)

Figure 11.1: Comparison of the relative residuals for the different correction methods for p_T of the leading jet (a) and p_T of the second leading jet.

For the p_T of the leading jet and the second leading jet, the bin-by-bin method gives a good agreement between the reconstructed corrected distribution and the truth distribution, except for the high p_T region of the second leading jet. This is dominated by statistical fluctuations. However, both other methods are within a precision of 5%−20% for the leading jet and 10%−30% for the second leading jet. As described in Sect. 10.3, these differences mostly do not refer to a bias in the methods. In order to make a complete comparison, the correction methods have to be fine tuned in order to reduce the biases.

The iterative Bayes method gives the smallest uncertainties due to statistical fluctuations in the training and test sample. However, this method seems to have problems with border effects in particular in the low p_T bins. By contrast the bin-by-bin methods seems to be highly dependent on statistical fluctuations, the uncertainties are twice as large compared to the other methods.

A shape independence is expected for the iterative Bayes method. The factorized correction are nearly shape independent, as shown in Sect. 10.4.2, The shape dependence is at the percent level, which is relatively low to the uncertainty due to statistical fluctuations. For the bin-by-by method a shape dependence is expected, due to migration. In order to get an estimate for the influence of this dependence, corrections with very opposed predictions for the distributions have to be done.

Summing up, all methods have their advantages and disadvantages. They have to be compared with more statistics after fine tuning the procedure to get rid of the biases. In addition, there are also some optimization possibilities for the different methods, such as using the bin-by-bin method iteratively to provide large statistical fluctuations or taking into account distributions of the entries in each bin for the factorized correction. With higher statistics also the matrix inversion could be a good alternative to the other methods, which can be obtained using regularisation.

11.2 Cross Section Ratio between Data and Theory

In this section, the results from the uncertainty studies on the $Z(\rightarrow e^+e^-) + \ jets$ cross section measurement from chapter 9 and 10 are discussed. The cross section ratio between data and theory is set to 1.

Fig. 11.2 shows the uncertainty on the cross section ratio including all statistical and systematic uncertainties for the inclusive cross section. The blue band includes the uncertainty on the theory predictions and the uncertainty of the correction from parton level to hadron level (see Sect. 9.2). The yellow band shows the uncertainty on the cross section measurement in data (see Sect. 10.4) without the uncertainties from the JES uncertainty. Finally, the green and red bands describes the impact of the JES uncertainty, green for a JES uncertainty of 5% and red for a JES uncertainty of 10%.

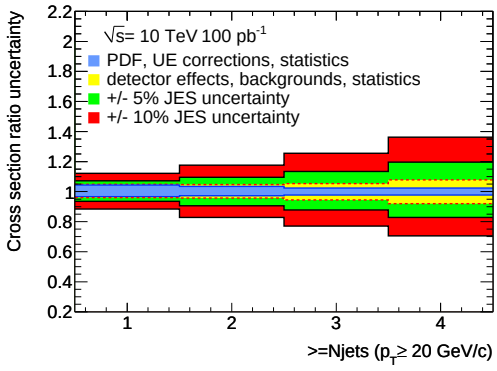

Figure 11.2: Total uncertainty on the measurement of the cross section ratio between data and theory for $Z \rightarrow e^+e^-$ inclusive cross section with 100 pb^{-1}. The ratio is set to one.

The dominant contribution comes from the uncertainty of the JES, it is 6%−12% (13%−25%) for $Z(\rightarrow e^+e^-)+ \geq 1-3\ jets$ for a JES uncertainty of 5% (10%). Tab. 11.1 shows a summary of the different sources of statistical and systematic uncertainties for the inclusive $Z(\rightarrow e^+e^-)+ \geq 1-3\ jets$ cross section. Regarding the correction of detector effects only the uncertainties for the factorized corrections are shown.

For the uncertainty coming from the background estimation, it is assumed that $W \rightarrow e\nu$ and $Z \rightarrow \tau^+\tau^-$ are negligible compared to QCD jets and $t\bar{t}$. For the QCD jets background a precision of 20% and for $t\bar{t}$ a precision of 10% for the estimation is assumed, which results in an uncertainty of less than 0.5% on the inclusive $Z(\rightarrow e^+e^-)+ \geq 1-3\ jets$ cross section. Hence, uncertainties from the background do not contribute much to the total uncertainty.

As described in Sect. 10.4.2, the uncertainty for the correction of detector effects is clearly dominated by the uncertainty of the statistical fluctuations in the training samples, which is at same order as the uncertainty from the JES of 5%, but can be reduced using a higher amount of statistics.

The uncertainty due to statistical fluctuations in data becomes more and more important for high jet multiplicities. It increases for the inclusive $Z(\rightarrow e^+e^-)+ \geq 1-3\ jets$ cross section from 1% to 4%. The uncertainty from the theory predictions has a small decrease with increasing jet multiplicity from 4.5% to 2.5%. This uncertainty is dominated by the contribution from PDFs, but it could be possible that the contribution from UE becomes larger due to the uncertainty on the UE measurement in data and the UE tuning of PYTHIA.

For the first data, including an uncertainty on the estimation of the integrated luminosity is not necessary, due to the fact that theory predictions and measurements from data will be normalized to the inclusive $Z \rightarrow e^+e^-$ cross section. In addition, due to the fact that the reconstruction efficiency is constant with increasing number of jets, the uncertainty belonging to the electron corrections within the factorized correction can be neglected, which results in a smaller contribution for the uncertainty from the correction method due to statistical fluctuations in the training sample.

Uncertainty		$Z+ \geq 1$ *jet*	$Z+ \geq 2$ *jets*	$Z+ \geq 3$ *jets*
Uncertainties from parton to hadron level				
statistics		$\pm 0.19\%$	$\pm 0.49\%$	$\pm 0.16\%$
PDF		$(+4.41/-3.35)\%$	$(+3.17/-2.29)\%$	$(+1.90/-1.83)\%$
UE corrections		$\pm 0.70\%$	$\pm 1.46\%$	$\pm 1.46\%$
Uncertainties from detector to hadron level				
statistics		$\pm 1.03\%$	$\pm 1.80\%$	$\pm 3.32\%$
background		$\pm 0.15\%$	$\pm 0.25\%$	$\pm 0.38\%$
Uncertainties for detector correction				
statistics		$(+0.73/-1.31)\%$	$(+1.18/-2.15)\%$	$(+1.59/-2.76)\%$
resolution	$\pm 50\%$	$(+1.15/-0.97)\%$	$(+2.06/-1.60)\%$	$(+2.66/-2.10)\%$
shape dependence		$\pm 0.44\%$	$\pm 0.98\%$	$\pm 1.25\%$
JES	5%	$(+5.40/-5.17)\%$	$(+8.33/-8.35)\%$	$(+12.39/-10.88)\%$
	10%	$(+11.10/-10.87)\%$	$(+17.02/-16.69)\%$	$(+24.94/-22.29)\%$
total uncertainty	JES 5%	$(+7.23/-6.52)\%$	$(+9.58/-9.42)\%$	$(+13.48/-12.19)\%$
	JES 10%	$(+12.09/-11.57)\%$	$(+17.66/-17.25)\%$	$(+25.50/-22.96)\%$

Table 11.1: Different contributions to the total uncertainty on the inclusive $Z(\rightarrow e^+e^-)+ \geq 1-3$ *jets* cross section. The uncertainties for the correction of detector effects refers to the factorized correction.

The total uncertainty on the ratio between data and theory for the inclusive $Z(\rightarrow e^+e^-) + 1-3$ *jets* is between 7.3% and 13.5% for a JES of 5% and between 12.1% and 25.5% for a JES of 10%.

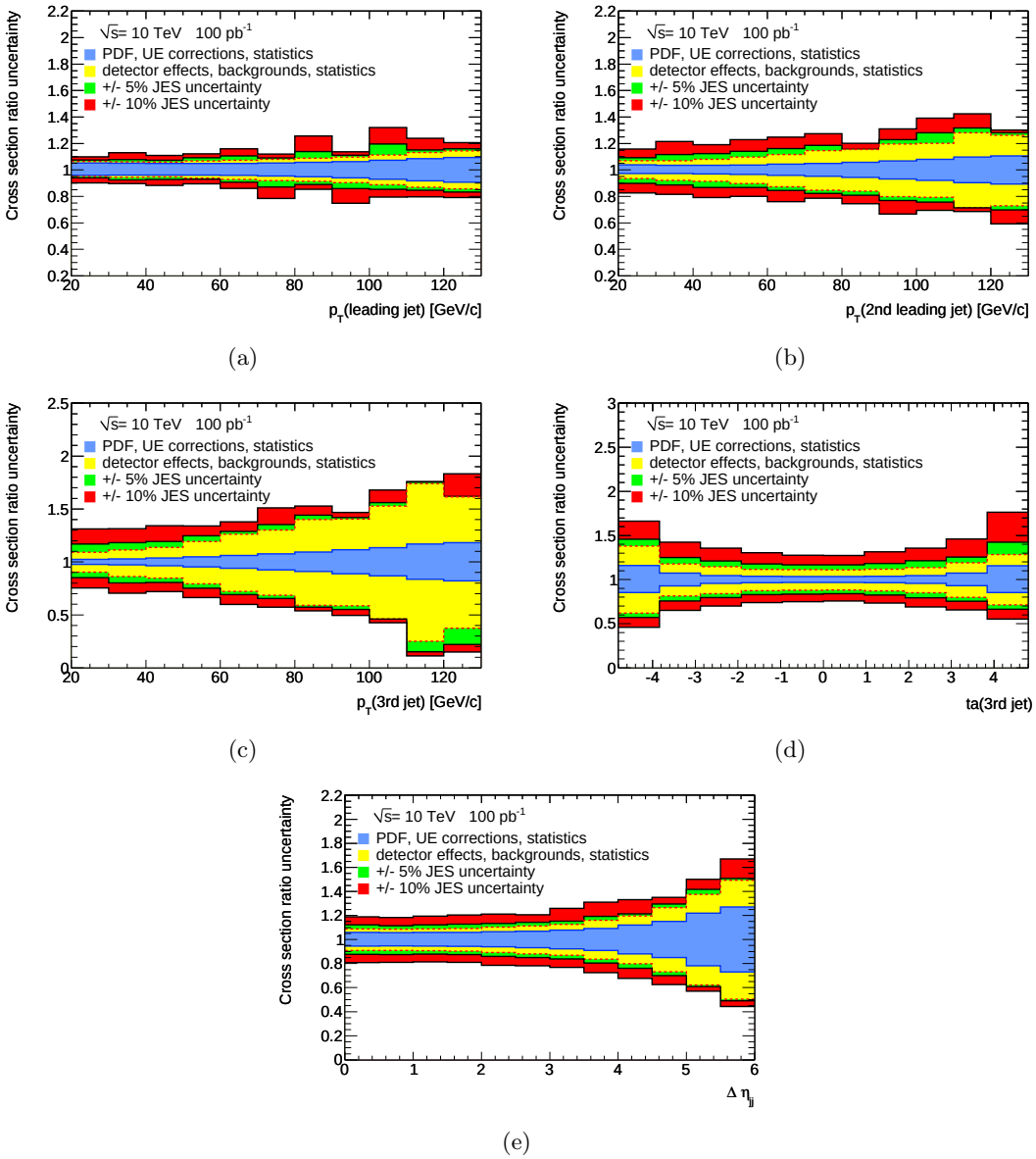

Figure 11.3: Total uncertainties on the differential cross section depending on p_T of the leading (a), second leading jet (b), third jet (c), η of the third jet (d) and the pseudorapidity gap (e).

Fig. 11.3 shows the total uncertainty for the differential $Z(\rightarrow e^+e^-) + \ jets$ cross section depending on p_T of the leading (a), the second leading jet (b) and the VBF $H \rightarrow \tau^+\tau^-$ key quantities (c)-(e).

As described in Sect. 9.2.3, the uncertainty from PDFs decreases with increasing p_T of the jets. In contrast, the uncertainties from statistics and UE corrections increases with increasing p_T of the jets. This results in an uncertainty on the theory, which increases with increasing p_T, for example from 5.2% to 8.5% for the leading jet. The contributions from the statistical uncertainty, the detector corrections and the JES increases as well with increasing p_T of the jets. In case of the uncertainties from the detector correction the increasing factor is the uncertainty due to the statistical fluctuations in the training sample. Again, this could be remedied by a larger

training sample. The uncertainties from resolution effects and shape dependence are nearly constant, see Sect. 10.4.2. The dominant contribution on the total uncertainty comes from the JES uncertainty, if the precision is only 10%. For a lower JES uncertainty, the contribution from the PDFs is the dominant contribution for low p_T and for high p_T the dominant contribution comes from the statistical fluctuations of the measurement.

Concerning the VBF $H \rightarrow \tau^+\tau^-$ key quantities, the precision of a cross section measurement for a sub-sample with a large pseudorapidity gap is highly limited by statistical fluctuations in the data.

Tab. 11.2 shows some examples for the different sources of uncertainties on the differential cross section measurement for the p_T of the leading jet and the pseudorapidity gap between the tagged jets. The total uncertainty on the ratio between data and theory for the differential $Z(\rightarrow e^+e^-) + \ jets$ cross section depending on the p_T of the leading jet increases with increasing p_T from 7.5% to 15.4% for a JES uncertainty of 5% and from 10% to 24% for a JES uncertainty of 10%.

Uncertainty		**Leading jet**		**Pseudorapidity gap**
		20 GeV/c $\leq p_T <$ 30 GeV/c	110 GeV/c $\leq p_T <$ 120 GeV/c	$3.0 \leq \Delta\eta < 3.5$
Uncertainties from parton to hadron level				
statistics		$\pm 0.37\%$	$\pm 2.06\%$	$\pm 2.38\%$
PDF		$(+5.05/-3.99)\%$	$(+2.81/-2.09)\%$	$(+1.97/-1.87)\%$
UE corrections		$\pm 0.91\%$	$\pm 7.71\%$	$\pm 8.55\%$
Uncertainties from detector to hadron level				
statistics		$\pm 1.70\%$	$\pm 10.00\%$	$\pm 12.40\%$
background		$\pm 0.10\%$	$\pm 0.24\%$	$\pm 0.36\%$
Uncertainties for detector correction				
statistics		$(+2.42/-1.84)\%$	$(+0.94/-1.83)\%$	$(+1.40/-3.20)\%$
resolution	$\pm 50\%$	$(+2.33/-0.63)\%$	$(+0.78/-1.54)\%$	$(+2.88/-3.77)\%$
shape dependence		$\pm 0.85\%$	$\pm 0.04\%$	$\pm 2.91\%$
JES	5%	$(+3.79/-3.39)\%$	$(+7.53/-7.87)\%$	$(+8.63/-9.43)\%$
	10%	$(+7.61/-8.43)\%$	$(+20.04/-15.42)\%$	$(+22.62/-19.14)\%$
total uncertainty	JES 5%	$(+7.47/-5.98)\%$	$(+15.16/-15.35)\%$	$(+19.19/-19.59)\%$
	JES 10%	$(+9.96/-9.76)\%$	$(+23.97/-20.29)\%$	$(+30.96/-27.65)\%$

Table 11.2: Different contributions to the total uncertainty on the measurement of the ratio between data and theory for the differential $Z(\rightarrow e^+e^-) +$ *jets* cross section. Taking some examples of the p_T of the leading jet and the pseudorapidity gap between the tagging jets.

11.3 Comparison between the Monte Carlo Generators with Respect to Uncertainties

In this section the statistical and systematic uncertainties on the inclusive and differential $Z(\rightarrow e^+e^-) + \ jets$ cross section are compared to the typical differences of Monte Carlo generators. The comparison is done on hadron level by applying the uncertainties expected in data on the predictions from the Monte Carlo generators. Due to the fact that the luminosity is not well known for the first data, the distributions are normalized to the inclusive $Z \rightarrow e^+e^-$ cross section. In addition, the comparison is done for a JES of 5% and the uncertainties for the correction of detector effects are determined from the factorized correction.
Fig. 11.4 shows the differences between the generators for the inclusive $Z(\rightarrow e^+e^-)+ \geq 1-3\ jets$ cross section.

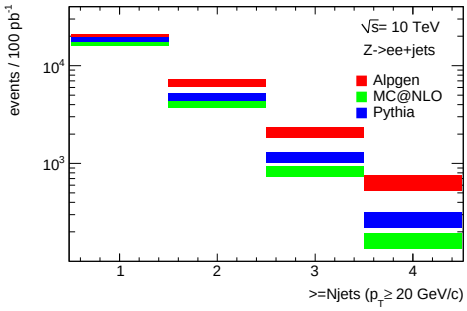

Figure 11.4: Comparison between the predictions from different Monte Carlo generators for the inclusive $Z(\rightarrow e^+e^-)+ \geq 1-3\ jets$ cross section with the uncertainties expected from data.

For the first 100 pb^{-1} of data with a JES uncertainty of 5%, it is not possible to distinguish between the generators for the inclusive $Z(\rightarrow e^+e^-)+ \geq 1\ jets$ cross section with the expected precision. For the inclusive $Z(\rightarrow e^+e^-)+ \geq 2\ jets$ cross section it is challenging to distinguish between MC@NLO and PYTHIA but between ALPGEN and MC@NLO or PYTHIA it is possible. For larger jet multiplicities, all three generators can be separated. Using different methods, which consider all bins at the time, e.g maximum likelihood fits, could provide a better result. This will be investigated in further studies. Fig. 11.5 shows the comparison for the differential

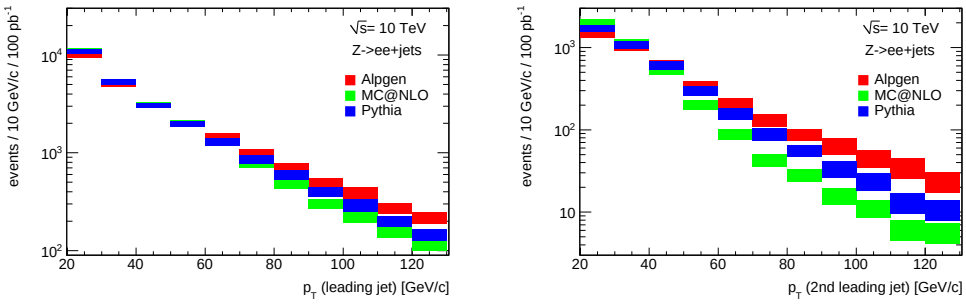

(a) (b)

Figure 11.5: Comparison between the predictions from different Monte Carlo generators for the differential $Z(\rightarrow e^+e^-) + \ jets$ cross section depending on the p_T of the leading jet (a) and second leading jet (b) with the uncertainties expected from data.

$Z(\rightarrow e^+e^-) + \ jets$ cross section depending on p_T of the leading (a) and second leading jet (b).

For the p_T of the leading jet, the predictions from the different Monte Carlo generators are comparable, only for high p_T jets a difference between the generators are visible. Therefore, it is impossible to differentiate between the generators for low p_T. For high p_T jets, the differentiation is challenging due to the low precision for generator validation. For the p_T of the second leading jet, the differentiation between the generators becomes possible for $p_T > 50$ GeV/c.

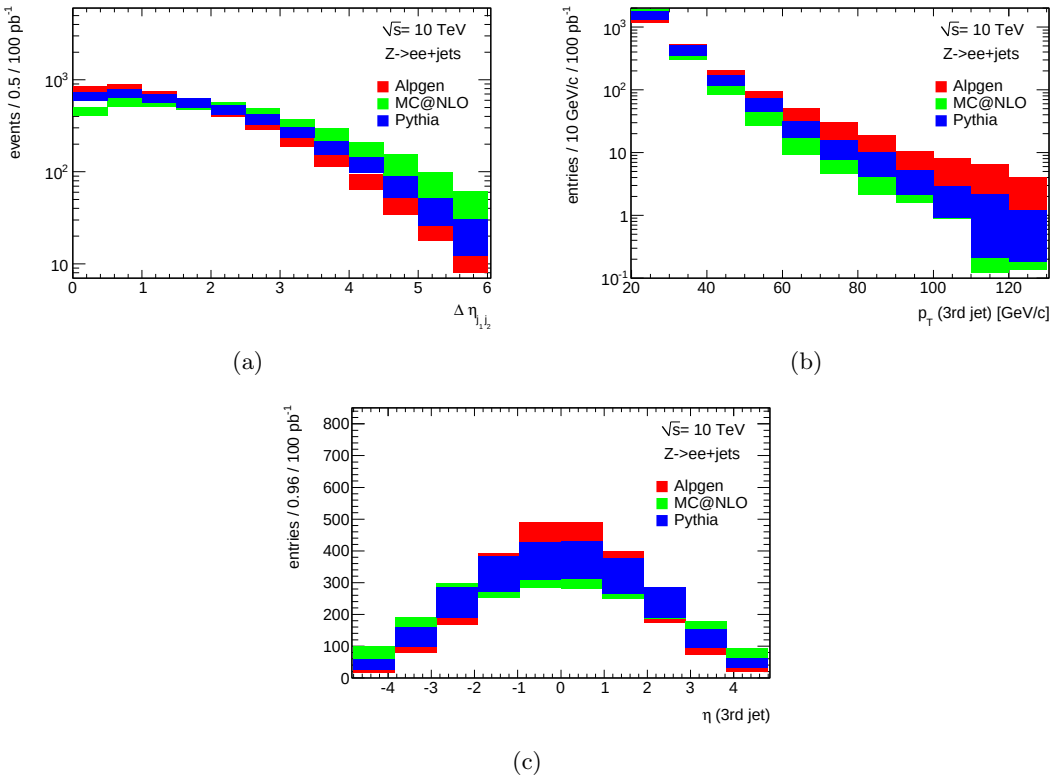

Figure 11.6: Comparison between the predictions from different Monte Carlo generators for the differential $Z(\rightarrow e^+e^-)+ \ jets$ cross section depending on the VBF $H \rightarrow \tau^+\tau^-$ key quantities: pseudorapidity gap (a), p_T of the third jet (b) and the centrality of the third jet (c).

Fig. 11.6 shows the distributions for the VBF Higgs boson key quantities. It is impossible to distinguish between the generators with the current precision for generator validation. This is due to the large uncertainties expected for the first 100 pb^{-1} of data. As described in Sect. 11.2, the expected uncertainty on the VBF Higgs boson key quantities is dominated by statistics. In order to get a prediction of the generator fitting best to the data with respect to the VBF Higgs boson key quantities, new observables have to be introduced, like e.g. the ratio between events with a large pseudorapidity gap and the events with a small pseudorapidity gap.

12 Conclusion and Outlook

12.1 Summary and Conclusion

In the first year of running, the LHC is expected to collide protons with a centre of mass energy of 7 TeV and to collect data corresponding to $100 - 200$ pb^{-1} integrated luminosity of data. This thesis describes a feasibility study for the measurement of the inclusive and differential $Z(\rightarrow e^+e^-) + jets$ cross section ratio between data and theory predictions. This study is motivated by the necessity of background estimation for the VBF Higgs boson production in tau final states.

The expectation for VBF $H \rightarrow \tau^+\tau^-$ for the first 100 pb^{-1} of data at a centre of mass energy of 10 TeV has been studied. The conclusion is that the expected number of Higgs bosons produced via vector boson fusion and decaying into a pair of tau leptons for 100 pb^{-1} is smaller than 0.04 events in the lepton-hadron channel. Therefore, the focus has been set to the understanding of the most important background, $Z + jets$.

This thesis has presented the prospects to measure the $Z(\rightarrow e^+e^-) + jets$ inclusive and differential cross section for 100 pb^{-1}, in particular with respect to VBF $H \rightarrow \tau^+\tau^-$ key quantities with the first data using predictions from different Monte Carlo generators. The fully simulated MC samples have been corrected to hadron level using different correction methods and compared to NLO theory prediction done with MCFM using CTEQ PDF sets corrected for non-perturbative effects. Among the generators studied in this thesis, ALPGEN shows the best agreement with MCFM. The correction methods for detector effects are very different concerning shape dependence and stability against statistical fluctuations of the training sample.

Different background processes have been studied using the predictions from Monte Carlo generators. The dominant background contributions are coming from $t\bar{t}$ and QCD jets, but they are very small, less than 2.5% for the inclusive $Z(\rightarrow e^+e^-) + 1 - 3\ jets$ cross section. Finally, the statistical and systematic uncertainties on the cross section ratio between data and theory have been studied. The dominant uncertainty comes from the JES for the first data.

For the first data the inclusive $Z(\rightarrow e^+e^-) + 1 - 3\ jets$ cross section can be determined with a precision between 7.3% and 13.5% for a JES of 5% and between 12.1% and 25.5% for a JES of 10%. The differentiation between the MC generators, especially for the VBF Higgs boson key quantities is challenging for the first data with the current precision for MC generator validation.

12.2 Outlook

The analysis presented is this thesis, has still some open tasks due to the time constraints and leaves the possibility for optimizations. In the near future the plan is to study the scale dependence of the theory prediction in more detail. In addition, the influence from different UE predictions and the impact of different shapes will be studied. The methods for the correction of detector effects will be optimized and compared again with more statistics. In addition, regularization for the matrix inversion will be used comparing different regularisation algorithms, like e.g. Single Value Decomposition [60] or Tichonow regularisation [59]. For the background,

methods for the estimation from data will be studied, like side band fits for the estimation of the QCD background.
Finally, due to the fact that the LHC will collide protons at a centre of mass energy of 7 TeV instead of 10 TeV in the beginning, the differences in kinematics for signal and backgrounds between 7 TeV and 10 TeV will be studied.

A Running MCFM

In this chapter an example for an input file for running MCFM is shown. For NLO calculations, MCFM has to run two times, once for the real part and once for the virtual corrections. In addition for the calculation of the inclusive $Z(\rightarrow e^+e^-)+2\ jets$ cross section the quark and the gluon contribution have also to run separately.

A.1 Example of an Input File

```
'5.4'           [file version number]

[Flags to specify the mode in which MCFM is run]
.false.         [evtgen]
.true.          [creatent]
.false.         [skipnt]
.false.         [dswhisto]

[General options to specify the process and execution]
41              [nproc]
'real'          [part 'lord','real' or 'virt','tota']
'Z+1Jet'        ['runstring']
10000d0         [sqrts in GeV]
+1              [ih1 =1 for proton and -1 for antiproton]
+1              [ih2 =1 for proton and -1 for antiproton]
120d0           [hmass]
1d0             [scale:QCD scale choice]
1d0             [facscale:QCD fac_scale choice]
.true.          [dynamicscale]
.false.         [zerowidth]
.false.         [removebr]
10              [itmx1, number of iterations for pre-conditioning]
500000          [ncall1]
10              [itmx2, number of iterations for final run]
500000          [ncall2]
1089            [ij]
.false.         [dryrun]
.true.          [Qflag]
.true.          [Gflag]

[Pdf selection]
'cteq6_m'       [pdlabel]
4               [NGROUP, see PDFLIB]
```

```
46                  [NSET - see PDFLIB]
cteq6mE.LHgrid      [LHAPDF group]
-1                  [LHAPDF set]

[Jet definition and event cuts]
81d0                [m34min]
101d0               [m34max]
0d0                 [m56min]
10000d0             [m56max]
.true.              [inclusive]
'cone'              [algorithm]
20d0                [ptmin_jet]
0d0                 [etamin_jet]
4.8d0               [etamax_jet]
0.4d0               [Rcut_jet]
.true.              [makecuts]
15d0                [ptmin_lepton]
2.7d0               [etamax_lepton]
0d0                 [ptmin_missing]
15d0                [ptmin_lepton(2nd+)]
2.7d0               [etamax_lepton(2nd+)]
0.2d0               [R(jet,lept)_min]
0.2d0               [R(lept,lept)_min]
0d0                 [Delta_eta(jet,jet)_min]
.false.             [jets_opphem]
0                   [lepbtwnjets_scheme]
15d0                [ptmin_bjet]
2d0                 [etamax_bjet]
6.5d0               [ptmin_photon]
2.5d0               [etamax_photon]
0.7d0               [cone_photon]
1d0                 [cone_ptcut]

[Anomalous couplings of the W and Z]
0.0d0               [Delta_g1(Z)]
0.0d0               [Delta_K(Z)]
0.0d0               [Delta_K(gamma)]
0.0d0               [Lambda(Z)]
0.0d0               [Lambda(gamma)]
2.0d0               [Form-factor scale, in TeV]

[How to resume/save a run]
.false.             [readin]
.false.             [writeout]
''                  [ingridfile]
''                  [outgridfile]
```

Bibliography

[1] C. Amsler *et al.*, Physics Letters **B667(1)** (2008).

[2] G. Altarelli, *A QCD primer*, hep-ph/0204179.

[3] The ALEPH, DELPHI, L3, OPAL, SLD Collaborations, the LEP Electroweak Working Group, the SLD Electroweak and Heavy Flavour Groups, *Precision Electroweak Measurements on the Z Resonance*, Phys. Rept. **427** (2006) 257, hep-ex/0509008.

[4] P. W. Higgs, *Broken Symmetries and the Masses of Gauge Bosons*, Phys. Rev. Lett. **13(16)** (Oct 1964) 508.

[5] P. W. Higgs, *Spontaneous Symmetry Breakdown without Massless Bosons*, Phys. Rev. **145(4)** (May 1966) 1156.

[6] A. Djouadi, J. Kalinowski, and M. Spira, *HDECAY: A program for Higgs boson decays in the standard model and its supersymmetric extension*, Comput. Phys. Commun. **108** (1998) 56, hep-ph/9704448.

[7] T. Hambye and K. Riesselmann, *SM Higgs mass bounds from theory*, Phys. Rev. D55 **7255** (1997), hep-ph/9708416 v1.

[8] A. Collaboration *et al.*, *Precision Electroweak Measurements and Constraints on the Standard Model*, 0911.2604.

[9] The LEP Working Group for Higgs boson searches Collaboration, R. Barate *et al.*, *Search for the standard model Higgs boson at LEP*, Phys. Lett. **B565** (2003) 61, hep-ex/0306033.

[10] The CDF Collaboration, *Combined CDF and DZero Upper Limits on Standard Model Higgs-Boson Production with up to 4.2 fb-1 of Data*, arXiv:0903.4001.

[11] R. S. Thorne, A. D. Martin, and W. J. Stirling, *MRST parton distributions: Status 2006*, hep-ph/0606244.

[12] A. D. Martin, W. J. Stirling, R. S. Thorne, and G. Watt, *Update of parton distributions at NNLO*, Phys. Lett. **B652** (2007) 292, 0706.0459.

[13] A. D. Martin, W. J. Stirling, R. S. Thorne, and G. Watt, *Parton distributions for the LHC*, Eur. Phys. J. **C63** (2009) 189, 0901.0002.

[14] J. Pumplin *et al.*, *New generation of parton distributions with uncertainties from global QCD analysis*, JHEP **07** (2002) 012, hep-ph/0201195.

[15] A. D. Martin, R. G. Roberts, W. J. Stirling, and R. S. Thorne, *Uncertainties of predictions from parton distributions. 1: Experimental errors*, Eur. Phys. J. **C28** (2003) 455, hep-ph/0211080.

[16] D. Stump *et al.*, *Uncertainties of predictions from parton distribution functions. 1. The Lagrange multiplier method*, Phys. Rev. **D65** (2001) 014012, `hep-ph/0101051`.

[17] J. Pumplin *et al.*, *Uncertainties of predictions from parton distribution functions. 2. The Hessian method*, Phys. Rev. **D65** (2001) 014013, `hep-ph/0101032`.

[18] J. M. Campbell, J. W. Huston, and W. J. Stirling, *Hard Interactions of Quarks and Gluons: A Primer for LHC Physics*, Rept. Prog. Phys. **70** (2007) 89, `hep-ph/0611148`.

[19] J. M. Butterworth, J. R. Forshaw, and M. H. Seymour, *Multiparton interactions in photoproduction at HERA*, Z. Phys. **C72** (1996) 637, `hep-ph/9601371`.

[20] G. Corcella *et al.*, *HERWIG 6.5: an event generator for Hadron Emission Reactions With Interfering Gluons (including supersymmetric processes)*, JHEP **01** (2001) 010, `hep-ph/0011363`.

[21] T. Sjostrand, L. Lonnblad, S. Mrenna, and P. Skands, *Pythia 6.3 physics and manual*, `hep-ph/0308153`.

[22] B. Andersson, G. Gustafson, G. Ingelman, and T. Sjostrand, *Parton Fragmentation and String Dynamics*, Phys. Rept. **97** (1983) 31.

[23] H.-U. Bengtsson and T. Sjostrand, *The Lund Monte Carlo for Hadronic Processes: Pythia Version 4.8*, Comput. Phys. Commun. **46** (1987) 43.

[24] B. R. Webber, *A QCD model for jet fragmentation including soft gluon interference*, Nuclear Physics B **238** (1984) 492.

[25] G. Marchesini and B. R. Webber, *Monte Carlo simulation of general hard processes with coherent QCD radiation*, Nuclear Physics B **310** (1988) 461.

[26] CERN Document Server, http://cdsweb.cern.ch/, (2008).

[27] The ATLAS Collaboration, *The ATLAS Experiment at the CERN Large Hadron Collider*, Journal of Instrumentation **3** (2008), S08003.

[28] *ATLAS detector and physics performance: Technical Design Report, 1*, Technical Design Report ATLAS, CERN, Geneva, (1999).

[29] The ATLAS Electromagnetic Barrel Calorimeter Collaboration, M. Aharrouche *et al.*, *Energy linearity and resolution of the ATLAS electromagnetic barrel calorimeter in an electron test- beam*, Nucl. Instrum. Meth. **A568** (2006) 601, `physics/0608012`.

[30] The ATLAS Collaboration, S. Akhmadalev *et al.*, *Results from a new combined test of an electromagnetic liquid argon calorimeter with a hadronic scintillating- tile calorimeter*, Nucl. Instrum. Meth. **A449** (2000) 461.

[31] J. P. Archambault *et al.*, *Energy calibration of the ATLAS liquid argon forward calorimeter*, JINST **3** (2008) P02002.

[32] The ATLAS Collaboration, *ATLAS muon spectrometer: Technical design report*, CERN-LHCC-97-22.

[33] The ATLAS Collaboration, *ATLAS high-level trigger, data acquisition and controls: Technical design report*, CERN-LHCC-2003-022.

[34] S. D. Drell and T.-M. Yan, *Massive Lepton-Pair Production in Hadron-Hadron Collisions at High Energies*, Phys. Rev. Lett. **25(5)** (Aug 1970) 316.

[35] M. Spira and P. M. Zerwas, *Electroweak symmetry breaking and Higgs physics*, Lect. Notes Phys. **512** (1998) 161, `hep-ph/9803257`.

[36] V. Buescher and K. Jakobs, *Higgs boson searches at hadron colliders*, Int. J. Mod. Phys. **A20** (2005) 2523, `hep-ph/0504099`.

[37] M. A. Dobbs *et al.*, *Les Houches guidebook to Monte Carlo generators for hadron collider physics*, `hep-ph/0403045`.

[38] M. L. Mangano, M. Moretti, F. Piccinini, R. Pittau, and A. D. Polosa, *ALPGEN, a generator for hard multiparton processes in hadronic collisions*, JHEP **07** (2003) 001, `hep-ph/0206293`.

[39] M. L. Mangano, M. Moretti, and R. Pittau, *Multijet matrix elements and shower evolution in hadronic collisions: $Wb\bar{b}$ + n jets as a case study*, Nucl. Phys. **B632** (2002) 343, `hep-ph/0108069`.

[40] F. Caravaglios, M. L. Mangano, M. Moretti, and R. Pittau, *A new approach to multi-jet calculations in hadron collisions*, Nucl. Phys. **B539** (1999) 215, `hep-ph/9807570`.

[41] S. Frixione and B. R. Webber, *Matching NLO QCD computations and parton shower simulations*, JHEP **06** (2002) 029, `hep-ph/0204244`.

[42] J. M. Campbell and R. K. Ellis, *MCFM v5.6, A Monte Carlo for FeMtobarn processes at Hadron Colliders*, (2009).

[43] The ATLAS Collaboration, e. . Duckeck, G. *et al.*, *ATLAS computing: Technical design report*, CERN-LHCC-2005-022.

[44] The ATLAS TWiki, http://twiki.cern.ch/.

[45] The GEANT4 Collaboration, S. Agostinelli *et al.*, *GEANT4: A simulation toolkit*, Nucl. Instrum. Meth. **A506** (2003) 250.

[46] W. Giele *et al.*, *The QCD / SM working group: Summary report*, `hep-ph/0204316`.

[47] J. Tanaka, https://twiki.cern.ch/twiki/bin/view/AtlasProtected/SMHiggsToTauTauToLH, (2009).

[48] The ATLAS Collaboration, G. Aad *et al.*, *Expected Performance of the ATLAS Experiment - Detector, Trigger and Physics*, `0901.0512`.

[49] G. C. Blazey *et al.*, *Run II jet physics*, `hep-ex/0005012`.

[50] C. Schwanenberger, *The Jet Calibration in the H1 Liquid Argon Calorimeter*, ArXiv Physics e-prints (Sep. 2002), `arXiv:physics/0209026`.

[51] P. J. Ilten, *A Study of Tau Identification with the ATLAS Detector at the LHC*, Master's thesis, Georg-August-University Goettingen, (2009).

[52] W. Lampl *et al.*, *Calorimeter clustering algorithms: Description and performance*, ATL-LARG-PUB-2008-002.

[53] The ATLAS Collaboration, A. Moraes, *Modeling the underlying event: Generating predictions for the LHC*, ATL-PHYS-PROC-2009-045.

[54] A. Moraes, C. Buttar, and I. Dawson, *Prediction for minimum bias and the underlying event at LHC energies. oai:cds.cern.ch:872257*, Eur. Phys. J. C **(SN-ATLAS-2006-057)** (2005) 35 p, Accepted as Scientific Note SN-ATLAS-2006-057.

[55] D. Acosta *et al.*, *The underlying event at the LHC*, CERN-CMS-NOTE-2006-067.

[56] P. Bartalini *et al.*, *Multi-parton interactions and underlying events from Tevatron to LHC*, In *Hamburg 2008, Multiparticle dynamics (ISMD08)* 406-411.

[57] J. W. Eaton, *GNU Octave: A high-level interactive language for numerical computations*, (1997).

[58] H. W. Nilsen, *Studying Z/γ+Jet Production in Proton-Antiproton Collisions at $\sqrt{s} = 1.96$ TeV*, Ph.D. thesis, Albert-Ludwigs-University Freiburg, (2009).

[59] B. Hoffman, *Mathematik inverser Probleme*, B. G. Teubner Stuttgart - Leipzig, (1999).

[60] A. Hocker and V. Kartvelishvili, *SVD Approach to Data Unfolding*, Nucl. Instrum. Meth. **A372** (1996) 469, `hep-ph/9509307`.

[61] G. D'Agostini, *A multidimensional unfolding method based on Bayes' theorem*, Nucl. Instrum. Meth. A **362** (Feb. 1995) 487.

[62] T. Adye, K. Tackmann, and F. Wilson, *RooUnfold: ROOT Unfolding Framework*, http://hepunx.rl.ac.uk/ adye/software/unfold/RooUnfold.html, (2009).

[63] *Prospects for the Top Pair Production Cross-section at $\sqrt{s}$ = 10 TeV in the Single Lepton Channel in ATLAS*, Tech. Rep. ATL-PHYS-PUB-2009-087. ATL-COM-PHYS-2009-404, CERN, Geneva, (Aug 2009).

List of Figures

List of Tables

Acknowledgements

I would like to sincerely thank my supervisor Prof. Dr. Arnulf Quadt for his stimulating ideas and the helpful discussions. I am indebted to Prof. Dr. Ariane Frey for her willingness to be the co-corector of this thesis. Particular thanks goes to Ulla Blumenschein for her endless patience and numerous fruitful discussions. These discussions served as a basis for many good and decisive ideas. Despoina Evangelakou deserves grateful respect for taking the time and trouble to alert me to errors in my manuscript. Many thanks to my colleagues of the 2nd Physical Institute, especially Dr. Kevin Kröninger, Dr. Jörg Meyer and Daniel Schiepel for the discussions regarding the analysis framework. I have to thank Prof. Dr. Markus Klute who encouraged me to write this thesis and Philip Ilten for the support at the beginning of my thesis.

Special thanks go to my parents Elke and Dr. Heinz-Volker Fiekas and my husband Jakob Bierwagen, they have always been on my side.

Furthermore, I would like to thank my teacher Otto Thies, who motivates me to study physics.